Master Thesis, Department of Geosciences

Application and evaluation of a borehole camera system for mapping firn stratigraphy

Lisbeth Langhammer

UNIVERSITY OF OSLO

FACULTY OF MATHEMATICS AND NATURAL SCIENCES

Application and evaluation of a borehole camera system for mapping firn stratigraphy

Lisbeth Langhammer

Master Thesis in Geosciences

Discipline: Physical Geography, Hydrology and Geoinformatics

Department of Geosciences

Faculty of Mathematics and Natural Sciences

University of Oslo

02. June 2014

Supervisors: Prof. Jon Ove Hagen, Dr. Thorben Dunse, Dr. Kirsty Langley

This work is published digitally through DUO – Digitale Utgivelser ved UiO

http://www.duo.uio.no

It is also catalogued in BIBSYS (http://www.bibsys.no/english)

“Wohin ich blickte – eisglättender Schnee, im Sonnenlicht glänzende Rillen und Rippen,
kristalline Wogen – Vertrautes, und doch blickte ich auf eine unbekannte Welt,
wo Gletscher nicht ins Tal, sondern ins Meer kalben (…)“

Zeno in Ilija Trojanows EISTAU

Cover photo: Field work during strong winds and sunshine on the Austfonna Ice Cap, 2013

Abstract

The density of snow and firn is crucial for estimating the mass balance of ice masses by GPR, airborne and spaceborne radar altimeter systems. To determine internal reflection horizons in the firn, independent ground-truth observations are required. This thesis presents a borehole video camera system that provides a proxy of the firn structure. A Junior Ultra Low Light borehole video camera and four shallow firn cores were used to investigate the firn stratigraphy close to the Summit camp on the Austfonna Ice Cap, Svalbard. Four videos from residual firn core boreholes and one ice auger borehole are analyzed to simulate an intensity-derived firn stratigraphy record, whereas the firn cores provided ground truth data. The camera lens measures the intensity of light, which is emitted from LEDs and reflected from the borehole wall. To extract a continuous intensity record from the video a Borehole camera video analysis tool was developed. Averaged grayscale values from a predefined section of the borehole wall or an attached mirror underneath the lens were correlated to the position of the camera in the borehole. Depending on a unique threshold value for each video log, the intensity signal was classified in firn and ice sections and compared to the firn cores from the same location. High to moderate agreement (91-63%) between the ground truth data and the intensity-derived stratigraphy is achieved. Two out of four intensity records show approximately the same amount of ice as the corresponding firn core comprises. In general, thin ice layers are underrepresented, whereas thicker ice agglomerations are more likely to be detected with the borehole camera. The quality of the intensity records is highly influenced by the technical set-up and operation of the camera system in cold climate environments. Further improvement of the set-up is recommended to achieve the same quality as ground truth firn core records.

In addition, the specific surface mass balance at the summit of the ice cap was calculated from mass balance stake measurements and firn core. The net balance varies (32.8-81.9 cm w.eq.) throughout the observation period 2009-2012 and is higher than the winter balance in three out of four years. Positive air temperatures in the summer of 2009 caused melting in the summit area. The firn core records exhibit thick ice agglomerations beneath the summer surface of 2009. The results emphasize the importance of considering refrozen meltwater and internal accumulation in the mass balance records.

The described borehole camera system is a logistically inexpensive tool to observe the stratigraphy of firn from beneath the last summer surface to the firn-ice transition. Ice structure, firn stratigraphy and densification surveys as well as in situ or spaceborne remote sensing measurements of the mass balance benefit from the implementation of the borehole camera system in the field.

Acknowledgements

First and foremost, I want to express my gratitude to Professor Jon Ove Hagen, Dr. Thorben Dunse and Dr. Kirsty Langley, my supervisors at the University of Oslo. Thank you for your patient guidance, inspiring discussions and useful critiques of this work. Your enthusiastic encouragement gave me the opportunity to participate in the Austfonna Ice Cap field campaign in 2013.

I would like to offer my special thanks to Trond Eiken, Thomas Schuler, Sanja Forsström, Thorben and Kirsty for their patience, technical and scientific briefings and splendid mood, which made the field work on the ice cap an unforgettable experience.

My special thanks are extended to Anne Fouilloux and the IT staff of the Geosciences department and I am particularly grateful for the help given by Elisabeth Isaksson and Jack Kohler while working in the cold laboratory at the Norwegian Polar Institute in Tromsø.

Proofreading and advice given by Désirée Treichler, Graham Gilbert and Jennifer Porter have been a great help throughout the process of writing.

During my master's studies in Oslo and the semester abroad at the University Centre of Svalbard, I saw crevasses and calving fronts, experienced -35°C in a blizzard, camped along the fjords and walked over glaciers. Life has never been more astonishing.

But it would have been different without the presence of friends, who are as close as family to me after these two years. To Maria Forsgård, Myrsini Dimitriou, Alex Grasshorn-Gebhardt and all the others of our exceptional group of friends, thank you!

Finally, I wish to thank my mother for her support and encouragement throughout my studies.

Two years of master's studies at the University of Oslo were supported with a graduate stipend by the German Academic Exchange Service. Field work in Svalbard, an arctic field and glacier safety course, laboratory work at the Norwegian Polar Institute and participation in several conferences were financed by the University of Oslo and the Norwegian Centre for International Cooperation in Education.

Table of content

List of figures

List of tables

1. Introduction

Between 1972 and 2008, the global sea level rose 2.1 $\pm$ 0.2 mm per year. The annual rate is expected to increase even further throughout this century (Church et al. 2011). While approximately half of the Earth's population lives within 150 km of the coast (United Nations Atlas of the Oceans 2014), rising sea level is becoming a significant hazard for a growing number of humans (Church et al. 2008). Ice mass loss and ocean thermal expansion are the largest contributors to sea level rise of which the melting of glaciers, ice caps and ice sheets account for more than half of the observed rate (Church et al. 2011). To estimate the current ice mass wastage and to predict future contributions, glaciological field campaigns and air- and spaceborne survey programs monitor glacier mass balance changes around the globe (WGMS et al. 2012). Visible imagery, satellite laser and radar altimeter systems as well as GPS and GPR surveys measure the extent and surface elevation of glaciers and ice sheets.

In general, changes in glacier mass balance are determined by measuring changes in ice volume, which are inferred from surface elevation variations through time. To determine the mass change, a constant density value of snow, firn and ice is assumed. Bamber and Kwok (2004, p. 75) state that 'this assumption is reasonable for sub-polar ice masses where the depth of the firn layer (…) is only a few metres'. However, refreezing of meltwater within the snow and internal accumulation are not considered, so the mass loss derived from surface elevation changes is presumably overestimated (Benn and Evans 2010). To emphasize the issue, Bezeau et al. (2013) conducted a survey on the Devon Ice Cap in Canada. They observed an increase in firn densification in the upper 2.5 m of the firn column of up to 80 % over the period 2004-2012. Möller et al. (2011) modeled the climatic mass balance of the Vestfonna Ice Cap, Svalbard, and suggested retention of 25 % of the total surface ablation due to refreezing. The authors conclude that height changes cannot account for mass changes entirely, if densification of snow and firn, refreezing of meltwater and internal accumulation are not considered. Furthermore, the accurate determination of the glacier's surface is an issue for radar altimeter systems. Electromagnetic waves penetrate the surface depending on the physical properties of the material. Volume scattering caused by density changes, ice lenses and layers, hinders the surface retracking in the radar waveform (Hawley et al. 2013, Langley et al. 2007, Langley et al. 2012, Massom and Lubin 2006). Thus, ground truth observations of the snow and firn structure are essential to evaluate mass balance changes derived from air- and spaceborne remote sensing methods.

The European Space Agency (ESA) carries out calibration and validation campaigns (CryoVEX) for the CryoSat-2 satellite, which was launched in 2010. The Department of Geosciences at the University of Oslo and the Norwegian Polar Institute in Tromsø are involved in the CryoVEX

campaigns on the Austfonna Ice Cap, Svalbard. To increase the knowledge about radar scattering in snow and firn, glaciological investigations such as GPS profiles, snow pit observations, shallow ice core retrieval and GPR profiling have been conducted since 2004. Additionally, a camera system is used to log an undisturbed record through boreholes, which were drilled with an ice auger or originated from the shallow firn core drilling in 2011-2013. The borehole wall is illuminated by the light source implemented in the system during the insertion of the camera into the borehole. The amount of reflected light depends on borehole wall material properties (Bohren and Barkstrom 1974, Fudge and Smith 2010, Warren 1982). Hence, ice agglomerations in firn can be detected (Hawley et al. 2003, Hawley et al. 2008a, Hawley and Waddington 2011, Hubbard et al. 2008). Ideally, the operation of the borehole camera system should provide a proxy of the firn densification and ice distribution in the firn column from the surface to the firn-ice transition.

The aim of this study is the evaluation of the borehole camera system for investigating firn stratigraphy. The question is whether or not the borehole camera system used by the University of Oslo can provide a firn stratigraphy record in the same quality as a firn core. A processing tool, developed in MATLAB (2013) for this thesis, is used to classify ice and firn sections in the borehole wall recorded in the videos. Several technical and operational aspects of the set-up and the processing algorithm are assessed to determine if the borehole camera is a valuable tool for glaciological field work. To verify the quality of the borehole camera derived stratigraphy, the logs are compared to shallow firn cores and analyzed according to the displayed amount of ice. Furthermore, the specific mass balance of the summit area of the Austfonna Ice Cap is calculated from mass balance stakes and firn cores. The intention of the analysis is to estimate the amount of refrozen meltwater in the snow pack which survived one seasonal cycle. Internal accumulation and ice layer distribution in the firn column are interpreted by firn core stratigraphy records from subsequent years.

2. Fundamentals

2.1 Glaciological background

The cryosphere is described as the sum of diverse land or sea ice masses on the Earth's surface. The term comprises frozen water in the type of sea or river ice, solid ground at a permanent temperature below the freezing point (permafrost), seasonal snow cover as well as glaciers (Hagen and Reeh 2004). Ice masses, which originate from the compaction of snow and flow downwards by the force of gravity, are defined depending on the spatial extend.

Ice sheets exceed an area larger than 50 000 km^2. Greenland in the northern hemisphere and Antarctica located south of 60°S are the largest ice bodies on Earth. Ice caps (e.g. Austfonna and Vestfonna on the Svalbard archipelago, Vatnajökull on Iceland) cover areas smaller than 50 000 km^2 and are less affected by topographical constrains. In contrast, ice stream and outlet glaciers are confined by the surrounding and underlying landscape (Graham 2011). To understand the history and to predict the future progress of climatic and sea level changes, the global amount of snow and ice and their current trend of development has to be quantified with comprehensive scientific methods.

2.1.1 Mass balance of land ice

The mass balance of a glacier or ice sheet is the rate of gain and loss of mass throughout a particular time period (Hagen and Reeh 2004). Ice bodies obtain mass (accumulation) by snow deposition, wind drift, refreezing of liquid precipitation or meltwater, avalanches from the walls of mountain ridges or basal adherence. Melting is the dominant process of mass wasting (ablation) in the alpine regions, whereas the influence of sublimation and evaporation increases in the dry Polar regions. Calving, the loss of ice through disruption and disintegration of ice shelves and marine terminating glacier tongues, is observed as the primary ablation process of the Antarctic and Greenlandic Ice Sheet (Benn and Evans 2010).

Several terms define individual aspects of the mass balance concept. The specific mass balance is the quantity of mass change at a specific location on the ice body. It is described as the sum of accumulation and ablation throughout a chosen time interval. The concept neglects the influence of glacier dynamics on the overall mass balance. Following the suggestion by Hagen and Reeh (2004), the variation of mass for the entire ice column at a certain location of the glacier is referred to as local mass balance.

Equation (1) describes the term mathematically with b_s as the specific mass balance at the surface and b_b at the bottom. H represents the ice thickness, t = time, v_s and u_s (u_s in the

direction of the flow) are horizontal components of the surface velocity and $\bar{u}$ the depth-averaged velocity (Hagen and Reeh 2004, Reeh and Gundestrup 1985, Reeh 1999):

$$\frac{\partial H}{\partial t} = b_s + b_b - \frac{u}{u_s}\left[H\left(\frac{\partial u_s}{\partial x} + \frac{\partial v_s}{\partial y}\right) + u_s \frac{\partial H}{\partial x}\right] \quad (1)$$

The overall volume change (equation 2) of an entire glacier or ice cap is defined as the total mass balance. The mass balance equation is expressed as the change in ice volume V per time unit t. The positive or negative balance can be determined by measuring the surface elevation variations with direct glaciological methods or by applying the 'budget approach'. The annual surface ablation from melt and run off M_m and ice loss due to calving M_c are subtracted from the annual surface accumulation M_a. If melt or freeze-on at the bottom of ice body M_b occurs, the mass balance decreases or increases, respectively (Hagen et al. 2003, Hagen and Reeh 2004):

$$\frac{\partial V}{\partial t} = M_a - M_m - M_c \pm M_b \quad (2)$$

In general, the observation period is considered to be 12 months to investigate one full cycle of accumulation and ablation. The beginning of the interval is dependent on the geographical location, climatic conditions, accessibility and logistical effort. Ideally, field observations are carried out before the onset of the melting season and before the first snow deposition (Cuffey and Paterson 2010).

2.1.2 Surface mass balance

By disregarding glacier dynamics, the annual mass balance of the glacier can be classified into two separate values throughout the balance year. The winter balance is the rate of accumulation at the surface, whereas the summer balance is determined by the overall ablation rate. The total mass loss or gain at the end of the seasonal cycle is referred to as annual (net) balance. It is negative in the lower areas of a glacier, where the amount of melt exceeds the snow deposition and positive at higher altitudes. The idealized curve in Figure 1 illustrates the specific mass balance at a position in the accumulation zone.

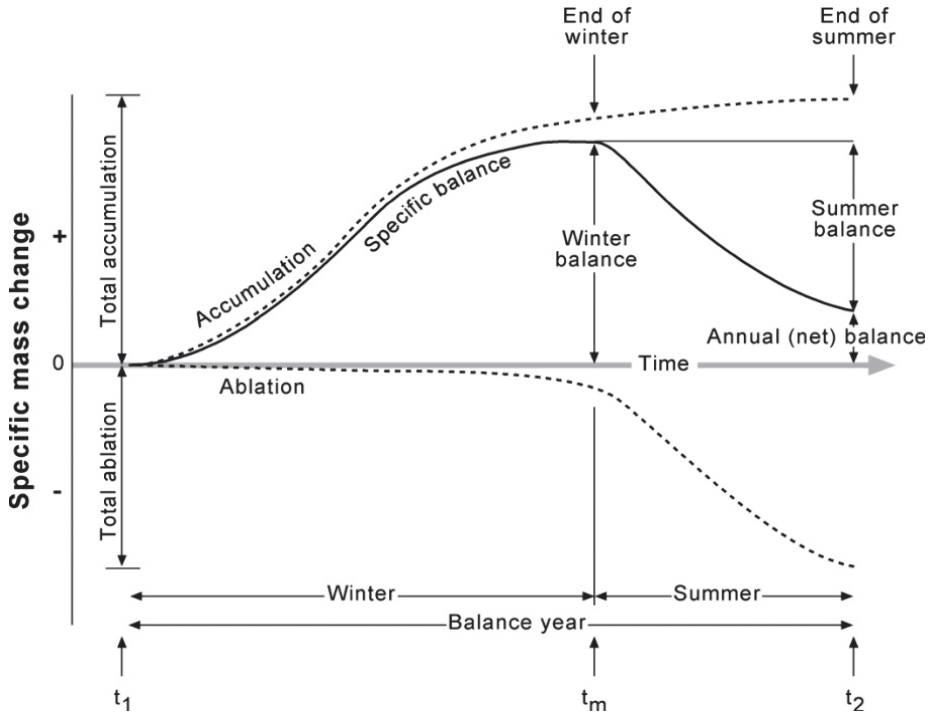

Figure 1: Annual seasonal cycle of accumulation and ablation. (Cuffey and Paterson 2010)

The accumulation occurs consistently throughout the winter season and less during the summer. At the end of summer ablation increases critically, exceeds the accumulation and the specific mass balance decreases. The net balance can be measured at the end of summer, before new snow is deposited on top of the old surface. Figure 1 is exemplary, but representative for the season cycle at any location on a glacier, if adjusted to the local conditions and time period (Cuffey and Paterson 2010). The processes that determine the net balance b_n at the surface, can be summarized with the following equation:

$$b_n = a_s + a_a + a_r - m_s - s \pm w \tag{3}$$

Snowfall a_s, avalanche deposition a_a and refreezing of meltwater a_r add to the accumulation, whereas melting m_s and sublimation s reduce the net mass balance. Depending on the location and wind direction, redistribution of snow due to wind w has a negative or positive effect. The amount of mass loss or gain is generally quantified in kg m^{-2} and mm water equivalent (w.eq.) m^{-2}. The units Gt (gigaton) and km^3 w.eq. are used in the context of sea level rise estimations.

2.1.3 Glacier facies

Glaciers and ice sheets can be subdivided into several zones according to the rate of surface melt and ice temperatures. Cuffey and Paterson (2010) classified the glacier body as seen in Figure 2, following the concept of Benson (1961) and Müller (1962).

Above the dry-snow line no surface melting occurs. The dry snow regions are found in the interior of the Greenland Ice Sheet and Central Antarctica, where the mean annual air temperature does not rise above -25° C (Benson 1961, Cuffey and Paterson 2010).

In the percolation zone meltwater infiltrates the underlying snow heterogeneously without raising the temperatures of the entire snow pack to 0°C. Refreezing of the melt water causes further warming of the surrounding snow due to latent heat release. When 1 gram of water refreezes, sufficient latent heat is produced to warm 160 grams of snow by one degree (Cuffey and Paterson 2010).

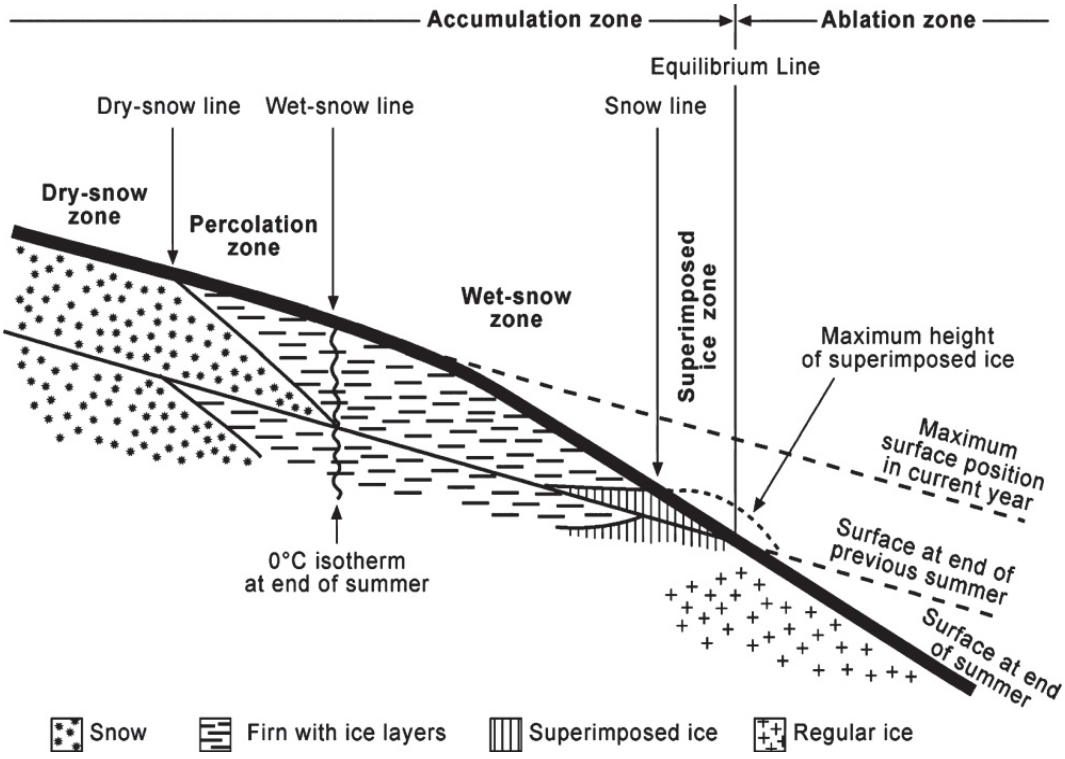

Figure 2: Generalized glacier facies. (Cuffey and Paterson 2010)

The zone below the percolation area is the wet snow zone. During the ablation season the air temperatures rise high enough to produce an amount of meltwater, which warms the snow pack to 0°C when it refreezes. Surplus meltwater can percolate even deeper than the last year's summer surface (LSS) (Cuffey and Paterson 2010). The LSS can be identified as the interface between the ice and the snow pack in the ablation area or as a well-defined ice layer in the accumulation zone (Dunse et al. 2009). The mass of snow beneath the LSS, which endured on ablation season and is not yet metamorphosed into glacier ice, is specified as firn (Cogley et al. 2011).

Internal accumulation refers to meltwater that percolates into the firn beneath the LSS and refreezes in cold firn. Refrozen meltwater, which infiltrates the snow pack during the summer

period is excluded from the definition. The definition includes capillary water that is cooled to the freezing point by the propagating winter cold wave (Schneider and Jansson 2004).

Ice lenses, layers and ice glands form, when the snow pack and firn are at temperatures below the freezing point. In this case, the mass is not lost due to run off, but rather redistributed and the surface elevation decreases. Mass balance measurements have to be corrected for the amount of internal accumulation particularly in regions without a dry snow zone in the accumulation area (Cuffey and Paterson 2010).

Quantifying the amount of refrozen water in the firn is logistically difficult and time consuming. By neglecting internal accumulation and refrozen water in the snow pack, the positive net mass balance is underestimated. The refreezing of meltwater does not add to the winter balance, but decreases the summer balance, because of the reduction of meltwater run-off. Studies have shown that approximately 7 % of the meltwater refreezes in the accumulation zones of Icelandic and Norwegian glaciers (Jóhannesson et al. 1995) and up to 30 % on the Greenland Ice Sheet, respectively (Box et al. 2006). Refreezing of rain water below the LSS, water in crevasses or moulins and basal water, which infiltrates the glacier ice from below, is categorized as internal accumulation as well.

An extensive overview of the relevance and terminology of internal accumulation is given by Marchenko (2012) as well as a detailed literature review on internal accumulation and refreezing on glaciers in Svalbard (Marchenko 2013).

The superimposed ice zone is defined as the part of a glacier between the snow or firn line and the equilibrium line (Cuffey and Paterson 2010). Meltwater and rainfall, which refreezes at the bottom of the snow pack above the LSS creates a distinct layer of ice. If the ice becomes exposed to the surface, because of continuous melting of the overlying snow, it is referred to as superimposed ice (Benn and Evans 2010). The formation is affected by the near-surface ice temperatures and the air temperatures. The large amount of internal accumulation in the wet snow and superimposed ice zone has to be considered in the estimation of the annual mass balance. At the equilibrium line the net mass balance is zero. The accumulation area with an overall gain in mass is located above, whereas the ablation area with bare glacier ice at the surface extends below it. (Cuffey and Paterson 2010).

2.1.4 Firn densification

Several processes are involved in the transformation of snow into ice. The climate and the geographical location of the glacier determine the rate of densification. Snow deposits in a temperate climate transfer much more rapidly into firn and ice than in the Polar regions. The

change in consistency is driven by high air temperatures and the available amount of rain and meltwater (Cuffey and Paterson 2010).

Newly fallen snow has a density of 50-70 kg m^{-3}, whereas redistributed wind packed snow can reach densities up to 400 kg m-3 (Figure 3). Firn consists of recrystallized grains, which are surrounded by air or water-filled spaces. The density varies between 400-830 kg m^{-3}. When firn reaches the pore close-off zone at 830 kg m^{-3}, the air spaces between the grains are sealed off from the atmosphere above. The pore close-off depth defines the boundary between firn and glacier ice. The maximal density of glacier ice in mountain glaciers is approximately 917 kg m^{-3}, whereas temperatures close to the melting point and high pressures in the interior of the large ice sheets cause the ice to reach an in situ density of 923 kg m^{-3} (Cuffey and Paterson 2010).

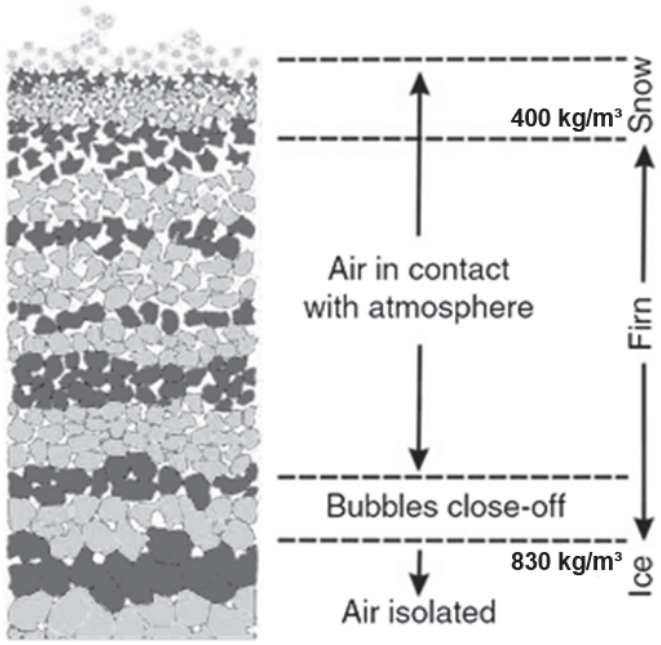

Figure 3: Schematic densification process determined by density. The grayish colored layers in the snow pack and firn characterize annual snow depositions. (Modified after Bertler (2011))

The process of firn densification comprises various mechanisms, which differ in dry snow and wet snow conditions. Dry snow zones in the interior of the Greenlandic and Antarctic Ice Sheet represent regions, where all types of dry snow metamorphism can be observed. Wind plays a major role in the redistribution and destruction of snow crystals. The crushed, smaller crystals are packed closer together and increase the density of the surface layer (Benn and Evans 2010). Due to the exerted pressure of the overlying snow, the grains within the snow pack or firn settle. Snow is compacted by the relocation of grains relative to each other, which is enhanced with rising overburden pressure. The decrease in pore space due to settling is known as grain-boundary-sliding (Cuffey and Paterson 2010, Kinnard et al. 2008). Additionally snow crystals

tend to be energetic unstable. The outermost molecules of the crystal branches are relocated with time in direction of the vapor-pressure gradient. The equi-temperature metamorphism causes the particles to become rounder in shape and grow at the cost of smaller crystals.

Sintering is the process of bonds forming between particles in dry snow pack conditions (DeWalle and Rango 2008). The pore space between the grains decreases, while the grain size increases. Firn with high densities and ice beyond the pore close-off point deform with a creep-like behavior and grains recrystallize because of internal diffusion (Cuffey and Paterson 2010).

The densification processes are sensitive to the local climate, hence, the metamorphosis is accelerated in the wet snow zone areas with higher air temperatures. Therefore the amount of melt water is a significant factor. In addition to the settling of the crystals, meltwater enforces the melting of the crystal branches and smaller grains. The crystal sizes become more homogenous. Tension of the water film in the pores attracts the grains and pore water-bonded crystals can freeze into denser clusters. For this reason the overall density of the firn in temperate climates increases more rapidly over time than on polar ice sheets. The firn-ice transition is located closer to the surface and the densification rate fluctuates throughout the year (Cuffey and Paterson 2010).

2.1.5 Mass balance measurement techniques

Multiple methods are used to evaluate the gain and loss of glacier ice. They range from direct glaciological measurements and water in- and output assessments to the estimation of surface elevation changes by air- and spaceborne sensors. This chapter gives a brief overview of the most important techniques in glaciology in general, with a focus on the methods that were applied during the field work for this thesis.

I. GPS surveys

Geodetic methods investigate the change in surface elevation throughout a specified time period. The surface height can be measured directly in the field by global positioning systems (GPS) and theodolites or remote sensing devices. Distance measurements from fixed points around the glacier offer precise information about surface rising or lowering. GPS surveys can be used to cover wider areas. Static GPS devices are mounted onto poles to trace the ice flow velocity, whereas kinematic GPS are applied to track elevation profiles along a predefined route on the glacier, ice cap or ice sheet (Hagen and Reeh 2004). Eiken et al. (1997) demonstrated a position accuracy of ± 10 cm in elevation and ± 5 cm horizontally, if a sufficient number of satellites (>5) is available (Hagen et al. 1999).

Comparing aerial photographs from different times of acquisition is another method to analyze long term surface elevation changes. Furthermore, digital elevation models (DEM) can be

reconstructed from historical maps or aerial photographs with photogrammetry methods. The result is a map of the spatial distribution of glacier surface elevation changes.

II. GPR

Ground penetrating radar (GPR) systems visualize snow distribution on a large spatial scale and contribute to the mass balance measurements from traditional methods. GPR systems used in glaciological field campaigns operate on frequencies of 200 MHz and higher. The speed of electromagnetic waves depend on the dielectric constant ε, which varies with the material's temperature and density. Several processing steps have to be performed to retrieve reliable results from the tracked reflection horizons. To validate the GPR signal and to distinguish between the snow-firn and firn-ice interface, snow probing and stratigraphy analysis of shallow cores are advisable (Hagen and Reeh 2004).

III. Remote sensing

Glaciers are usually situated in areas of higher elevation and in many cases in inaccessible regions. Therefore, satellite remote sensing techniques are practical tools to study the cryosphere on nearly the Earth's surface. Today's sensors produce data with a higher spatial and temporal coverage in contrast to traditional glaciological survey methods for instance mass balance stake measurements, ice cores and snow pit analysis.

Various types of sensors are operating onboard of satellites; ASTER (Advanced Spaceborne Thermal Emission and Reflection radiometer) is an example for a multispectral instrument, which detects wavelengths in the near-infrared light spectrum to map the extent of glacier ice and snow cover. Most visible and near-infrared sensors provide the users with stereo images, because of their nadir and backward looking orientation. The stereo images are used for the generation of DEMs.

Other imaging instruments, for instance synthetic aperture radars (SAR) and scatterometers transmit microwave pulses towards the Earth's surface. SARs measure the range from the ground to the satellite, whereas scatterometers register the intensity of the backscattered radiation. Compared to visual sensors, the instruments are able to provide images during night and from regions with consistent cloud cover. This advantage is beneficial for glaciological observations in the Polar regions and high altitude mountain areas. Satellite altimeter instruments are based on either microwave or laser technique. The CryoSat-2 satellite carries the sensor SIRAL (SAR Interferometric Radar Altimeter), which measures the time delay between the emitted and received microwave pulse. Based on this principle the distance between the satellite and ice sheet can be calculated and surface elevation changes detected. The GLAS (Geosciences Laser Altimeter System) onboard ICESat employs the same method, though it uses LIDAR (Light Detection And Ranging) instead of RADAR (Radio Detection And Ranging).

The focus on SAR and LIDAR altimeter derived elevation changes lies on ice caps, ice shelves and ice sheets. If the entire ice sheet is under investigation, acquiring remote sensing data is less time-consuming and logistically extensive than glaciological field surveys.

Topography changes refer to variations in volume, which then are transferred into mass changes by assuming a given density relation. Nevertheless, to assure that the recorded mass change is real, glacier dynamics have to be considered (Bamber and Kwok 2004). Moholdt et al. (2010) have shown that thickening in the interior of the Austfonna Ice Cap is rather related to mass build up in the quiescent phase of a surge-type glacier than to an increase of annual precipitation. Despite the advanced technology of remote sensing methods and sensors, direct measurements of the in situ conditions on the glacier are essential to achieve precise estimates of the mass changes.

IV. Direct measurements of mass balance components

The specific mass balance components can be measured directly. To quantify the accumulation and ablation rate, point measurements are taken on the glacier's surface. Stakes, which are drilled into the ice or firn, are used as a reference frame to surface changes. The net mass balance is preferably collected at the end of the ablation season by measuring the distance between the stakes top and the summer surface. The observations have to be repeated on an annual or seasonal basis to retrieve reference heights of the surface. If the stake is positioned in the ablation zone, it will melt out progressively.

The yearly differences in level height between the LSS and the present surface account for the mass lost during one year. The same principle can be used in the accumulation area. Snow deposits will bury the anchored stake over time. The change in height of the stake above the summer surface from one year to another is equal to the positive net balance. The thickness of the snow pack at the end of the accumulation season can be transferred into snow-water equivalent and thus it defines the winter balance. It can be accessed by snow probing as well. An avalanche probe is lowered into the snow until it hits the LSS. In wet snow conditions the LSS is a steady ice layer, which is harder to penetrate than the overlying snow. Deployed stakes can cause problems, if not inspected on a regular basis. They can be buried underneath snow or melt out of the surface and tilt over. When the overall mass balance of a glacier is extrapolated from stakes year after year, the horizontal displacement of the stakes has to be taken into account. For each study area it has to be decided depending on the local conditions, if the stake method is appropriate. In case of very fast flowing, heavily crevassed or debris covered glaciers, remote sensing methods might be more suitable.

The application of mass balance stakes on glacier in climates with precipitation in solid form in summer and ablation periods in winter has to be reconsidered as well. The explicit differentiation between summer and winter balance can become invalid (Hagen and Reeh

2004). To establish a representative grid over the glacier the total amount of stakes has to be considered carefully. Hagen and Reeh (2004) propose that 5-10 stakes for an area of <20 km^2 and 10-20 stakes for glaciers with a size of 20-500 km^2 are adequate.

V. Snow pits

To investigate the mass balance and enhance remote sensing based predictions, ground truth density measurements are recommended. Digging snow pits is a valuable method to examine snow layers and to measure the density of the deposit. The bulk density can be calculated by sampling the snow with a container of a known volume, usually a plastic or aluminum tube. The hardness of the layers is determined with the penetrometer or hand test. Snow temperature profiles compiled along the full depth of the pit and grain size measurements are other standard procedures in snow pit investigations (DeWalle and Rango 2008).

VI. Shallow cores

Shallow firn and ice cores can be used to obtain density profiles from snow/firn accumulations at greater depth. The cores give information about the stratigraphy below the LSS, the existence of dust layers or the chemical composition of past climates reconstructed from trapped air bubbles. The analysis of the oxygen isotope ratio of ^{16}O and ^{18}O reveals annual cycles in the accumulated firn and ice (Hagen and Reeh 2004). Density measurements and annual layer counting are performed to reconstruct the deposition conditions, the amount of internal accumulation and depth-age relations of the trapped gases.

VII. Hydrological methods

Hydrological methods are based on the input-output approach. The annual mass balance is represented by the amount of water, which is equal to the difference between the incoming water from the catchment area and the run-off from the glacier.

The mass balance components include the total amount of precipitation during the observation period, meltwater run-off from the glacier and surface evaporation. Further parameters are the glacial (e.g. sub-, supra- and englacial water) and the non-glacial storage (e.g. snow cover from adjacent mountains) (Benn and Evans 2010).

The most sophisticated results are achieved by combining the concepts and methods mentioned above. Advantages and disadvantages of each have to be considered to monitor the present glacial change accurately and to predict the future development.

2.2 Borehole video cameras

Borehole camera systems are commonly operated instruments in geological and geotechnical settings. Industrial companies and research institutes employ video and imaging systems for borehole logging in rock or soil to analyze the bedrock stratigraphy visually. In urban areas, borehole camera systems are often used to inspect the pipe and drainage system or other inaccessible locations (Lovell et al. 1999). Recently scientists started to investigate glacier boreholes with visual systems. Instead of bringing heavy coring equipment to the field and spending the time with drilling and transporting ice cores, more inexpensive and time efficient equipment such as borehole camera systems, are needed to record the firn and ice stratigraphy of the glacier.

Ice and firn cores reveal a wider range of information and are therefore necessary for more profound research. In contrast borehole camera systems are lightweight and easily applicable instruments, but with a limited amount of information value. This chapter focuses on the historical development of video systems specifically operated on glaciers or ice sheets. Furthermore, the basic theory of light propagation in firn is explained.

2.2.1 History and application on glaciers

Harrison and Kamb (1973) were first to describe the attempt to utilize a borehole camera in glacier ice. They inserted a single shot camera in a glacier borehole on the Blue Glacier, USA, to observe basal sliding rates along the bedrock. Their attempt to monitor the subglacial conditions with photographic cameras was the onset of further investigations. Since then surveys have been carried out, in which borehole image and video systems have been used in glaciers, ice sheets or ice shelves (e.g. Copland et al. 1997, Engelhardt et al. 1978, Harrison and Kamb 1973, Hawley et al. 2008b, Hubbard et al. 2012, Koerner et al. 1981).

In the 1990s, Pohjola (1993, 1994) investigated the bed rock conditions and occurrence of englacial voids of Storglaciären, Sweden. High velocity peaks in basal motion were measured and interpreted as local stress release events caused by the topography of the bedrock. Harper and Humphrey (1995) surveyed voids, ice structures and bubble content in the ice column to test a glacier flow model. Copland et al. (1997) analyzed the hydrology and internal structure of the Haut Glacier d'Arolla, Switzerland, with a borehole camera video system. The results were used to correlate water pressure, basal sliding rates and water chemistry. Further interest was shown in the turbidity of the emerging water in the borehole, voids and englacial channels in the borehole wall.

A few years later, Carsey et al. (2002) presented a down- and side-looking camera system to examine the basal conditions of the Ice Stream C in West Antarctica. Hawley et al. (2003)

designed and operated a borehole optical stratigraphy (BOS) system consisting of a borehole camera and a post-processing software at Siple Dome, Antarctica. Annual layers in the record were identified manually and compared to ice core from the same location. The correlation of the two datasets provided a sufficient depth-age estimation of the glacier ice. Other field operations and the improvement of the BOS system were undertaken in the following years (Hawley 2005, Hawley and Morris 2006, Hawley et al. 2008a, Hawley et al. 2008b, Hawley and Waddington 2011).

Hawley and Morris (2006) used a neutron scattering probe to derive density from a borehole that was logged by the BOS system as well. Their results reveal a change in correlation between the density and the borehole video intensity with depth for shallow boreholes.

Another borehole camera system for glaciers and ice shelves was introduced to the scientific community in 2008. Hubbard et al. (2008) established the optical televiewer (OPTV) system supported by an Borehole and Ice feature annotation tool (BIFAT) (Malone et al. 2013) to detect horizons and melt features in the borehole wall. Roberson and Hubbard (2010) drilled six boreholes into Lovénbreen, Svalbard, to map deformation structures and englacial debris accumulations. They produced a high resolution three-dimensional grid of the glacier by combining the 360° borehole camera videos with supraglacial observations of debris ridges. In 2012 the OPTV system was used on the Roi Baudouin Ice shelf in East Antarctica to identify facies along the borehole and to investigate the ice shelf bottom. As a further application, Koerner et al. (1981) and Hubbard et al. (2008) mentioned the possibility to inspect the borehole bottom in the event of drilling equipment failure or inefficient drilling rates.

The development of methods to interpret the visual properties of ice and firn is an ongoing process. Ice core visual stratigraphy, in contrast to borehole video logging, is another technique to examine annual layers, melt features, impurities and bubble content in the ice column (Kinnard et al. 2008, Sjögren et al. 2007, Svensson et al. 2005). The borehole video camera systems for glacial environments were designed to provide the direct and real time monitoring of the bedrock beneath the ice and the internal structure of the glacier (e.g. Hawley et al. 2003, Hawley and Waddington 2011, Hubbard et al. 2008, Malone et al. 2013, Roberson and Hubbard 2010). To simplify the drilling process in the field and to minimize the logistical expenses, borehole observations without retrieving an ice core are preferable.

2.2.2 Light propagation in firn

A commercial borehole camera system is equipped with a light source to illuminate the borehole walls. The emitted light is transmitted through the firn or reflected from the borehole wall, respectively. Changes in the wall properties cause differences in the amount of reflected and

scattered light, which is recorded by the video camera device (Fudge and Smith 2010, Hawley et al. 2003). The variations are displayed as lighter or darker zones in the borehole video and can be quantified in grayscale values. Both terms, brightness (Hawley et al. 2003, Hubbard et al. 2008) and intensity (Kinnard et al. 2008, Sjögren et al. 2007), are used in glaciological literature to characterize the grayscale value of an image section. To minimize confusion, image intensity will be used throughout this thesis.

To derive relative or absolute density from firn and ice with a borehole camera video, the intensity of the received light is measured. The procedure is based on the assumption that the scattering effects in the firn are directly related to its physical properties (Fudge and Smith 2010). As shown by Bohren and Barkstrom (1974) and Warren (1982), the intensity in the record depends on the bubble size and content, the grain size and the grain shape. These properties also determine the density of the firn and ice body.

Fudge and Smith (2010) modeled the light transfer in firn to improve the general understanding of the dependency of image intensity on physical properties. They concluded that variabilities are not only caused by change in density. Impurities, drilling effects (e.g. saw tooth pattern, gouges and ridges), borehole diameter variations, adhered ice chips or a shift in camera position induce variations as well.

An inversion in the intensity record in the upper most part of the log (10-15 m depth) was noted in several studies (Hawley and Morris 2006, Hawley et al. 2008a, Hubbard et al. 2008, Hubbard and Malone 2013). Referring to Bohren and Barkstrom (1974) and Warren (1982), Hawley and Morris (2006) argued that the inversion is caused by a change in snow properties with depth due to the firnification process. The transition between grain boundary sliding and pressure sintering in the firn determines the inversion depth. During the process of grain boundary sliding, grains have a relative small size compared to the air spaces and are rearranged in position. The intensity of the backscattered light is higher, the greater the specific surface area (SSA). The SSA represents the area of the ice-air boundary surface per unit volume. In the process of pressure sintering, the particles grow larger and the air space in between decreases. Thus, the SSA is reduced as well as the intensity of the backscattered light (Cuffey and Paterson 2010, Fudge and Smith 2010).

The correlation between density, borehole diameter, intensity and bubble or grain size is not unique. More light is reflected from the wall, if the grain size is smaller and bubbles in ice are dominant. By varying the factors, the same intensity value can be achieved. Even if the grain size is known, density cannot directly be derived from the intensity due to the influence of the grain shape. As a general rule, bubbly ice and low density sections are brighter in a borehole video than the dense ice layers and melt features (Hubbard and Malone 2013).

Even though the correlation between the density of the firn or ice and the borehole camera intensity is not unique, the overall stratigraphy in the borehole wall is evident in the video. Therefore the borehole log has the potential to reveal individual layers that can be detected manually or automatically (Hawley et al. 2003, Hubbard et al. 2008, Malone et al. 2013)

3. Field site Austfonna Ice Cap

The Austfonna Ice Cap covers an area of 7800 km^2 and is situated on the Nordaustlandet Island (79°42'N, 24°00'E) in the north-east of the Svalbard archipelago (Moholdt and Kääb 2012). The summit area (Figure 4) is located at approximately 800 m a.s.l. and the ice cap thickness varies from below 300 m in the southeast to a maximum of ~580 m at the dome in the interior (Dowdeswell et al. 1986, Moholdt et al. 2010).

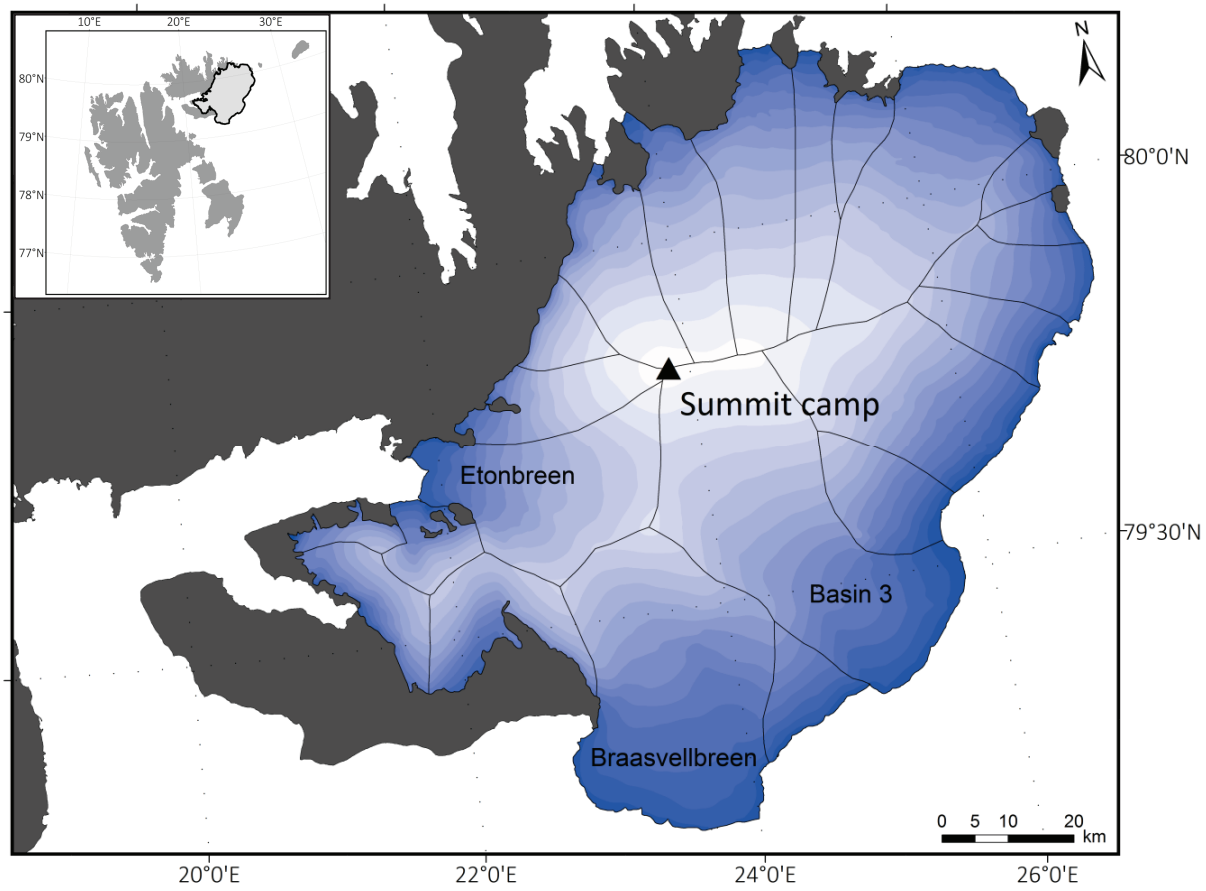

Figure 4: Austfonna Ice Cap in the north-east of the Svalbard archipelago. The contour lines of the Austfonna DEM are spaced in 50 m intervals. The black triangle localizes the Summit camp. Nordaustlandet outlines from Nuth et al. (2013) and Austfonna Ice Cap outline, basins and DEM from Moholdt and Kääb (2012).

The southeastern basins and northwestern basins are separated by a major ice divide from where the ice flows towards the sea (Dowdeswell et al. 1986, Dunse et al. 2011). While the majority of the outlets have low surface velocities with less than 10 m y^{-1} (Dowdeswell et al. 1999, Moholdt et al. 2010), few are known to reach higher velocities and surges have been reported for three of the basins (Basin 3, Etonbreen and Bråsvellbreen) (Lefauconnier and Hagen 1991). Current GPS observations and Terra-SAR X velocity maps from Basin 3 have shown a significant increase in flow velocity and the widespread crevasse fields are noted to be an indication for an ongoing surge in the area (Dunse et al. 2012, Dunse et al. 2014).

Temperature records from an automatic weather station, located close to the equilibrium-line altitude in the west of the Austfonna Ice Cap, show a mean annual air temperature of -8.3 °C for the observation period 2004-2012. Mean monthly temperatures below the freezing point are usually recorded for all seasons except the summer (June, July and August), but short episodes of temperatures above 0°C are registered throughout the year at lower elevations on the ice cap (Schuler et al. 2013). The precipitation distribution on the ice cap is highly influenced by low-pressure weather systems with warm and moist air from the south-east and local wind patterns. Higher snow accumulation rates in the southeast, in contrast to the northwest demonstrate the asymmetric distribution, and lead to a distinct accumulation gradient (Pinglot et al. 2001, Taurisano et al. 2007).

Dunse et al. (2009) and Hawley et al. (2013) investigated glacier facies on the Austfonna Ice Cap by GPR and airborne Ku-band altimeter. The accumulation area consists of the superimposed ice and wet snow zone. The summit area is located in the percolation zone depending on variability of the mean annual air temperature. Temperatures above zero during summer and rain events in the winter time cause percolation features or other facies related to melting and refreezing. Wind crusts, depth hoar, ice layers and lenses indicate varying wind and temperature conditions throughout the year. Radar altimeter and GPR measurements are used to map the extent of the facies on the ice cap by distinguishing zones according to their specific signal reflection pattern (Brandt et al. 2008, Langley et al. 2007). In the period from 2002-2008, the Austfonna Ice Cap was thickening in the interior by 0.5 m y^{-1}, but the mean mass balance was measured to be negative with -0.16 $\pm$ 0.06 m w.eq. per year, if the retreat of the glacier front due to calving is incorporated in the calculation (Dowdeswell et al. 2008, Moholdt et al. 2010).

Bamber et al. (2004) and Moholdt et al. (2010) derived similar elevation changes from the accumulation zone for the years 1996-2002 and 2002-2008, respectively. To explain the interior thickening of the ice cap, Bamber et al. (2004) interpreted the rise in elevation as an increase of moisture flux and therefore more precipitation from incoming low-pressure weather systems, whereas Moholdt et al. (2010) suggest a dynamic imbalance, which is caused by mass build-up in the quiescent phase between surges (Bevan et al. 2007, Dunse et al. 2012, Hagen et al. 2005).

4. Data sets and methods

The data sets used in this study were provided by the glaciology section at the Department of Geosciences of the University of Oslo. Mass balance stake measurements, borehole video camera logging and firn core drilling were carried out on the Austfonna Ice Cap, Svalbard, on an annual basis. The chapter describes the technical specifications of the borehole video camera system, the processing tool and the analysis of the intensity record. Furthermore the firn core and mass balance stake data sets are presented.

4.1 Borehole video camera system

The borehole camera system described in this work is a commercial video device. The lightweight camera system is transportable on snowmobile sledges and proved to be deployable in cold climate environments. It can be utilized to record the ice distribution below the snow surface or the LSS. The section gives an insight view about the video system's operation in the field and its technical properties. Furthermore, the developed processing chain is explained in detail in this chapter.

4.1.1 Data set

The analyzed borehole camera data set consist of four videos (Table 3 in appendix) logged in multiple locations on the Austfonna Ice Cap from 2011 to 2013. The videos were recorded during the field season from April-May by different glaciological field teams of the University of Oslo. The boreholes are located approximately 2.4 km east from the Summit camp on the ice divide (Figure 5). The videos from 2011 and 2012 were recorded in boreholes, which originated from firn core drilling. The two 2013 videos were produced in the firn core borehole (A) and in an ice auger borehole (B), respectively. The locations of the 2011 and both 2013 boreholes are closer than 3 m compared to each other, whereas the 2012 firn core borehole is situated less than 180 m in the southwest.

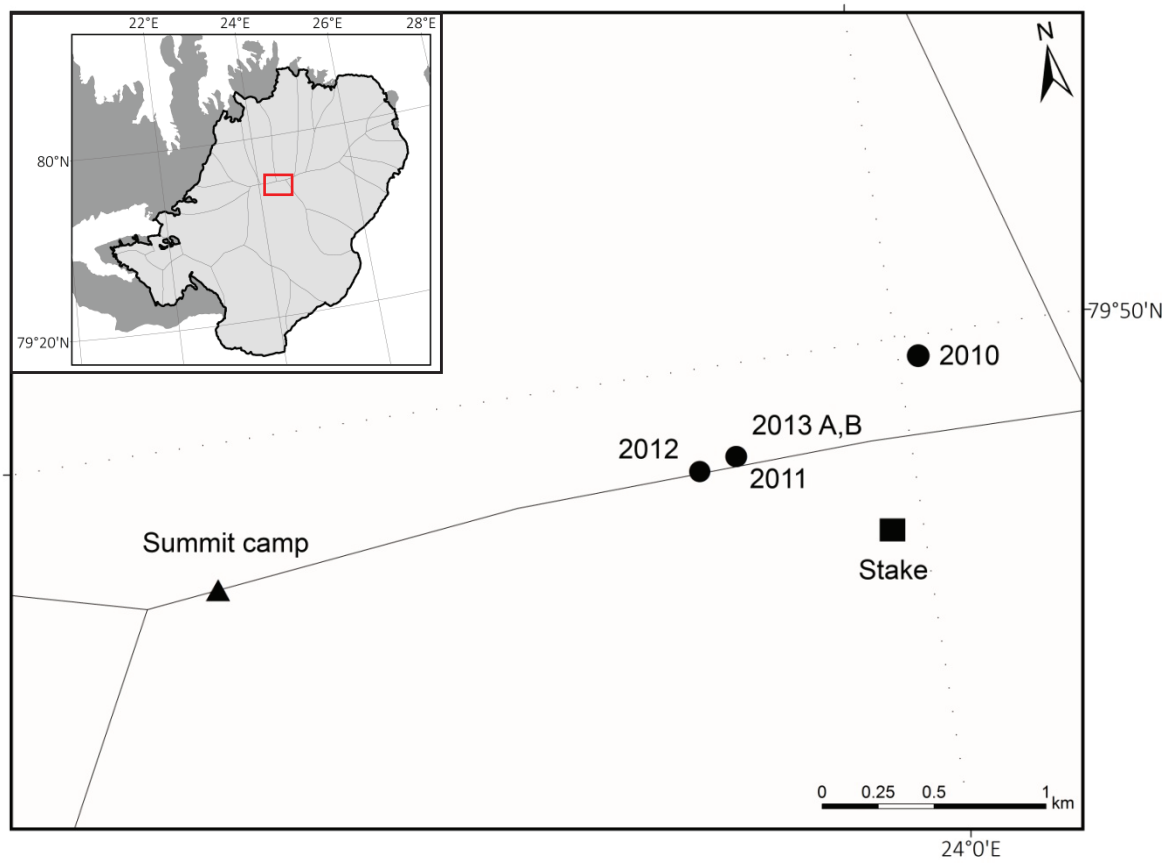

Figure 5: Location of the marked mass balance stake and the boreholes of the analyzed videos. The Summit camp (black triangle), the stake "Even" (black square) and the boreholes from 2011, 2012 and 2013 A, B (black dots) are shown along the ice divides (gray lines) (Moholdt and Kääb 2012). The 2011 and 2013 A, B boreholes are situated to close to be distinguishable from each other in the map. A firn core was retrieved at the location of the 2010 label, but no borehole camera video.

The videos were recorded from the snow surface or the top of the LSS below the snow pack, respectively. In three of the analyzed videos (2012, 2013 A, B) the mirror was attached to the casing and visible below the camera lens. The video from 2011 was recorded without the attachment. Depending on the operator the duration of the recording varies from 102 (2013 A) to 922 (2012) sec as well as the overall number of frames per video of 3330 to 28350. The logged depth range differs from 8.5 m in 2011 to 14.3 m in 2013 (A) (Table 3 in appendix).

4.1.2 Set-up and field operation

In the years 2011 to 2013, the Junior Ultra Low Light camera from Marks products, Inc., now listed under the name Allegheny Instruments Inc., was used during field work on the Austfonna Ice Cap (Figure 6). The plastic coated camera records grayscale videos. Eight light-emitting diodes (LEDs) are integrated in the downward-looking camera system, which is approximately 4.5 cm thick. The 2.9 mm wide angle lens is glass covered and provides a adequate video quality for close-up images (Allegheny Instruments 2012, Marks Products 2014). The video camera system has a square-shaped mirror attached to the casing (Figure 8), which provides the user

with the option to observe the borehole wall laterally. The camera is connected to the control panel by a GeoVISION™ standardized cable, which is hauled over an OSD (On-Screen Depth display) encoder by a steel, hand operated winch. The depth of the camera in the borehole is automatically displayed as a digital number in the video frames. With a joint monitor, real time acquisition and observation of the borehole is feasible directly at the field site. The electronic equipment (Figure 6) is stored in a waterproof case to protect it from the cold conditions on the glacier (Allegheny Instruments 2012, Marks Products 2014).

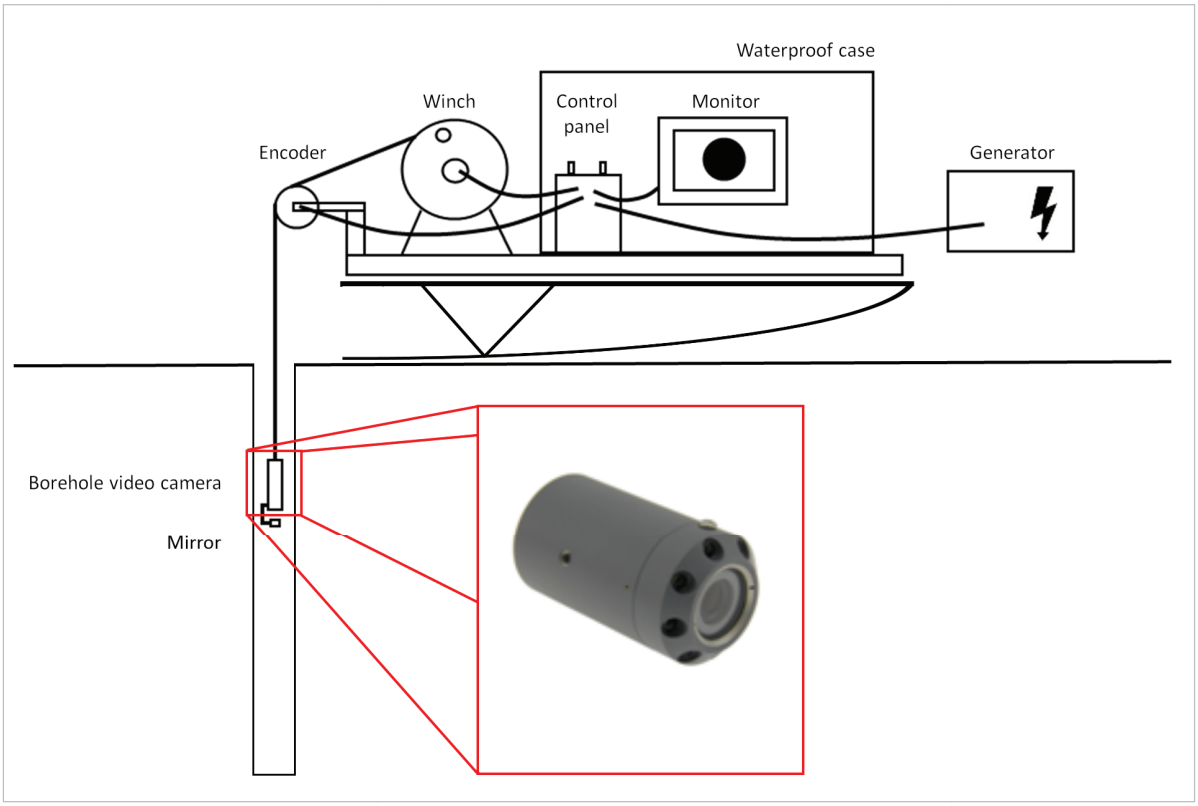

Figure 6: Borehole video camera set-up used on the Austfonna Ice Cap from 2011-2013. The instruments are mounted on a snowmobile sledge while the camera is lowered into the beforehand drilled borehole. The red box depicts a close up of the video camera device without the attached mirror, metal holdings and cables. The image of the device is taken from Allegheny Instruments (2012).

The boreholes were drilled with a mechanical, hand stabilized Kovacs ice auger or coring system (Kovacs Enterprise 2014). To register the depth below the surface, a measuring tape or the attached encoder of the camera system was employed. While the video camera was lowered down into to borehole, the monitor was observed to prevent potential damaging of the instrument. In case of lens fogging or covering of the mirror with ice chips, the camera had to be hauled to the surface again to clean the equipment. Due to the missing centralizers on the system, the video cable needed additional stabilization. This was achieved by the handle of a shovel that was anchored above the borehole.

An important detail of the operation process is the cleaning of the borehole prior to the insertion of the video camera. The borehole wall has to be brushed to reduce the amount of adhered ice

chips. This process increases the video quality and prevents disturbances of the recording process. During the field campaign an ordinary toilet brush was utilized. It was fixated on snow probes, which were taped together.

4.1.3 Video properties

The Junior Ultra Low Light video camera has a standard NTSC (National Television Systems Committee) resolution of 720 x 480 pixels (aspect ratio 4:3). The frame rate is 30 images per second and the system records the video (.avi file) in black/white (Allegheny Instruments 2012). A black pixel has the binary grayscale value of 0, whereas white has the maximum number of 255 for a 8 bpp (bit per pixel) color code. All of the analyzed videos in this study are from coring boreholes with a diameter of 8 cm, except for one (2011). The latter was recorded in an ice auger borehole with a diameter of approximately 5 cm. The borehole video camera was lowered down to the bottom and the depth encoder was set to zero manually. During the hauling process, the camera logged the borehole wall.

The video shows a downwards view into the borehole (Figure 8). The borehole walls and the measuring tape are clearly visible. White zones represent snow and firn deposits, whereas darker bands in the borehole wall characterize ice layers.

4.1.4 Data processing and tools

The primary aim of the video data processing is the extraction of depth-specific intensity values. A continuous horizontal log of the borehole wall has to be produced from a video camera in a down-looking position. Brandt (2014) introduced a self-made borehole camera system to the glaciology section of the University of Oslo in 2008. Since then the system was changed to a commercial borehole video camera set-up and employed in the field. In the context of this study a new processing program has been developed in MATLAB® (2013). Several functions have been computed to create a continuous intensity record, which is dependent on the specific depth value for each video frame of the video.

Before the borehole camera videos could be analyzed, they had to be preprocessed. The algorithm is designed to read the video from the snow surface towards the bottom of the borehole. Our field data was collected in the opposite direction. The camera was hauled up from the bottom. To process the videos, they had to be reversed with a standard video editor software and transformed into .ogv files. The depth is automatically logged by the OSD encoder and displayed in the borehole camera video in meters and decimeters.

A training program (Figure 7) initializes an automatic detection of the depth value in the video, which can be implemented for any borehole video recorded with the described camera set-up.

The Borehole camera analysis tool is the centerpiece of the processing program and comprehends the input and output, the self testing depth calculation and the intensity extraction algorithms.

The borehole wall intensity values are extracted in every frame either from the image periphery or from the mirror. The combination of depth with the intensity values for each frame results in an accurate data set of the intensity distribution along the borehole log. Figure 7 illustrates the processing chain, which is described in more detail in the following sections.

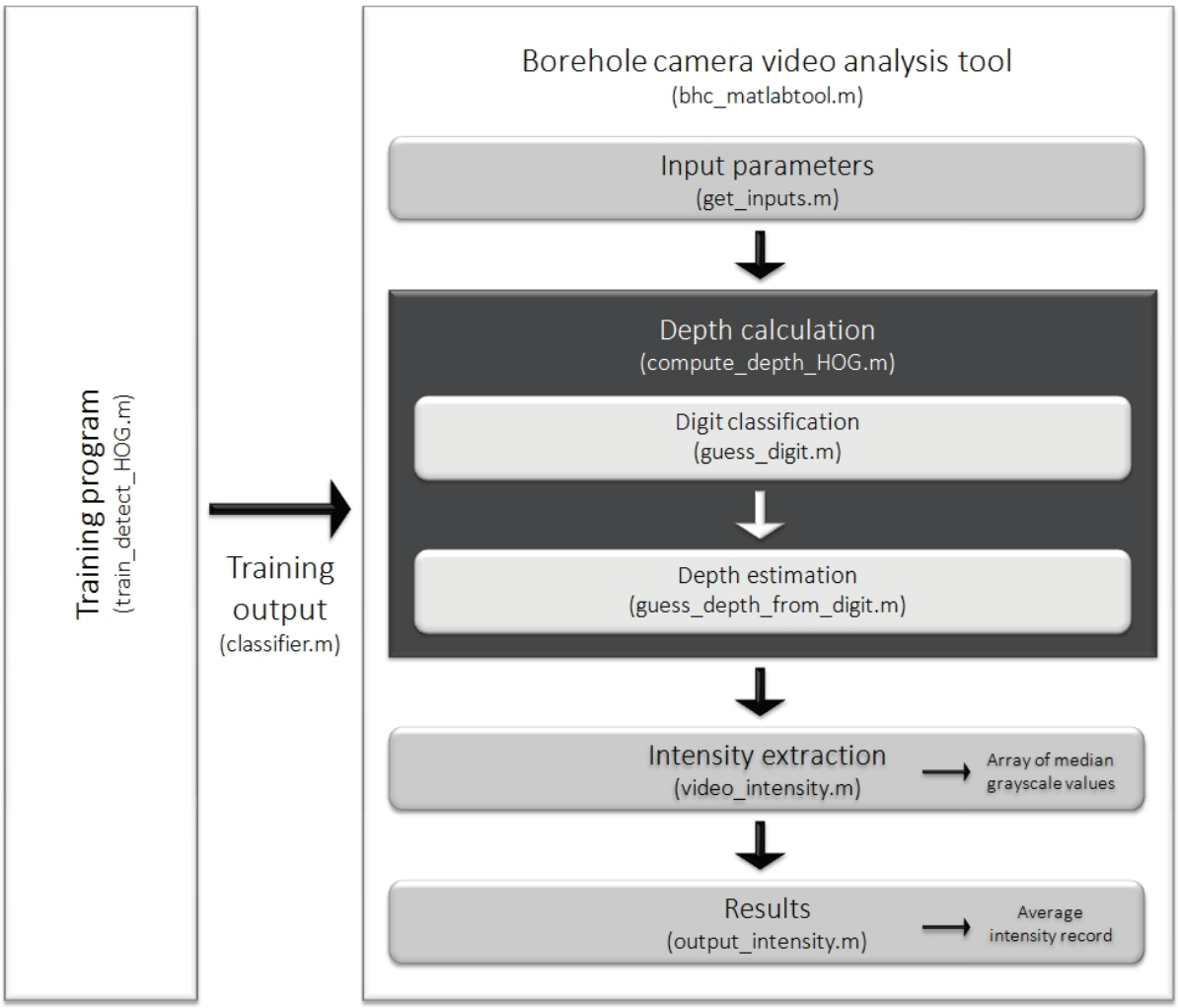

Figure 7: Overview of borehole video camera data processing chain.

4.1.4.1 Training Program

The video system used on the Austfonna Ice Cap does not provide an independent depth record of the encoder. The display of the depth values in the borehole video is the only indication for the position of the camera below the surface. To relate the depth to the frame numbers, the actual depth values displayed in the video have to be identified. This is achieved by using the extractHOGfeatures.m (HOG - Histograms of Oriented Gradients) from the Computer Vision System Toolbox™ and the svmtrain.m algorithm from the Statistics Toolbox™ in MATLAB®(2013). The program train_detect_HOG.m (Figure 7) is necessary to guarantee that every borehole video, recorded in the past or future with the above described set-up, is processable and the intensity logs are correlated with depth.

Each frame in the video displays a depth value in meter and decimeter. The decimeter number of the depth value, ranging from 0 to 9, is saved as an image (training image). In the next step the extractHOGfeatures.m function assigns shape information to all training images. The shape of the decimeter number in each frame is characterized by 'HOG feature' vectors; a general tool for object detection in digital images. These information are stored as training features.

To clarify, which digit is seen in the original frame, numbers of 0 to 9 are assigned to the training features. Therefore, the features represent the decimeter value in the video.

The SVM (Support Vector Machine) classifier (svmtrain.m) registers each 'HOG feature' pattern and its associated digit. By knowing the shape of a number and its specific value, the decimeter digit in a video can be registered as number between zero and nine and stored in a depth data set.

The videos are recorded in grayscale, which can cause problems for the SVM classifier. The depth logger value is a white number that is displayed in the foreground. Firn layers and the inserted measuring tape in the borehole cause bright areas in the video and decrease the contrast between the depth value and the background. As a result the SVM classifier is not always able to detect the correct digit. In general it is advised to enhance the contrast of the video and to restrict the size of the training images to the dimension of the depth value.

4.1.4.2 Borehole camera video analysis tool

The main program to analyze the borehole camera videos (Borehole camera video analysis tool, Figure 7) extracts the encoder digits and intensity values in each frame in order to correlate the depth profile to the borehole wall intensity. The output (classifier.m) from the training program is required to run the borehole camera video analysis tool (bhc_matlabtool.m). To determine the intensity values in a particular section of the video, the first and last frame have to be defined manually.

A search window is used to extract the intensity from the borehole wall (Figure 8 and Figure 9 (A)). The get_inputs.m function (Figure 7) provides the user with the ability to select the image coordinates for the intensity detection (Figure 8), while showing the start frame as a background image. The center search window has a size of 120x20 pixels, whereas the side window contains 20x120 pixels, respectively.

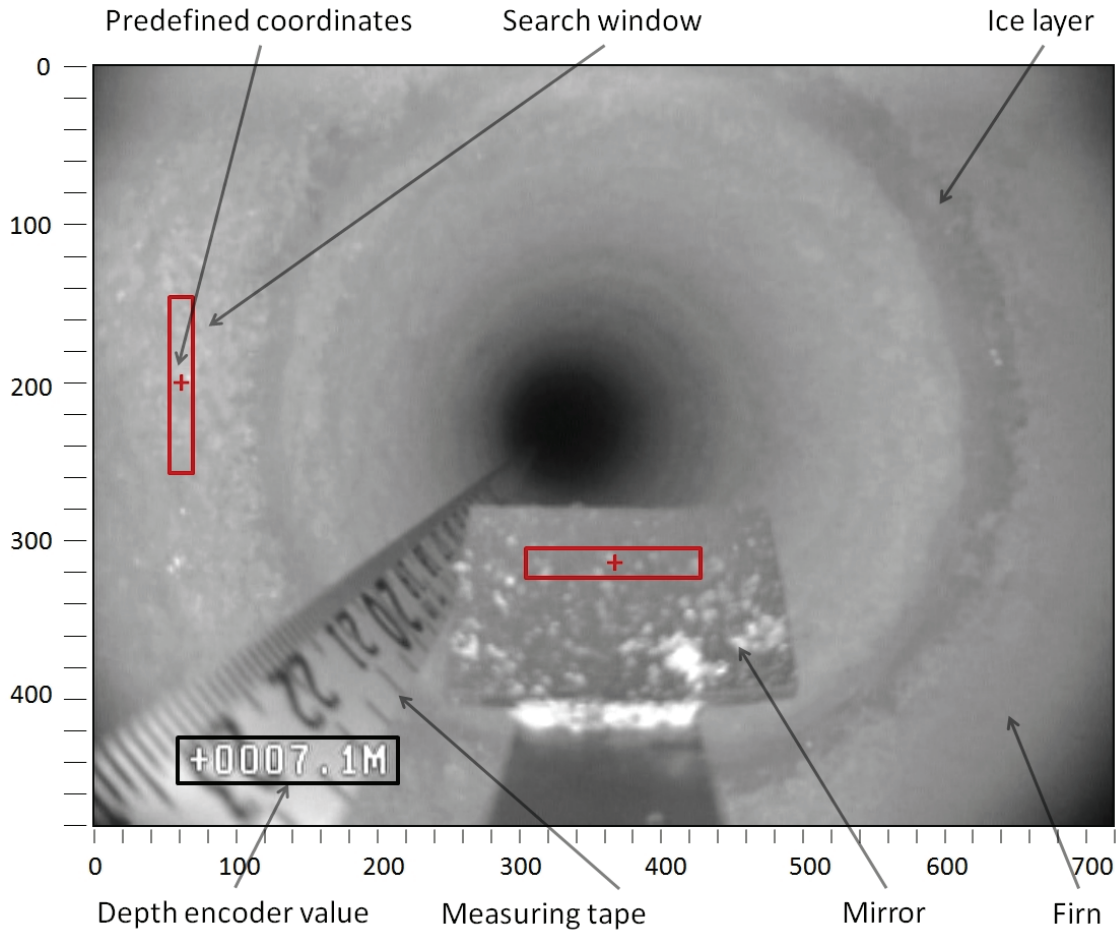

Figure 8: Video frame from the borehole camera video. The attached mirror is visible in the middle of the lower section of the image. The depth is displayed in the foreground (black) and the exemplary search windows (120x20 pixel) are marked in red (center window = horizontal, side window = vertical). The plus in the center of each search window defines the selected image coordinates for the intensity detection.

Preferably, the center intensity is registered in the mirror area, while the side intensity is recorded at the borehole wall. The center of reference should be positioned in an area which is not covered by the measuring tape throughout the video (Figure 8).

The compute_depth_HOG.m function (Figure 7) uses the SVM classifier to extract the depth values from the video and to construct a depth profile. The work flow is similar to the training program with the exception that the extracted digits are validated. The HOG feature vectors are generated as mentioned above, classified into digits from 0 to 9 based on the training program output (classifier.m) and registered as preliminary labels.

The user provides the algorithm with the depth of the start frame. The function guess_digit.m in the depth calculation tool tests the reliability of the preliminary labels. The procedure is necessary to prevent a wrong numbering caused by the occurrence of gaps and inaccurate classification. In the next step, the guess_depth_from_digit.m function assigns each frame a depth value in meters and decimeters according to the prior classified digit for the frame.

Dependent on the hauling speed of the camera along the borehole, several frames show the same decimeter depth value in the video. Depth values in centimeter and millimeter scale are linearly interpolated over the number of frames with same decimeter digits. The result is a continuous depth record and movement per frame profile along the borehole wall.

To extract the intensity from the video, the video_intensity.m function is executed. The defined narrow search window around the previous selected coordinates in the start frame determines the survey area in the video image (see B in Figure 9). The output of the intensity extraction is an array (120x1) of median grayscale values, which were derived from each column of pixels in the window matrix (C in Figure 9). To interpret the intensity in the subsequent analysis, the median numbers are averaged to one intensity value $\bar{x}_{int}$ for every frame. In addition, the standard deviation σ_{int} (STD) of the average intensity is calculated (D).

4.1.5 Analysis

The average intensity signal is normalized and smoothed into 1 cm intervals to reduce signal noise. Amplitude fluctuations, which occur in a smaller depth range than 1 cm, are considered not to be related to the firn-ice changes.

The brighter the sections in the video, the higher is the intensity and probability that the borehole wall consists of firn. Darker zones represent ice layers and lenses. Therefore the intensity record is classified automatically into firn and ice sections using a threshold value (I in Figure 9). A more detailed description of the threshold and the analyzing process will be presented in chapter 5.3.4 Observed and recorded firn-ice distribution.

To compare the position and thickness of ice layers derived by the borehole camera system with ground truth firn stratigraphy records, the video and firn core logs are digitally aligned to cover the same depth range (J in Figure 9). Furthermore, the amount of ice in the borehole camera stratigraphy log is compared to the quantity of ice layers in the firn core record. The movement of the camera along the borehole is calculated as well according to the depth value per frame.

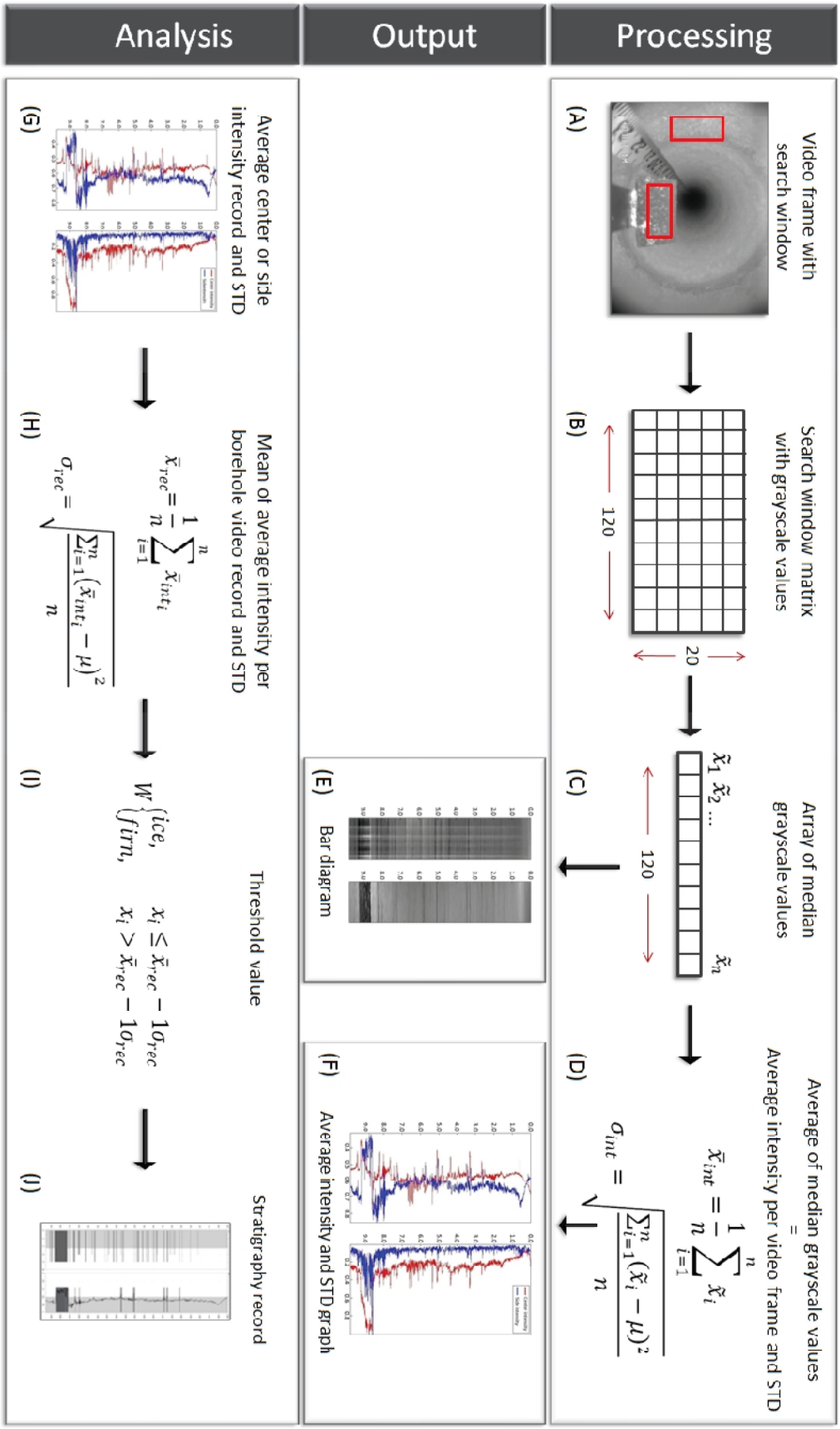

Figure 9: Scheme of the processing and analysis workflow.

4.2 Firn core stratigraphy

The data set consists of four cores from the years 2010-2013 (Table 4 in appendix). All of the cores we obtained by the glaciological field team of the University of Oslo during the field seasons in spring (Figure 5). The aim of the core drilling was to retrieve a density and stratigraphy log from the snow surface to the firn-ice transition. The length of the cores (diameter 7.8 cm) varies from 8.00 m to 14.78 m. In 2013, the transition between the firn and ice was reached. It remains unclear, if the firn core from 2010 and 2011 cover the total range, whereas it is likely for the 2012 firn core.

The shallow cores were drilled with a standard coring system (Kovacs Enterprise 2014) from the snow surface directly or the LSS at the bottom of a snow pit, respectively. The core pieces with a maximal length of 55 cm were weighed with an electronic balance and the length measured in the field. The wrapped core pieces were transported in styrofoam boxes with from the Austfonna Ice Cap to the Norwegian Polar Institute in Tromsø, Norway.

In the cold laboratory of the institute the core pieces from 2010, 2012 and 2013 were cleaned from ice chips, photographed with a camera and the length remeasured. The stratigraphy was visually analyzed in 0.5 cm intervals. The 2011 firn core was investigated by Carmen Vega Riquelme, Uppsala University. Firn sections were categorized according to the grain size, ice layers and lenses registered. Furthermore frozen meltwater intrusions, the approximate bubble size in the ice layers and changes in material color were documented.

Uncertainties in the length measurements of the core pieces can occur, when drilling chips are compressed onto the core or pieces break off during the hauling process or transport. The 2011 firn core shows indication for material loss, since the length measured in the field (8.86 m) exceeds the one measured in the cold laboratory by 0.86 m.

The firn cores serve as ground truth validation for the borehole camera intensity-derived firn stratigraphy and evaluation of the specific mass balance. In order to compare the borehole camera intensity record with the ground truth core stratigraphy, the log was resampled into 1 cm intervals. Hence, ice layers thinner than 1 cm are underrepresented. Further, the bulk density, the mass divided by the volume of each core piece, was calculated for the cores 2012 and 2013.

4.3 Mass balance stake

The Austfonna Ice Cap is covered with a network of mass balance stakes (>25). The stakes are installed in the ablation and accumulation area. The specific surface net mass balance b_n and winter mass balance b_w is remeasured every year by a research team during the field season in April-May 2008-2013. Severe snow deposition, strong winds that bend the metal pole to the ground and melt out, can complicate the measuring of the LSS and the snow pack height along the stake. Bad weather conditions, crevasse opening and the ongoing surge in Basin 3 can hinder continuous measurements. The mass balance stake 'Even' (Lat.: 79.825327, Long.: 23.9906485) is located less than 800 m away from the firn core borehole from 2010 - 2013 (Figure 5). The change in distance from the stake top to the snow surface and LSS during the observation period was used to estimate the specific surface mass balance components.

5. Results

5.1 Specific surface mass balance from firn cores and mass balance stake

The accumulation area of the Austfonna Ice Cap is comprised of the wet snow zone and merges into the percolation zone. In the summer months (June, July and August) wet snow deposition, rain events and surface melting might occur at higher elevations. The meltwater produced at the surface percolates into the underlying snow pack and the firn. The pore spaces are infiltrated and the densification processes proceed. Hence the firn below the old snow surface and the LSS consists of a complex pattern of ice layers, pipes, lenses and firn sections.

Surface mass balance estimates are based on the assumption that the firn underneath the old snow surface is a homogeneous continuum with an assigned density measure. In general, the assumption underestimates the surface mass balance because the occurrence of refrozen meltwater in snow during the summer months is neglected.

To evaluate the discrepancy, the specific surface winter b_w (September-May) and net b_n mass balance for the years 2009-2012 are calculated with the standard (b_n standard) as well as the firn-ice fraction method (b_n fraction), which considers the firn core stratigraphy from 2010-2013.

The winter balance b_w is estimated by multiplying the depth of the snow pack with an empirical density value of $\rho = 0.375$ g cm^{-3} for the years 2009 and 2010 and with $\rho = 0.390$ g cm^{-3} for 2011 and 2012, respectively. For the standard calculation of the net mass balance b_n (b_n standard), the change in height of mass balance stake in respect to the LSS is multiplied with the density of firn ($\rho = 0.540$ g cm^{-3}). The firn density was derived from the average of bulk sample densities of the 2012 ($\rho = 0.507$ g cm^{-3}) and 2013 ($\rho = 0.573$ g cm^{-3}) firn cores.

The enhanced estimation of the net mass balance performed in this study distinguished between the firn and ice fraction below the old snow surface until the depth of the previous year's summer surface. The exact measurement of the firn content and imbedded ice agglomeration thicknesses improves the accuracy of the net mass balance (b_n fraction) calculations. The density of ice ($\rho = 0.870$ g cm^{-3}) is estimated from the bulk densities of the 2013 core pieces, which are retrieved from below the firn-ice transition. The summer balance b_s is calculated as the difference between b_w and b_n (Table 1). All mass balance values are transferred into water equivalents (cm w.eq.).

The record of the specific mass balance of the years 2009-2012 (Figure 10) reveals a maximum winter balance b_w of 62.4 cm w.eq. in 2012 and a minimum of 46.8 cm w.eq. in 2011. The mean

value of the winter mass balance is 54.6 cm w.eq.. The values vary throughout the observation period. No considerable trend in the winter mass balance is observable.

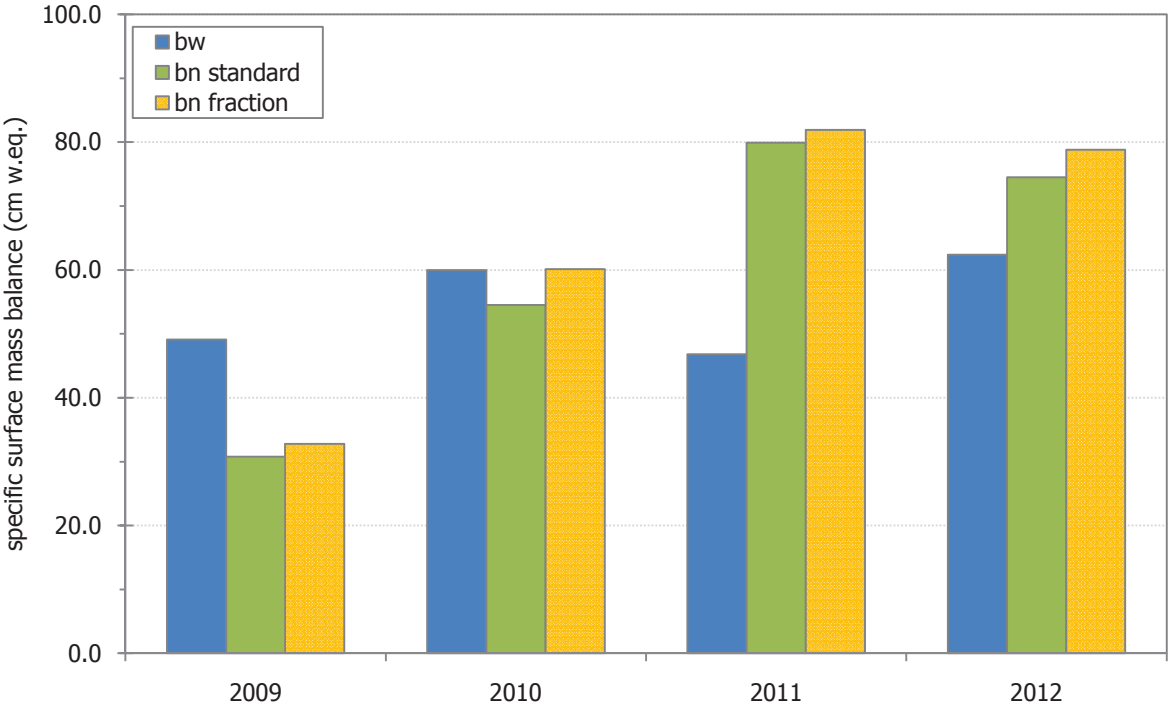

Figure 10: Specific surface winter $\boldsymbol{b_w}$ and net $\boldsymbol{b_n}$ mass balance (cm w.eq.) derived at the summit of the Austfonna Ice Cap. $\boldsymbol{b_n}$ standard was calculated by assuming a homogeneous firn, whereas $\boldsymbol{b_n}$ fraction distinguishes between the amount of firn and ice.

In contrast, the specific net mass balance b_n increases in the years 2009-2011 to the maximum of 79.9 cm w.eq. (81.9 cm w.eq., b_n fraction) and decreases in 2012. The findings indicate an overall underestimation of the specific net mass balance of -5.8 % by the standard method, if the fraction method is considered to produce accurate results. The mean of firn-ice fraction net mass balance (63.4 cm w.eq.) is 3.5 cm w.eq. higher than the standard net mass balance (59.9 cm w.eq.) (Table 1).

The greatest difference is seen in the year 2010 (Figure 10). Ice agglomerations imbedded in the snow pack that endured the ablation season, cover 20% of the depth range and the specific net balance is underestimated by -9.3 % (Table 1). While the standard method suggests a smaller b_n than b_w balance and therefore a negative summer balance b_s, the firn-ice fraction method reveals a positive summer balance with a higher net mass balance. The case indicates how necessary the accurate measurement of the refrozen meltwater is for surface mass balance estimates. In the years 2011 and 2012, the specific net balance (b_n fraction) exceeds the winter balance by 35.1 cm w.eq. (75 %) and 16.4 cm w.eq. (26 %), respectively. Hence the specific summer balance is positive for these years. In 2009, the calculated summer balance is negative with -18.3 cm w.eq., b_s standard (16.4 cm w.eq., b_s fraction) and therefore the net mass balance is smaller than the winter balance for both methods.

Table 1: Specific winter b_w, summer b_s and net b_n (standard, fraction) surface mass balance at the mass balance stake 'Even' in the summit area of the Austfonna Ice Cap

	b_w (cm w.eq.)	b_n standard (cm w.eq.)	b_n fraction (cm w.eq.)	firn content (cm)	ice content (cm)	b_n fraction - b_n standard (cm w.eq.)	b_n fraction - b_n standard(%)	b_s standard (cm w.eq.)	b_s fraction (cm w.eq.)
2009	49.1	30.8	32.8	51.0	6.0	2.0	6.0	-18.3	-16.4
2010	60.0	54.5	60.2	84.0	17.0	5.6	9.3	-5.5	0.1
2011	46.8	79.9	81.9	142.0	6.0	2.0	2.4	33.1	35.1
2012	62.4	74.5	78.8	125.0	13.0	4.3	5.4	12.1	16.4
$\bar{x}$	*54.6*	*59.9*	*63.4*	*100.5*	*10.5*	*3.5*	*5.8*	*5.4*	*8.8*

5.2 Change in accumulation-area firn stratigraphy

The specific mass balance estimates in the summit area of the Austfonna Ice Cap (Figure 10) illustrate a highly variable net mass balance during the observation period. The firn cores of 2010-2013 exhibit the stratigraphic record of the firn from 2009-2012. The growth and repositioning of ice layers is related to the amount of produced meltwater at the surface and the percolation and refreezing of water in the firn. Since the mean annual air temperature on the Austfonna Ice Cap is below -8°C, rainfall and meltwater in the summer time is considered to infiltrate pore spaces in the firn column and refreeze at lower depth. Due to the varying meteorological conditions, the densification of snow on the ice cap is dominated by refreezing of meltwater in the pore spaces rather than settling and compression.

The visually derived stratigraphy for each firn core is displayed in Figure 11. To trace the number and position of ice layers in the same depth interval through time, the logs are aligned according to the summer surfaces of particular years. The mutual basis is the summer surface of the year 2006. The longest record (2013) extends over a length of 7.0 m and comprises six sections of accumulated firn mass, each deposited in one seasonal cycle. Thickness changes of the firn and ice layers due to settling, compaction or flow-induced layer thinning are neglected in the comparison of the stratigraphic logs through time. The stratigraphy is derived at a 1 cm resolution and ice lenses and layers are not treated separately. Therefore the amount of ice is overrepresented in Figure 11, if ice lenses were observed in the original firn core record. Due to the given resolution, ice layers thinner than 1 cm are not displayed. The top of each firn core is leveled with the upper most LSS for the particular year of drilling (e.g. LSS 2012 for the 2013 core, LSS 2010 for the 2011 core).

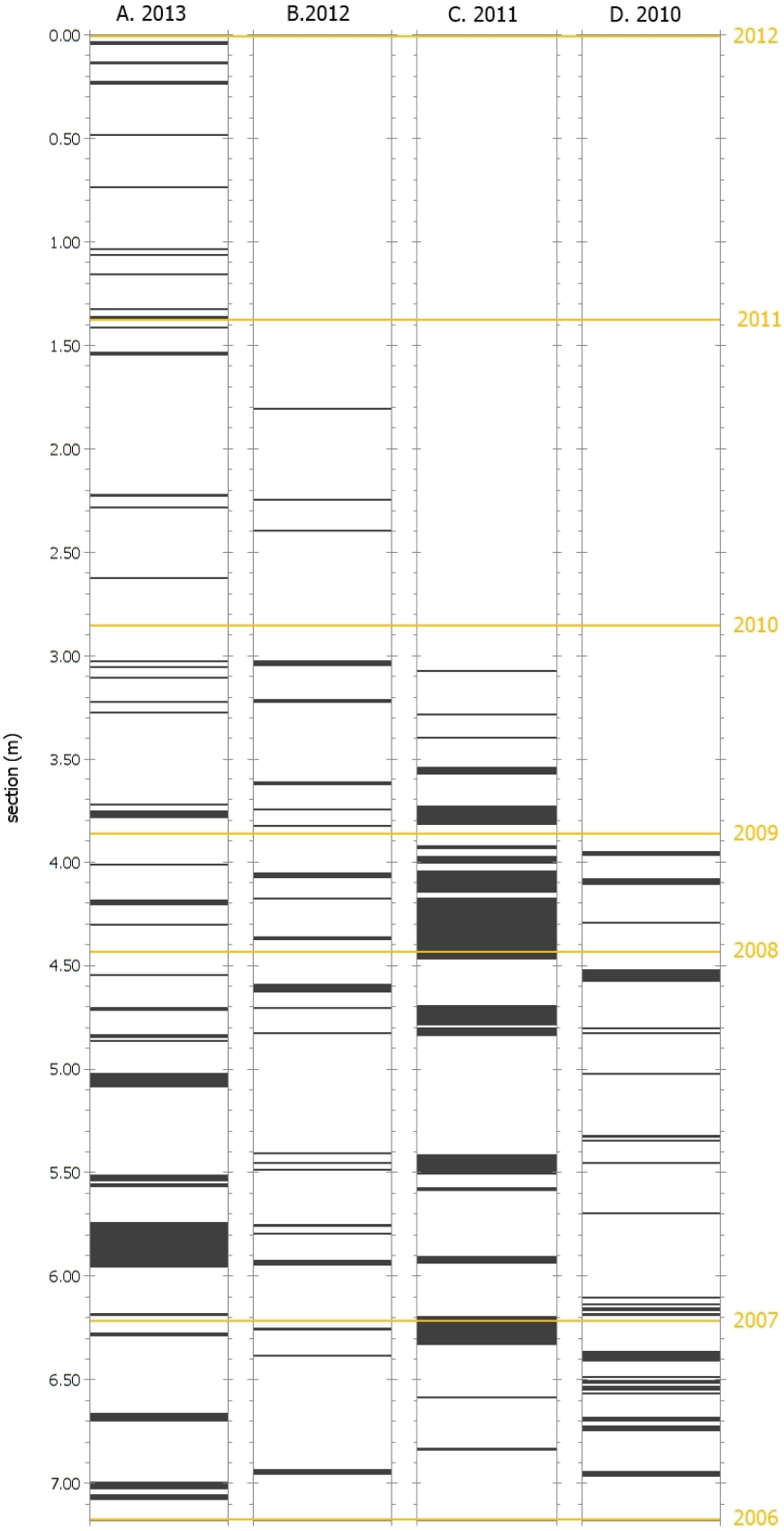

Figure 11: Stratigraphic record of the firn at in the summit area of the Austfonna Ice Cap. Ice layers are shown as dark horizontal bars. The logs (2010-2013) are aligned by the depth of the summer surface (yellow lines) for particular years to compare the change in ice layer content and location in the firn. The y-axis represents the length of the section of the firn core and not the individual depth of the LSS below the true surface.

Comparing the ice fraction in the firn core intervals between the summer surface interfaces, the overall distribution and thickness of ice layers is inconsistent throughout the records. However similarities can be observed.

Ice layers are found in each interval below the first LSS and the previous year's summer surface. None of the sections contains a homogenous firn without imbedded ice layers. A major ice agglomeration is shown in the 2011 firn core in the section between the 2008 and 2009 summer surface. The amount of ice in the particular depth interval (37.4 cm w.eq.) is five times as high as in the equivalent firn cores sections (Table 6 in appendix). The other logs do not display such extensive ice agglomerations. In the 2007-2008 section more thick ice layers (> 10 cm) are indicated in 2011 and in the 2013 cores. Otherwise patterns of thick ice agglomeration at a certain depth cannot be traced through the years.

Even though the firn cores were not examined according to predefined firn types specifically, iced firn and percolation features such as refrozen meltwater intrusions (ice glands and lenses) are reported at all depths in the cores 2010, 2012 and 2013.

5.3 Evaluation of the borehole camera video system

5.3.1 Product of the video processing program

The borehole camera video analysis tool generates a continuous record of the borehole wall intensity. As a result of the processing the grayscale values from the search window and the normalized average intensity can be presented in diagrams. The output products of the analysis tool in 2012 and 2013 are displayed in Figure 12 and Figure 13, respectively. The log of the borehole profile in grayscale values is shown in the two graphs on the left. To achieve the record, the arrays of median grayscale values are stacked together according to the depth value of the frames. The width is as long as the search window itself. The average intensity and the standard deviation are presented in the third and fourth graph from the left.

The output of the 2012 video shows a good result of the analyzed videos, whereas the 2013 firn core borehole (A) video output illustrates potential deficiencies. In the 2012 center intensity profile (Figure 12) brighter vertical striping occurs in the entire log. The center intensity was measured on the mirror underneath the borehole camera. By inspecting the video visually, it becomes apparent that ice chips cover parts of the mirror. The chips are captured by the search window as well and disturb the intensity profile as permanently bright area throughout the entire log.

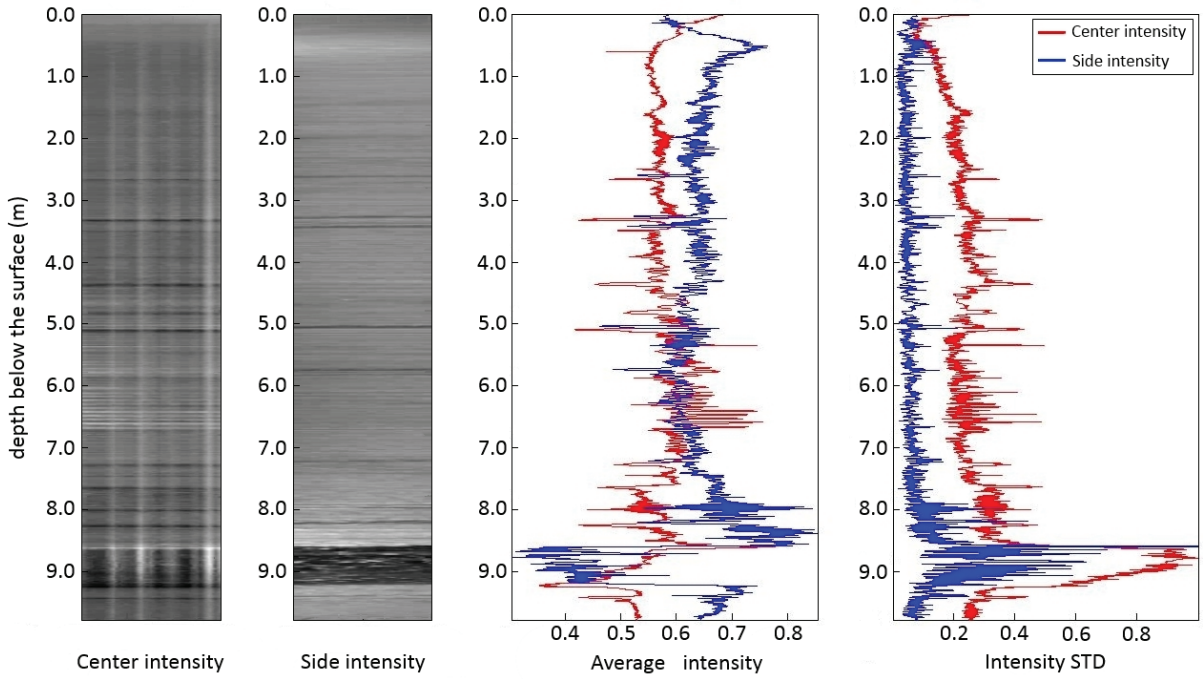

Figure 12: Output product of the borehole camera video analysis tool for the video 2012. In the two diagrams on the left the array of the original median grayscale values for each column of pixels in the search window are stacked together for a continuous log of the analyzed video sequence. In this case, zero at the top of the graphs represents the snow surface. The dark bands in the diagrams characterize ice layers surrounded by brighter firn sections. The normalized average intensity of the center (red) and side (blue) and its standard deviation is shown in the graphs on the right side. The standard deviation represents the variability in the array of median grayscale values.

Ice layers are characterized by dark horizontal lines, because less light is reflected from the wall in these sections. In the 2012 log, a thick agglomeration of ice can be observed 8.6-9.2 m below the surface. The average side intensity shows a strong signal change in this section whereas the average center intensity decreases gradually due to the influence of the brighter ice chips. In general, where ice layers are recognized in the borehole video camera log, the average intensity decreases and the standard deviation increases. At approx. 3.4 m below the surface the center grayscale record shows a darker, more dominant layer, whereas the side record indicates two thinner bands. Overall more dark bands are visualized in the center record than in the side one. Other features are the brighter areas in the side grayscale value record between 0.0 - 1.0 m below the surface and above and below the thick ice layer at the bottom. These are not seen in the center log. In an ideal case the center and side grayscale records should show the same features.

The 2013 firn core borehole (A) video output (Figure 13) gives an impression of poor acquisition and algorithm problems in the analysis process. The video reveals that the borehole camera was swinging during the recording and therefore was not steadily centered. Oscillations in the section between 0.0 – 3.5 m below the surface in the average center and side intensity are caused by the changing light conditions in the borehole.

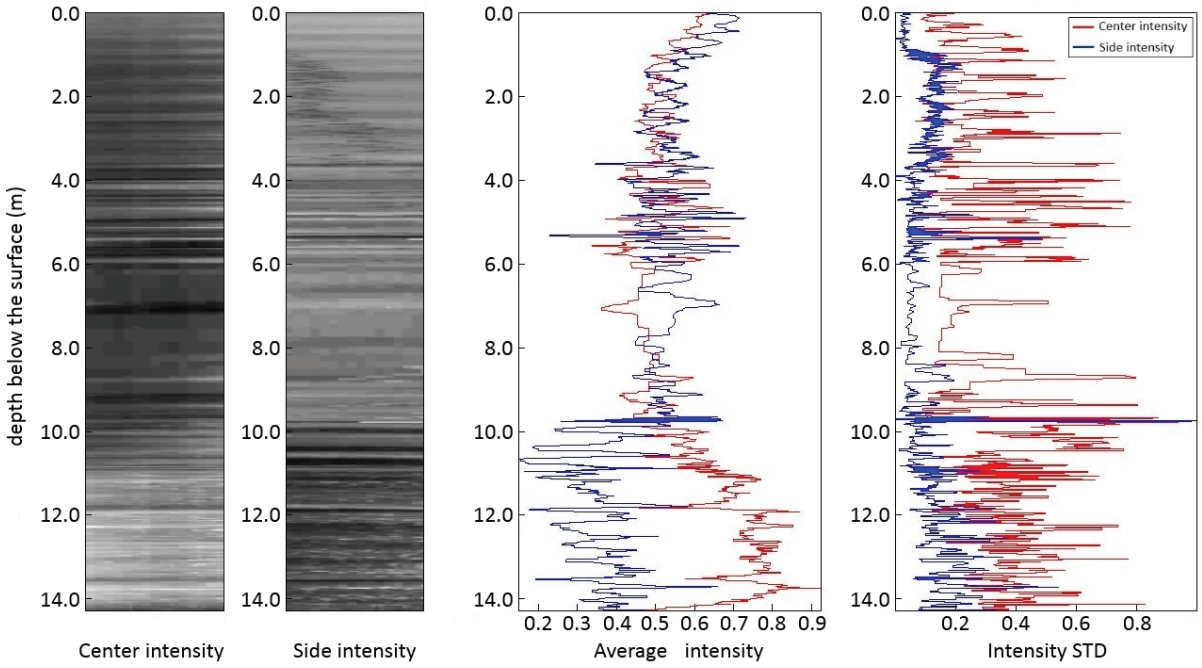

Figure 13: Output product of the borehole camera video analysis tool for the video 2013 firn core borehole (A). In the two diagrams on the left the array of the original median grayscale values for each column of pixels in the search window are stacked together for a continuous log of the analyzed video sequence. The dark bands in the diagrams characterize ice layers surrounded by brighter firn sections. The normalized average intensity of the center (red) and side (blue) and its standard deviation is shown in the graphs on the right side. The standard deviation represents the variability in the array of median grayscale values. In this figure the zero at the top of the graphs represent the LSS.

Visual differentiation between ice layers and shadow features is not feasible for the 2013 firn core borehole (A). Furthermore, the center and side grayscale record contradict each other in the intensity trend throughout the borehole log. While the center intensity increases towards the bottom, the side intensity decreases and the sections become darker. The borehole camera video analysis tool derives the depth for each frame according to the encoder digits in the video. If the background becomes very bright, the algorithm does not recognize the white numbers and the depth approximation fails. This issue is indicated in the section 6.0 – 9.5 m. The grayscale record is distorted and the average intensity graph dispersed. A detailed analysis of this borehole wall segment becomes corrupt.

At the depth of 0.9 to 3.7 m in the side intensity grayscale record ambiguous horizontal lines interfere with the continuous alternations. They are caused by the emergence of the measuring tape in the search window. The video camera was intensively moving in this section so that the measurement tape was captured by the processing algorithm.

5.3.2 Movement profile

The hauling of the borehole video camera is a crucial part of the working procedure in the field and influences the results of the video processing directly. The videos have been recorded by changing operators throughout the field seasons, which is reflected in the video length and total number of frames (Table 3 in appendix). The hauling of the video camera is done manually. To achieve precise depth estimations a consistent movement along the borehole is beneficial. Only constant hauling speed allows for accurate interpolated depth values from the processing software. Figure 14 displays the varying performances per recorded video.

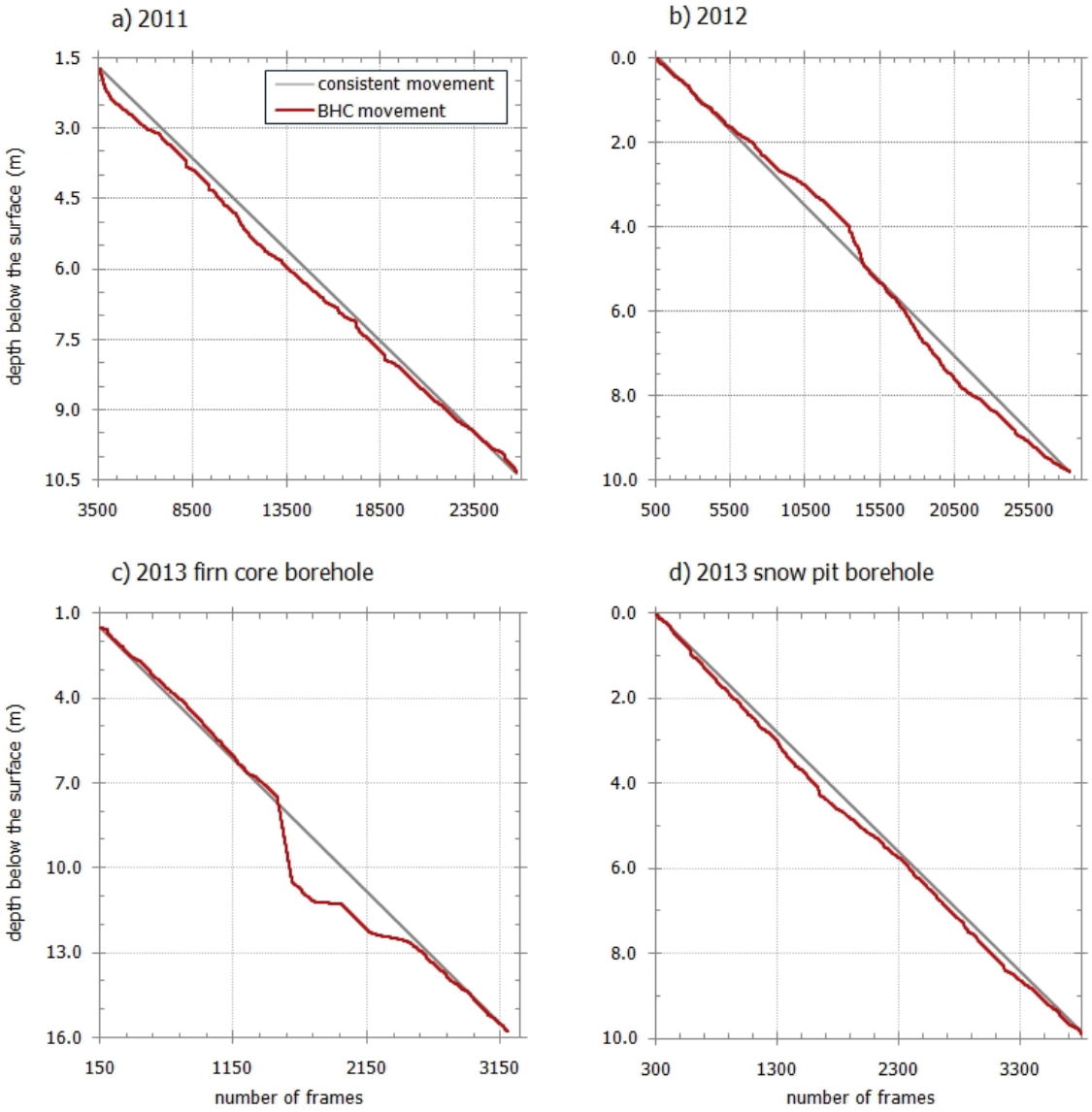

Figure 14: Movement profile of the borehole video camera along the borehole. Depth per frame (red) was derived with the Borehole camera (BHC) video analysis tool. The ideal continuous movement is displayed in gray.

The movement of the camera along the borehole was derived with the borehole camera video analysis tool, which assigns a specific depth value to every frame. The gray lines in Figure 14 represent the ideal consistent movement that would be achieved with an automatic winch system. The length of the analyzed video sections differ from 922 sec in 2012 and 741 sec in 2011 to 102 sec for the 2013 firn core borehole (A) and 116 sec for the snow pit borehole (B) in 2013 (Table 3 in appendix). The time taken to record the videos in 2011 and 2012 is 7 to 8 times longer than for the videos in 2013. The time difference is reflected by the average hauling speed. In 2012, 1.06 cm were recorded in one second, whereas 14.01 cm were covered per second in the 2013 firn core profile. In the field, the video camera was hauled from the bottom of the borehole towards the surface, while it was recording. The video files had to be reversed for the processing. Therefore, the number of frames increases with depth and has a maximum value at the bottom of the borehole.

In the 2012 video the camera was hauled up with an inconsistent speed. The manual movement decreased until approx. 8.0 m and accelerated in the next 2 m until a steady change in position was achieved in the depth interval of 5.0 - 6.0 m. From approx. 5.0 m the camera movement accelerated until 4.0 m was reached. From this depth to 1.5 m below the surface the movement decreased and followed the ideal change in position closely. The 2011 profile reveals several pauses during the hauling process. At 3.8 m and 4.3 m below the surface in the upper section and 7.2 and 8.0 in the lower segment, peaks in the borehole camera movement indicate a halt in the hauling process. In general, the 2011 and 2013 snow pit borehole (B) videos follow a steady movement with less acceleration and deceleration of the camera throughout the entire log. In contrast, the 2013 firn core borehole (A) video profile shows a major offset compared to the ideal consistent movement in the section between 7.5 and 12.5 m below the surface. Two phases with the same trend can be observed in the profile. Between 11.5 - 12.5 m and 7.5 – 11.5, a decrease in movement is followed by a rapid increase in hauling.

5.3.3 Shadow effects and artifacts

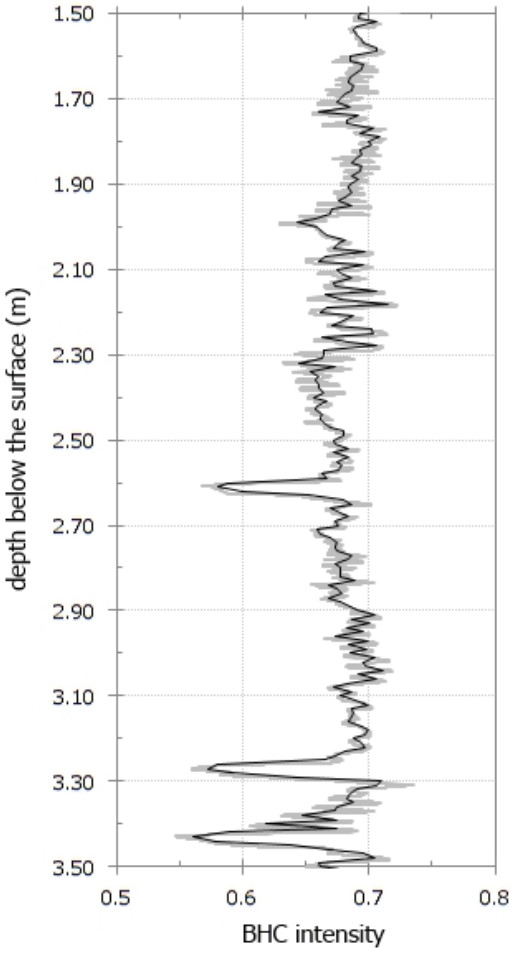

Figure 15: Segment of the raw (gray) and smoothed (black) 2012 side borehole camera (BHC) intensity signal

The borehole camera is a downward-looking system that uses LED to illuminate the area underneath the lens. This set up induces interferences such as shadow effects. The main objective of the video camera is the logging of shade difference of the borehole wall to distinguish between firn and ice areas. The borehole wall is not uniform in shape and the diameter varies. Due to the constant light from above, uneven surfaces and irregularities cast shadows on the borehole wall sections below. These small-scale differences in shading, which are not related to the change in material, are captured by the search window in the video frame. Therefore, they interfere with the stratigraphic intensity signal. To minimize the influence of the shadows on the results, the intensity record was smoothed before analyzing (Figure 15). Variations smaller than one centimeter are eliminated. Peaks, which are most likely related to ice layers, are not affected (e.g. 2.60, 3.25 and 3.45 m below the surface). However, shadowed areas wider than one centimeter in depth are not repressed by this method.

The light of the camera causes other problems as well. As seen in the depth record of the 2013 firn core borehole video (A) intensity record (Figure 13), bright sections of the borehole wall disturb the recognition of the encoder depth values by the processing tool. This happens when the video camera is positioned too close to the borehole wall. Even if the depth digits in the video frame are not affected, more light is reflected off the wall than in the previously recorded section. The intensity record is shifted towards higher values without a change in material. Furthermore any kind of obstacle in the borehole, such as the measuring tape or depth markers degrades the quality and reliability of the intensity log.

5.3.4 Observed and recorded firn-ice distribution

To evaluate the borehole camera videos, the intensity records were analyzed in regard to ground truth firn core stratigraphy profiles. By assessing the agreement between the logs, conclusions can be drawn if the videos are a suitable tool to investigate firn accumulations and ice structures.

Depending on the quality of the borehole camera video, the intensity records of the center and side search window differ. In an ideal camera set-up, both logs display the same grayscale variations along the borehole wall. After examining the raw data (Figure 12, Figure 13), it becomes apparent that the center and side records do not necessarily agree due to set-up issues and borehole wall irregularities. Therefore, only one log per borehole set was selected for the analysis of the intensity-derived stratigraphy. The mean $\bar{x}_{rec}$ of the smoothed and normalized average intensity and the mean of the intensity STD σ_{int} were calculated for the center and side log (Table 5 in appendix). The data set with the lower mean value of the intensity STD was chosen for onward investigations for each borehole. The center intensity was selected for the 2011 video and the side intensity for the remaining videos (Table 3 and Table 5 in appendix).

To derive a stratigraphic record from the borehole video camera data, a threshold value was used to classify firn and ice sections. The threshold value varies depending on the intensity record. To estimate the stratigraphy, the mean $\bar{x}_{rec}$ and the STD σ_{rec} of the smoothed average intensity record are calculated (H in Figure 9, Table 2). The derived numbers determine the individual threshold value for each analyzed video. The borehole wall material W is categorized as ice, if the intensity x_i is lower than one standard deviation σ_{rec} subtracted from the mean of the smoothed average intensity $\bar{x}_{rec}$ of the video record (Equation 4).

$$W \begin{cases} ice, & x_i \leq \bar{x}_{rec} - 1\sigma_{rec} \\ firn, & x_i > \bar{x}_{rec} - 1\sigma_{rec} \end{cases} \tag{4}$$

The borehole wall material is classified as firn, if the intensity is above the threshold. To distinguish the classes, firn is defined as material with open pore space around the grains, whereas the pore spaces are closed off in ice and bubbles can be observed. No differentiation between ice lenses and ice layers was accomplished in the intensity record, due to the limited coverage of the borehole wall in the search window.

5.3.4.1 Comparison of the firn core and borehole camera video stratigraphy

The firn core stratigraphy was derived in the cold laboratory of the Norwegian Polar Institute. Each section in the core pieces was categorized visually into firn with various grain sizes, ice

lenses and ice layers. The structural composition of the entire firn cores aligned with the corresponding intensity stratigraphy logs is shown in Figure 16 -Figure 19. As described above, a threshold value was chosen, which varies depending on the particular smoothed average intensity record (Table 2). The agreement of the two logs is shown in percent. The value increases, if the same class (firn or ice) was observed in the firn core and the intensity-derived stratigraphy in the depth segment of 0.01 m.

Table 2: Threshold value, mean and STD of the selected smoothed and normalized average intensity records of 2011, 2012 and 2013 A and B.

		$\overline{x}_{rec}$	σ_{rec}	**Threshold value**
2011	Center	0.639	0.068	0.571
2012	Side	0.671	0.075	0.596
2013 firn core borehole (A)	Side	0.498	0.118	0.380
2013 snow pit borehole (B)	Side	0.680	0.069	0.611

I. 2011 video intensity and firn core stratigraphy

The 2011 firn core stratigraphy (Figure 16) reveals three ice layers with a thickness of more than 0.20 m (e.g. 3.05-3.35 m, 7.10-7.55 m and 8.75-9.05 m depth below the surface). The remaining twenty-two ice layers are distributed throughout the record with a higher concentration in the top 5.70 m. Ice lenses are registered at approx. 2.00 m, 4.15 m and 7.80 m.

The borehole camera video intensity decreases in the first 2 m of the borehole and increases below 6.20 m in the section which are identified as firn. In the depth range of 3.70-6.20 m the record is steadily at low intensity values between 0.6 and 0.65. Greater amplitude variations in the classified firn areas are shown in the first 1.5 m (3.20 m depth) and below 8.20 m. Those sections contain more ice layers according to the stratigraphic firn core data, which is not reflected in the intensity log. Presumably, brighter ice chips interfere with the darker ice layers and cause the intensity signal to fluctuate to a greater extent, which induces poor agreements (e.g. 36 % in the last meter). The mean value of the agreement is 63 %. The records show the best agreement (95 %) at the depth of 5.70-6.70 m. However, while three thin ice layers are recognized in the firn core stratigraphy record, only one ice layer is indicated by the video camera intensity.

The opposite effect can be observed in the interval between 2.70 and 3.70 m. The firn core stratigraphy presents several ice layers, whereas the video camera intensity does not reproduce the finding. The agreement of the records is poor (40%). A higher agreement of 83 % is found in

the first meter of the log even though no ice layers are registered by the video intensity. The high agreement results from the low amount of thin ice layers in the firn stratigraphy. None of the thick ice layers over 0.2 m are represented in the borehole camera intensity.

At 7.75-7.95 m below the surface the intensity values decline below the threshold, but no ice layer can be found in the same depth range in the firn record. The closest ice agglomeration is located approximately 0.20 m above. The peak at 8.25 m in the intensity could refer to an ice layer, which is shown in the firn core stratigraphy. However, the intensity signal does not decline below the threshold.

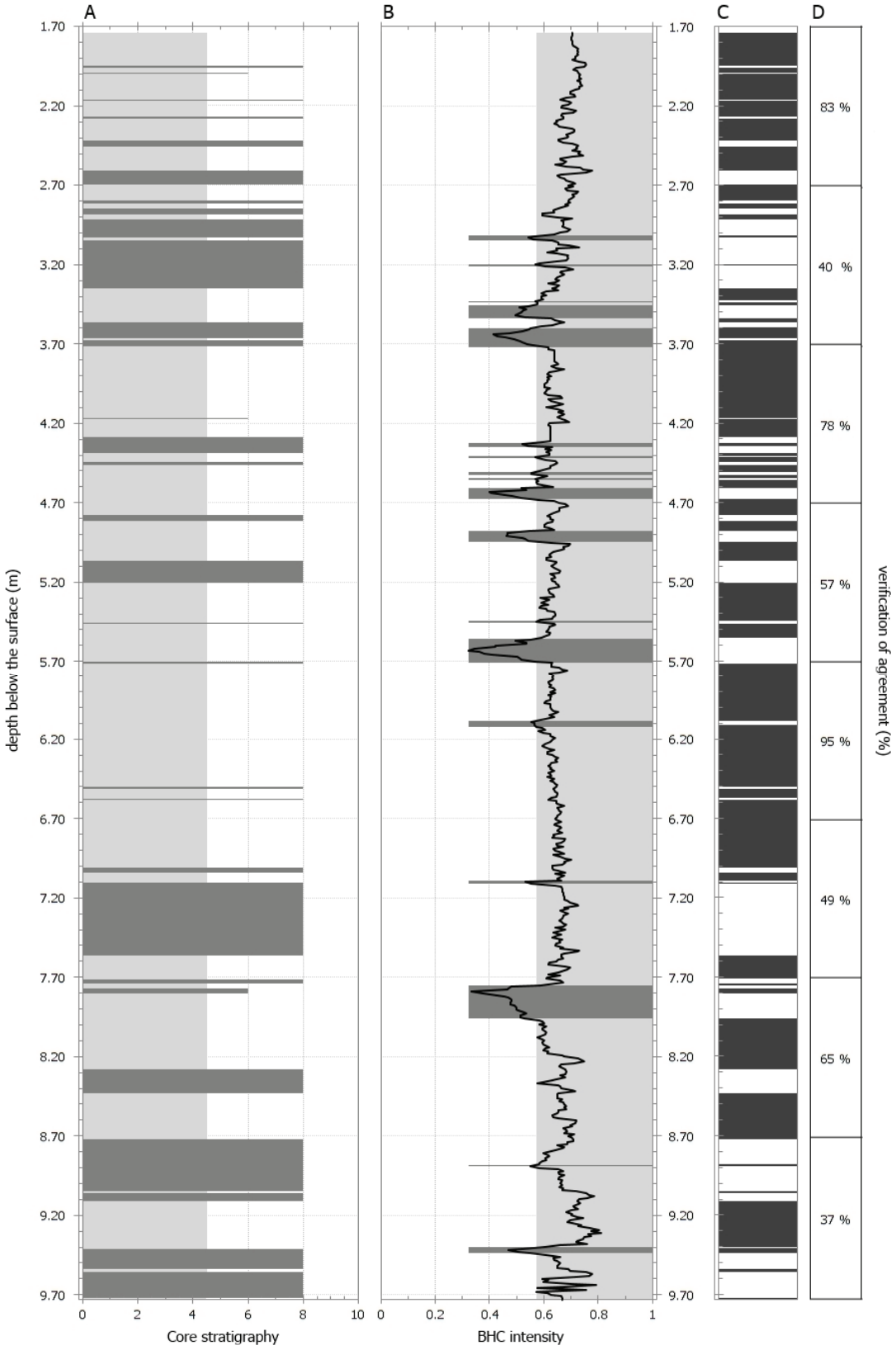

Figure 16: Comparison of the 2011 video intensity and firn core stratigraphy. The ground truth firn core stratigraphy (A) is classified into firn (light gray) and ice (dark gray). The scale of the x-axis is artificial (0-10), but necessary to distinguish between ice lenses (x = 6) and ice layers (x = 8). The firn and ice sections (B) of the normalized and smoothed average intensity record (thin black line) are classified according to the threshold value of 0.571. Note that ice layers in the firn core data are featured by high x-values, whereas ice layers in the intensity record correspond to low x-values. The verification of the agreement of the two stratigraphy records is displayed as visual quantification (C) and percent per depth interval of one meter (D). Black bars represent areas in which both logs show the same material, whereas white bars indicate no agreement. The video was recorded from the LSS 1.73 m below the snow surface.

II. 2012 video intensity and firn core stratigraphy

The borehole video camera intensity increases in the first 0.50 m from the surface and decreases after the turning point until a depth of 5.80 m. From there it increases steadily until the depth of thick ice layer. Compared to the 2011 intensity profile, less large scale amplitude variations are shown in the sections that are categorized as firn. An exception is the depth span between 7.90 and 8.60 m below the surface.

The comparison of the 2012 firn core and video intensity stratigraphy (Figure 17) demonstrates the best agreement (91%) between the two records for all the analyzed data sets. The lowest agreement of 83 % is shown between 8.00 – 9.00 m, whereas the first depth interval (0.00-1.00 m) reveals a 100 % agreement. The ideal conformity is produced by the absence of ice layers in the firn core stratigraphy and intensity record.

One major ice agglomeration is found at 8.65-9.25 m in the firn core profile. The remaining ice layers are thinner than 0.10 m and distributed throughout the log. Eleven ice lenses can be counted as well. The thick ice agglomeration in the lower part of the firn core stratigraphy record is very well reflected in the intensity profile. The indicated layer is shifted approx. 0.05 m towards the surface, but equals the ground truth layer in thickness. In total seven ice layers are suggested by the video intensity log. By comparing the first three ice layers of the video intensity stratigraphy at 2.60, 3.25 and 3.45 m depth, it becomes apparent that those can be observed in the firn core record at the same position in the borehole wall. The other recognized layers might be induced by an assembly of ice layer and lenses or do not correspond to a firn core counterpart.

As seen in the 2011 comparison, several peaks (e.g. at 7.2 m) in the intensity record could represent ice layers, but do not fall below the threshold value. Three peaks between 9.35-9.50 m could be caused by the change in intensity related to the three ice layers recorded in the firn core. However, the peaks are classified as firn and shifted in position towards the surface.

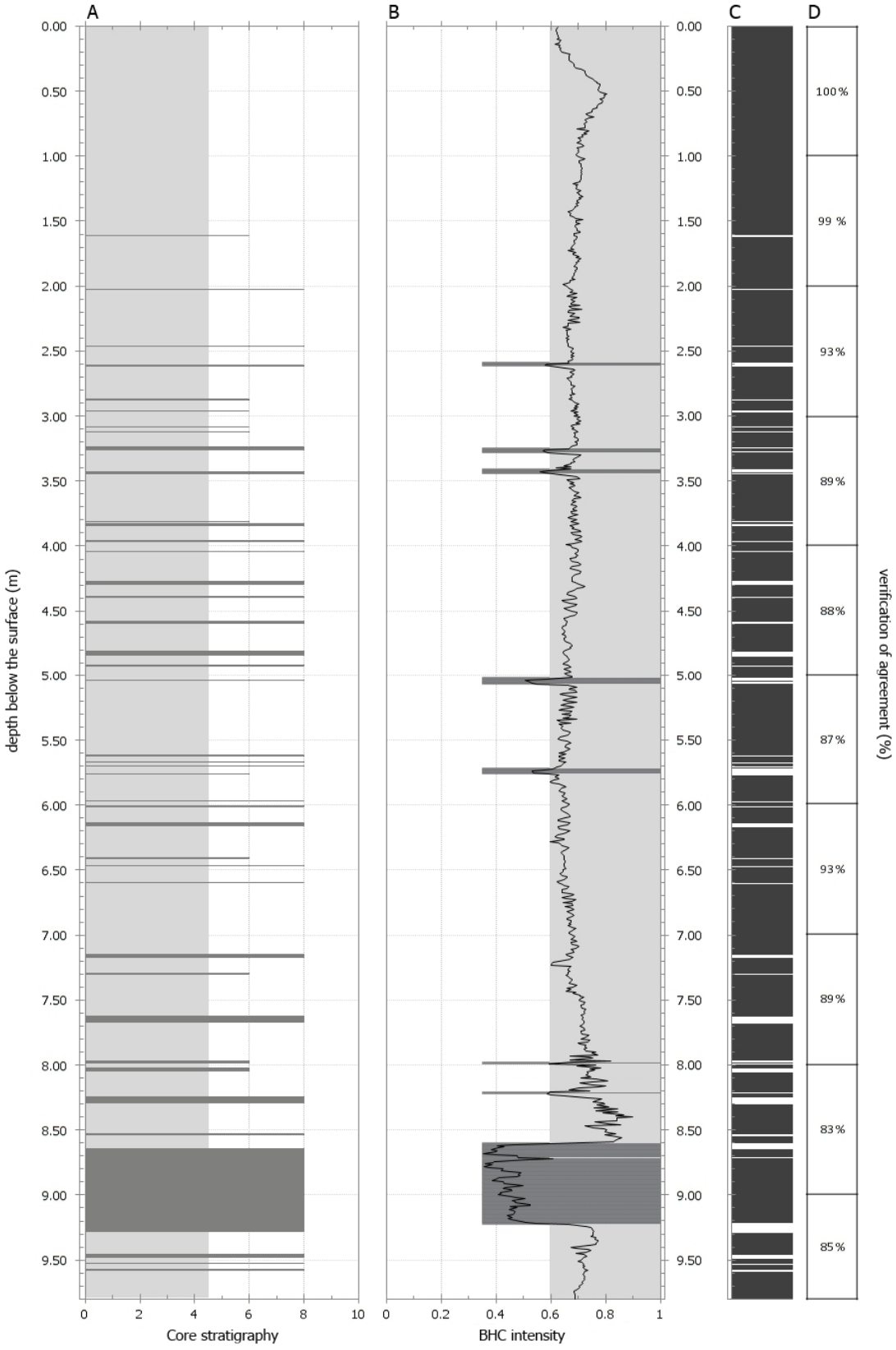

Figure 17: Comparison of the 2012 video intensity and firn core stratigraphy. The ground truth firn core stratigraphy (A) is classified into firn (light gray) and ice (dark gray). The scale of the x-axis is artificial (0-10), but necessary to distinguish between ice lenses (x = 6) and ice layers (x = 8). The firn and ice sections (B) of the normalized and smoothed average intensity record (thin black line) are classified according to the threshold value of 0.596. Note that ice layers in the firn core data are featured by high x-values, whereas ice layers in the intensity record correspond to low x-values. The verification of the agreement of the two stratigraphy records is displayed as visual quantification (C) and percent per depth interval of one meter (D). Black bars represent areas in which both logs show the same material, whereas white bars indicate no agreement. The video was recorded from the snow surface.

III. 2013 firn core borehole (A) video intensity and firn core stratigraphy

The 2013 firn core comprises the deepest stratigraphy record (15.29 m) of the analyzed data set beneath the LSS (Figure 18). The firn-ice transition is reached at a depth of 12.30 m. No firn layers are observed below the interface. Several ice layers are found throughout the record of which four are equal to or thicker than 0.2 m.

The mean average intensity of the video log is the lowest (0.498) compared to the other intensity records, which range above 0.6 (Table 2). However, the standard deviation value of 0.118 is the highest. The standard deviation of all other intensity records is lower than 0.075. Consequently, the threshold value is approx. 0.2 lower than in the other videos. In contrast to the previously described profiles a continuous decrease in the intensity values can be observed for the entire depth range.

The comparison of the firn core and borehole video intensity stratigraphy reveals an overall moderate agreement (71 %). The best agreement of 95 % is shown in the depth interval of 3.50-4.50 m. In this depth interval, only three thin ice layers and two ice lenses are present in the firn core stratigraphy, but not replicated in the intensity profile. The section between 14.50-15.50 m shows the lowest agreement of 40 % and is situated below the firn-ice transition. The intensity output of the video does not reproduce the continuous occurrence of ice in this section of the borehole wall. The intensity fluctuates around the threshold value, which creates a disturbed stratigraphy record.

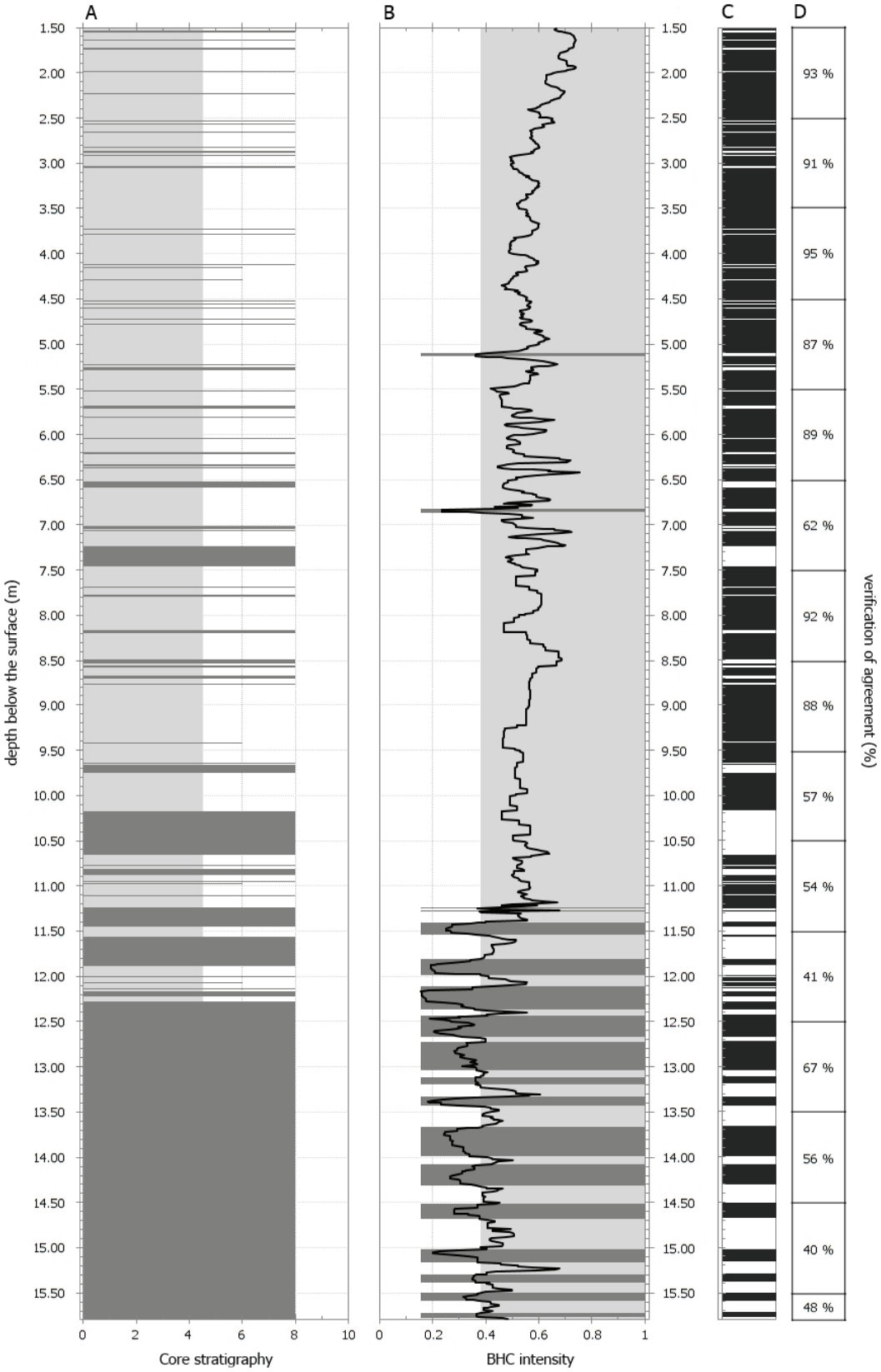

Figure 18: Comparison of the 2013 firn core borehole (A) video intensity and firn core stratigraphy. The ground truth firn core stratigraphy (A) is classified into firn (light gray) and ice (dark gray). The scale of the x-axis is artificial (0-10), but necessary to distinguish between ice lenses (x = 6) and ice layers (x = 8). The firn and ice sections (B) of the normalized and smoothed average intensity record (thin black line) are classified according to the threshold value of 0.380. Note that ice layers in the firn core data are featured by high x-values, whereas ice layers in the intensity record correspond to low x-values. The verification of the agreement of the two stratigraphy records is displayed as visual quantification (C) and percent per depth interval of one meter (D). Black bars represent areas in which both logs show the same material, whereas white bars indicate no agreement. The video was recorded from the LSS 1.50 m below the snow surface.

IV. 2013 snow pit borehole (B) video intensity and firn core stratigraphy

To investigate whether the results for the 2013 would improve by examining another video, an intensity record form a nearby ice auger borehole was processed. The 2013 snow pit borehole (B) was drilled approx. 3 m away from the borehole from which the firn core was retrieved. The diameter of the ice auger borehole was 5 cm smaller than the one of the firn core and the firn-ice transition was not reached. To compare the 2013 firn core stratigraphy record and the snow pit intensity profile, the propagation of ice layers and lenses in the firn are considered to be constant over the distance of 3 m.

One ice layer (7.25-7.45 m) in the firn core record is thicker than 0.20 m and three ice lenses are shown. The remaining thin ice layers are distributed below the LSS. The intensity profile indicates three ice layers 0.15-0.20 m underneath the snow surface that are not present in the ground truth record. Contrarily, the ice layers in the intensity record section between 7.00-7.70 m are represented in the firn core stratigraphy. The intensity profile in this depth interval is shifted with less than 0.05 m towards the surface, but shows the same sequence of ice layers as the firn core stratigraphy.

The 2013 snow pit borehole (B) intensity profile (Figure 19) indicates an overall good agreement with a minimum of 69 % at 8.00-9.00 m depth and a maximum of 96 % between 3.00 and 4.00 m. The good agreement of more than 90 % is found for the first 5 m of the record, whereas the following sections do not exceed 78 %. The highest number was calculated in the depth interval with the low number of three thin ice layers in the firn core and none in the intensity stratigraphy.

In general, no increasing or decreasing trend in the intensity signal in the firn sections of the intensity profile can be detected.

The results of the stratigraphic analysis of the borehole camera video intensity demonstrate a high variability in the amount of the reproduced ice agglomerations. The best agreement is achieved in sections without or with minimal ice content in the firn core. Thicker ice layers are more likely to be represented in intensity-derived stratigraphy record than smaller ice layers.

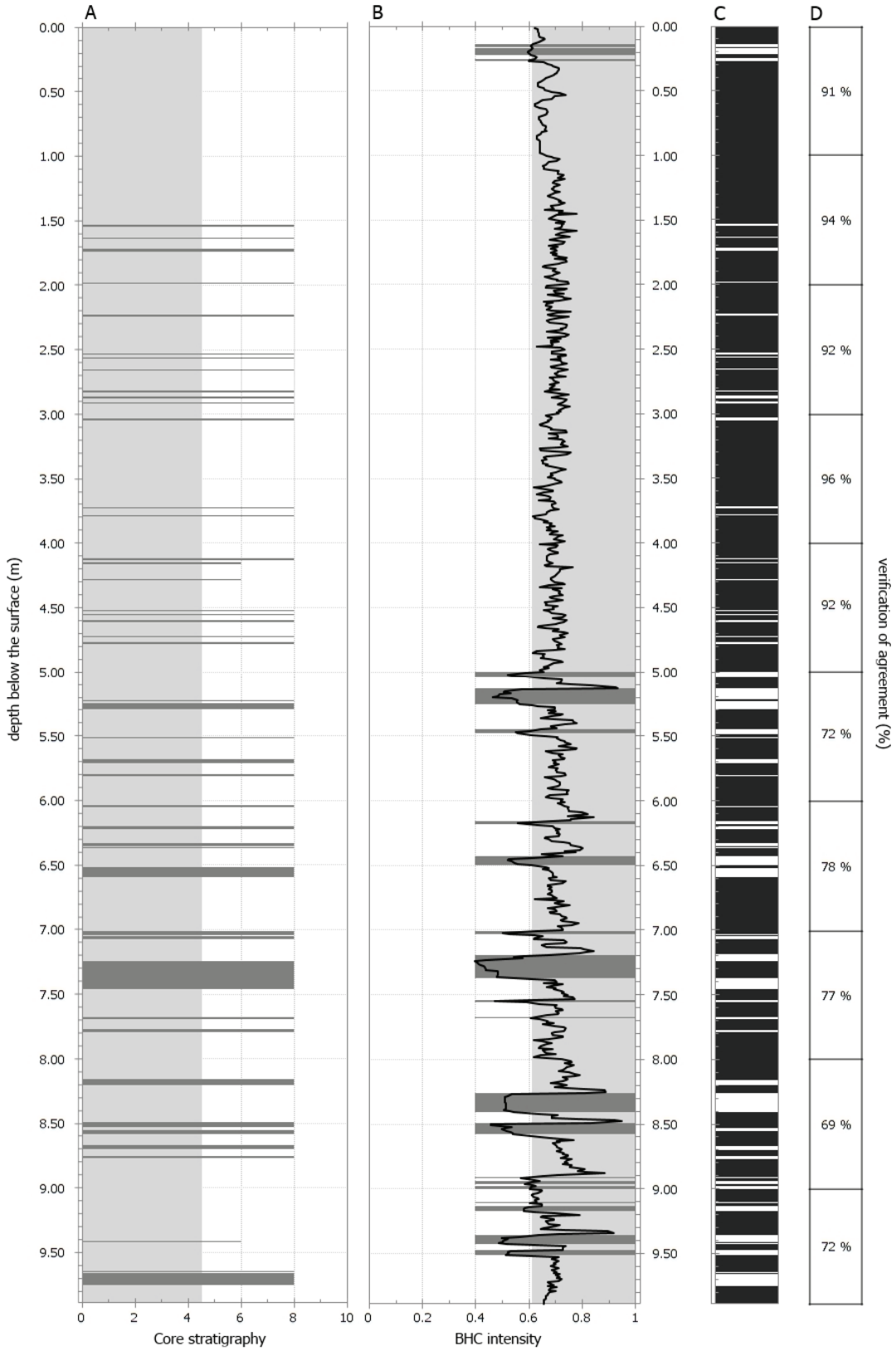

Figure 19: Comparison of the 2013 snow pit borehole (B) video intensity and firn core stratigraphy. The in ground truth firn core stratigraphy (A) is classified into firn (light gray) and ice (dark gray). The scale of the x-axis is artificial (0-10), but necessary to distinguish between ice lenses (x = 6) and ice layers (x = 8). The firn and ice sections (B) of the normalized and smoothed average intensity record (thin black line) are classified according to the threshold value of 0.611. Note that ice layers in the firn core data are featured by high x-values, whereas ice layers in the intensity record correspond to low x-values. The verification of the agreement of the two stratigraphy records is displayed as visual quantification (C) and percent per depth interval of one meter (D). Black bars represent areas in which both logs show the same material, whereas white bars indicate no agreement. The video was in an ice auger borehole approx. 3 m away from the firn core borehole. It was recorded from the snow surface.

5.3.4.2 Cumulative firn core and video intensity stratigraphy ice content

To evaluate, if the borehole camera videos replicate ice structures in the firn an estimation of the ground-truth and intensity-derived ice content was accomplished. The cumulative thickness of ice in the firn core and in the intensity record is shown in Figure 20.

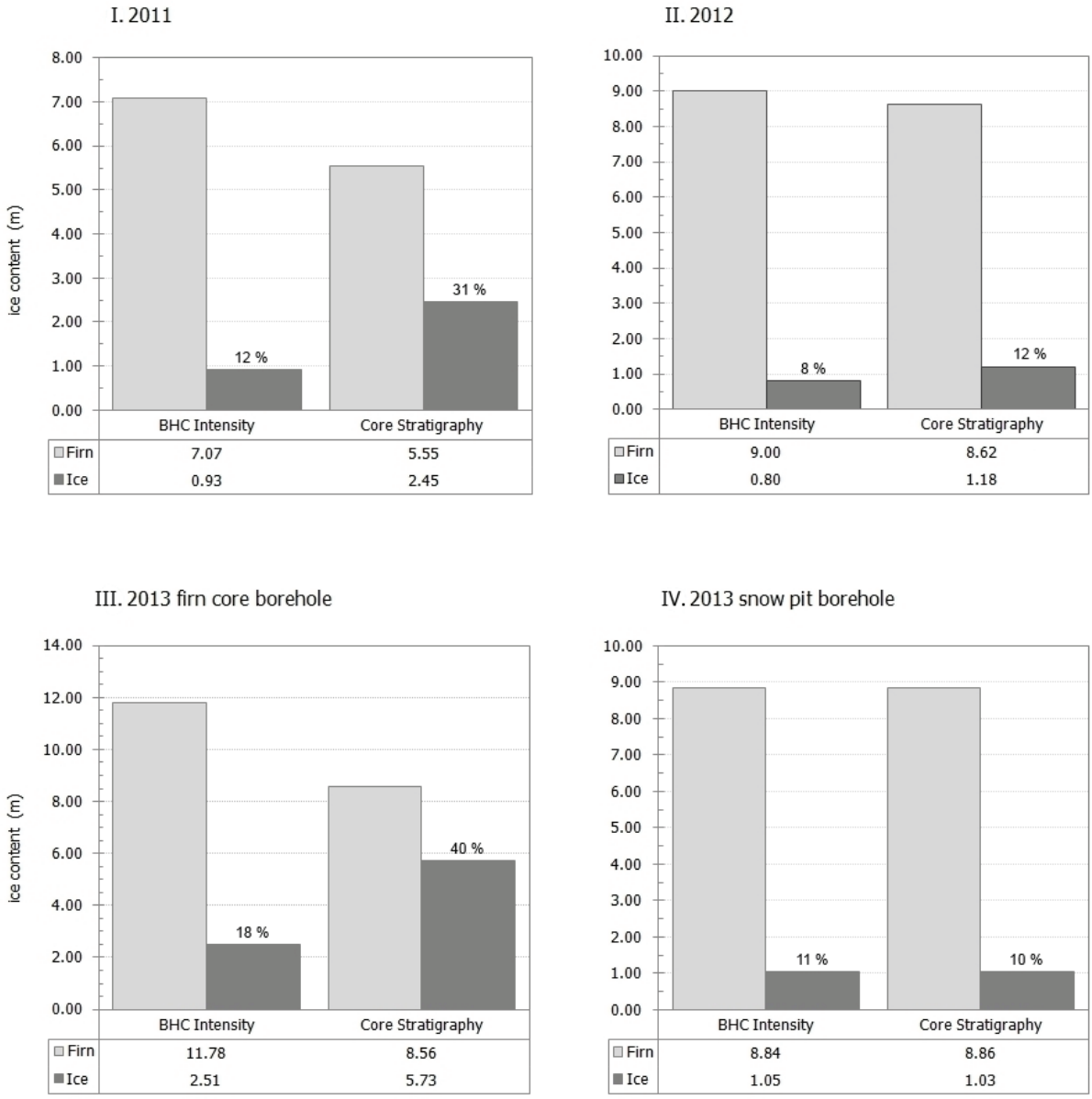

Figure 20: Cumulative ice content derived from the firn core (Core Stratigraphy) and video intensity stratigraphy (BHC intensity). The firn and ice content for each of the analyzed videos and the corresponding depth interval of the firn core is displayed in separate diagrams. The percentage value above the ice content represents the overall proportion of ice in respect to the entire length of the log.

The results reveal an average underestimation of the ice content by 15 % in the intensity profile of the videos, which were recorded in the firn core boreholes. A good approximation was achieved in the ice auger drilled borehole (III.).

The 2013 snow pit borehole (B) log (III.) reproduces the closest estimation of ice in the borehole wall. The intensity-derived stratigraphy indicates 0.02 m more ice (1%) than observed in the upper 9.8 m of the ground truth data. The 2013 snow pit borehole (B) log does not cover the full range from the surface to the firn-ice transition. Therefore the cumulative amount of ice is smaller. As presented in Figure 19, the distribution of the ice layers is not necessarily equal to the firn core stratigraphy, but the overall content is estimated accurately. The highest spatial agreement of the stratigraphy records is shown in the 2012 data. By analyzing the overall ice content, it becomes apparent that the borehole camera video ice fraction (II.) underestimates the amount of ice. It deviates from the firn core log by 4%, which is equal to 0.38 m of ice in the firn. The 2011 (I.) intensity-derived stratigraphy underestimates the ice proportion by 19 % and thus, only records a third of the ice present. The result corresponds to a deficit of 1.5 m of ice.

The greatest disagreement occurs between the 2013 firn core data and the firn core borehole (A) intensity log. 22 % of the ice in the borehole wall is not replicated by the intensity stratigraphy. The percentage value corresponds to a shortage of more than 3.2 m of ice due to the length of the borehole and the transgression below the firn-ice transition.

5.3.4.3 Sectional analysis of ice content

In the following, a sectional analysis of the firn core and video intensity-derived ice content will be described. The ice content is compared to verify, if the borehole camera can provide a proxy of the amount of ice agglomerations in predefined intervals. The percentage of agreement represents the ratio of ice, which is shown after the classification of the intensity record in respect to the ground truth firn core.

I. 2011 profile ice content (Figure 21)

In general the ice fraction is overestimated in the intensity profile where the firn core data indicates less than 0.20 m of ice and severely underestimated otherwise. More than 0.5 m of ice can be observed in the firn core record in the depth ranges of 2.74-3.73 m, 6.74-7.73 m and 8.74-9.73 m (Figure 21, Table 7 in appendix). None of these values are reflected accurately in the intensity profile. In the remaining sections of the log, the borehole video camera suggests more ice content than measured in the firn core. An exception is the first depth interval, in which no ice layers are reproduced by the intensity log. In the depth interval 5.74 – 6.73, the borehole video camera registers 200 % more ice. The high value is caused by the small amount of 0.02 m ice in the firn core and 0.04 m in the intensity profile.

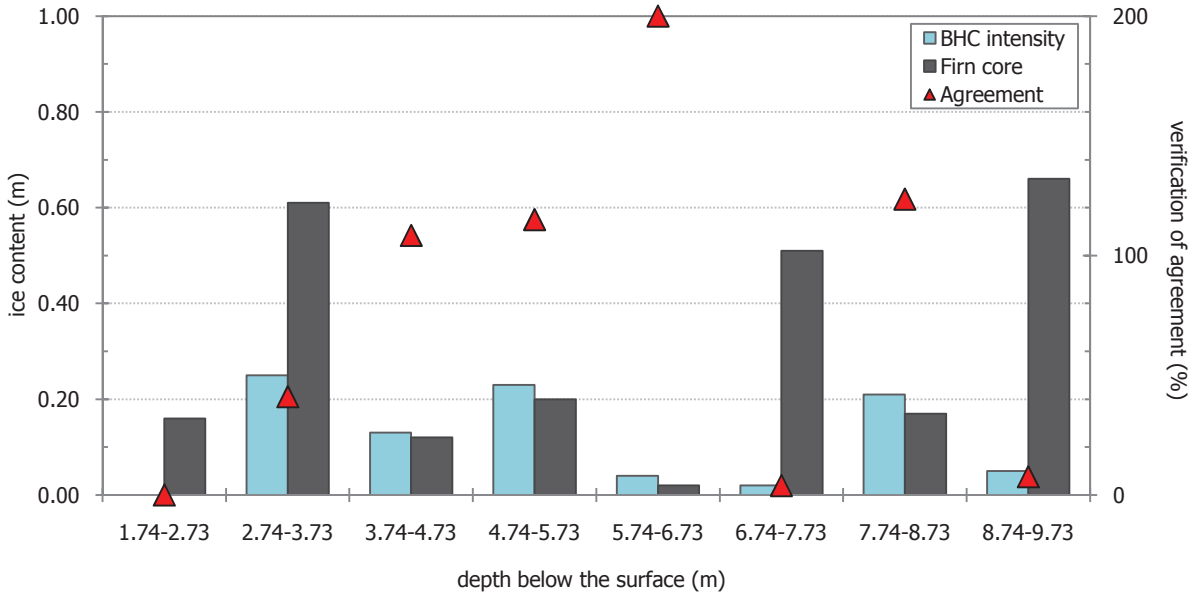

Figure 21: Ice content per depth interval of the 2011 firn core (grey) and video (BHC) intensity stratigraphy (blue). The bars represent the ice content in cm in each of the specific sections. The depth intervals have a length of one meter, starting from the top of the log. The percentage value of the agreement (red triangle) verifies if the ice content was over- or underestimated.

II. 2012 profile ice content (Figure 22)

The 2012 firn core record contains an overall low amount of ice with less than 0.20 m per depth interval (Table 8 in appendix). Exceptions are the two sections below 8.01 m with 0.42 m and 0.34 m, respectively. In the first two meters, no ice is recorded in the firn record or in intensity profile. Therefore, the records are in 100% agreement with each other. In contrast to the 2011 log, the ice content is underestimated by the video intensity in general except for one depth interval (5.01-6.00 m). The pattern is caused by the absence of ice layers in the borehole camera record in the depth intervals 4.01-5.00 m and 6.01-7.00 m

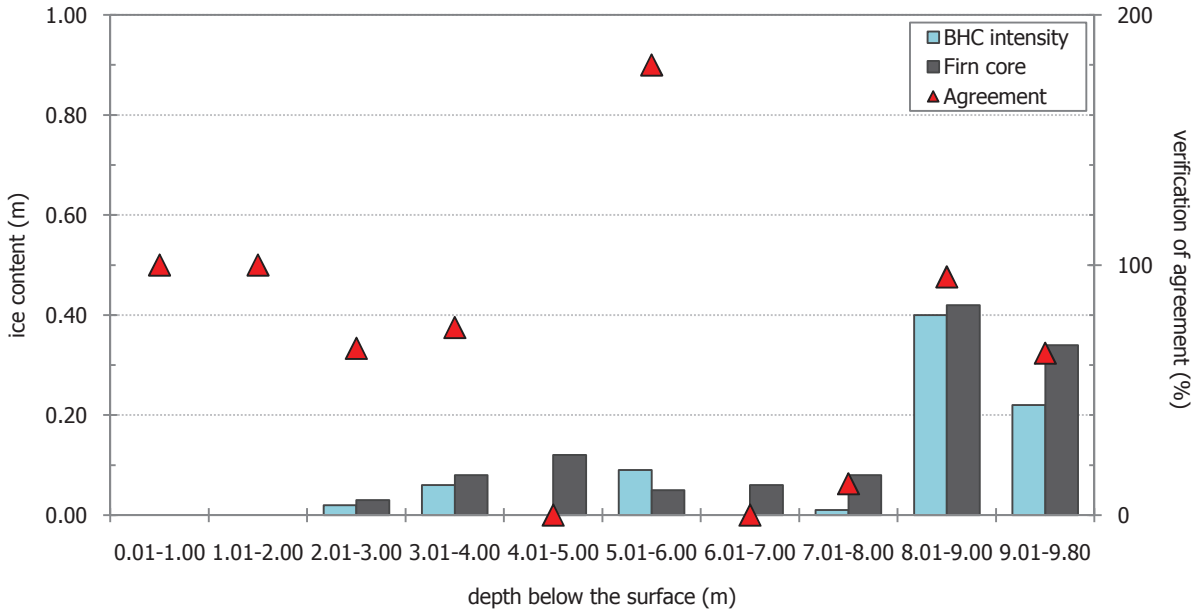

Figure 22: Ice content per depth interval of the 2012 firn core (grey) and video (BHC) intensity stratigraphy (blue). The bars represent the ice content in cm in each of the specific sections. The depth intervals have a length of one meter, starting from the top of the log. The percentage value of the agreement (red triangle) verifies if the ice content was over- or underestimated.

III. 2013 firn core borehole profile ice content (A) (Figure 23)

The 2013 firn core borehole (A) intensity-derived stratigraphy underestimates the amount of ice throughout the record (Table 9 in appendix). In the borehole wall sections of 1.51-4.50 m and 7.51-9.5 m, no ice is suggested by the intensity profile. The agreement values do not rise above 40 % in the first 11.50 m of the log, which includes roughly the entire firn section of the core. Below the depth of 12.51 m, the borehole wall section contains 100 % of ice, whereas the video intensity does not replicate the high amount. The best agreement is found in the depth interval between 11.51-12.50 m with 90 %.

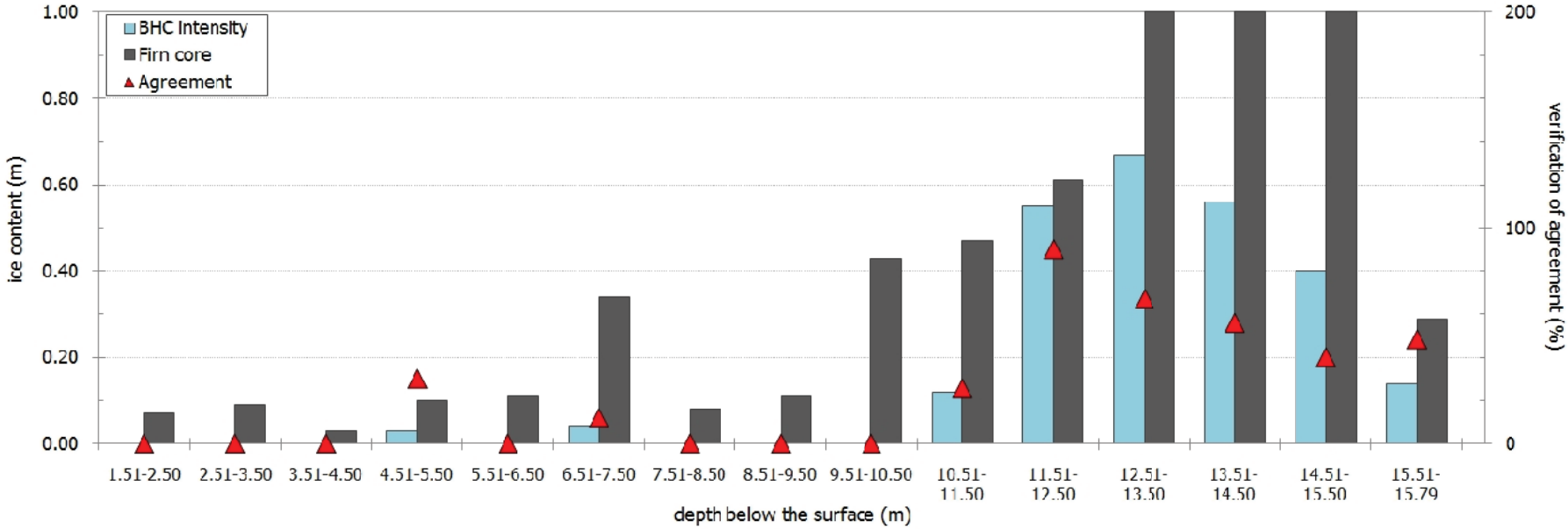

Figure 23: Ice content per depth interval of the 2013 firn core (grey) and firn core borehole (A) video (BHC) intensity stratigraphy (blue). The bars represent the ice content in cm in each of the specific sections. The depth intervals have a length of one meter, starting from the top of the log. The percentage value of the agreement (red triangle) verifies if the ice content was over- or underestimated.

IV. 2013 snow pit borehole profile ice content (B) (Figure 24)

The first meter in the 2013 snow pit (B) profile demonstrates the only case in the overall analyzed data in which the video intensity suggests ice (0.09 m) and no ice content is observed in the firn core (Table 10 in appendix). The following sections (1.01-5.00 m) present ice fractions of less than 0.10 m each, however none is reproduced by the borehole camera intensity. The overall ice content per depth interval is lower than 0.20 m with the exception of 0.23 m between 7.01-8.00 m. In the second half of the record, the ice content is overestimated by the intensity stratigraphy in three sections. Each of them comprises less than 0.20 m of ice.

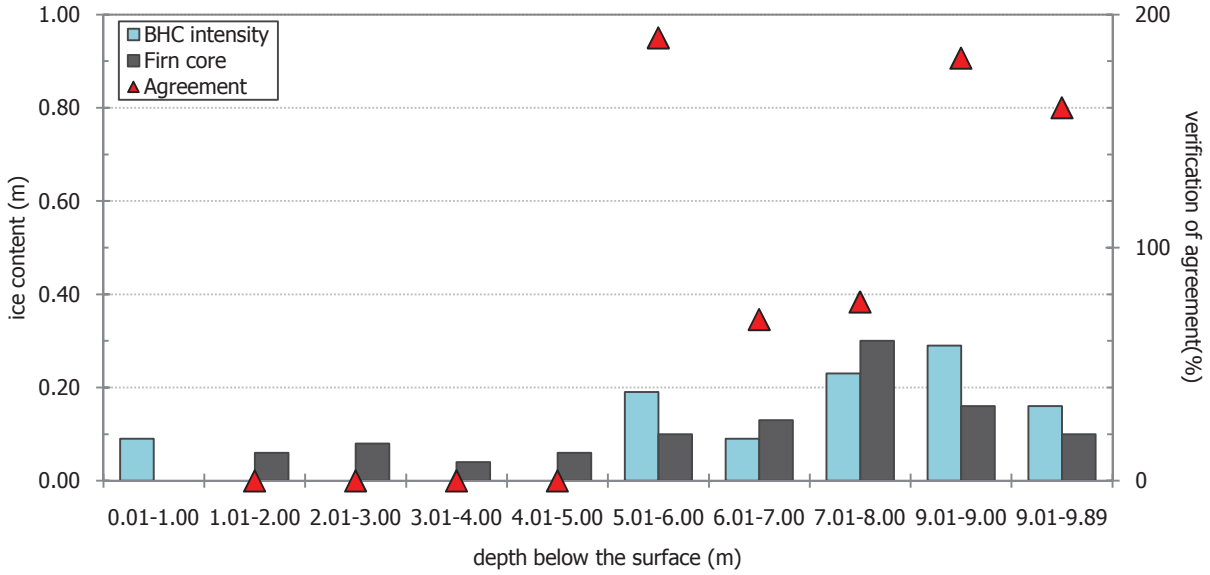

Figure 24: Ice content per depth interval of the 2013 firn core (grey) and snow pit borehole (B) video (BHC) intensity stratigraphy (blue). The bars represent the ice content in cm in each of the specific sections. The depth intervals have a length of one meter, starting from the top of the log. The percentage value of the agreement (red triangle) verifies if the ice content was over- or underestimated.

6. Discussion

In this chapter the results of the mass balance measurements and firn core stratigraphy are discussed in terms of weather conditions on the Austfonna Ice Cap and previous investigations of the surface mass balance. The advantages of the firn-ice fraction estimation on the specific surface net mass balance and the influence of meltwater refreezing are presented. Further, the product of the borehole camera video analysis tool, the threshold for the intensity-derived firn stratigraphy and persistent problems in the set-up and processing program are addressed.

6.1 Specific surface mass balance and firn stratigraphy in the summit area

Since 1998 the thickness of the snow cover on the Austfonna Ice Cap has been mapped by GPR (Dunse et al. 2009, Pinglot et al. 2001, Schuler et al. 2013, Taurisano et al. 2007). The snow thickness measurements revealed a greater accumulation in the south-east with a decreasing trend towards the north-west. The distribution pattern is likely caused by the northern mitigation of weather systems originating over the Barents Sea (Pinglot et al. 2001).

The specific surface winter mass balance has been calculated in this study for the firn core drilling locations in the summit area of the Austfonna Ice Cap. Results illustrate a varying pattern throughout the observation period 2009-2012. The measured values range from 46.8 to 62.4 cm w.eq. with an average value of 54.6 cm w.eq. Taurisano et al. (2007) describe a spatially consistent accumulation pattern on the ice cap with high interannual variabilities. Their findings are in agreement with the observations made in this study. According to the spatial distribution map of winter mass balance on the Austfonna Ice Cap (Pinglot et al. 2001), the field site at the summit had an annual winter balance of 50-60 cm w.eq. in 1998-1999. The same range is recorded in the years 2009-2012 in this investigation.

Pinglot et al. (2001) estimated the mean annual net mass balance value for the summit area of the Austfonna Ice Cap using firn core measurements and GPR for the years 1963-97, whereas Schuler et al. (2007) modeled the net mass balance distribution in 2004-2005. Both studies proposed a positive net mass balance of >50 cm w.eq in the summit area of the ice cap. The average specific net mass balance (59.9 cm w.eq., b_n standard, 63.4 cm w.eq., b_n fraction) calculated in this study from a mass balance stake and firn core stratigraphy (2009-2012), is in agreement with the previously published results. This finding indicates that the specific net mass balance has not changed considerably over the last 50 years.

The specific surface net balance values presented in this study are highly variable (e.g. 32.8-81.9 cm w.eq. b_n fraction). While the net mass balance of 2009 is well below the average and 2010 somewhat, 2011 and 2012 exceed the long term mean by approximately 20 cm w.eq.

In three of four years, the specific net mass balance was higher than the winter mass balance. Similar observations have been reported by Pinglot et al. (2001) in the late 1990s. In contrast to the negative summer balance in 2009, the positive specific summer mass balance accounts for 43% and 21% of the net balance in 2011 and 2012, respectively. Since the field observations have been carried out in May of each year, no direct measurements of the specific summer balance have been performed.

The positive summer mass balance in 2011 and 2012 suggests that snow accumulation is not restricted to the winter months (September-May), but also occurs during summer (June-August). The measured snow thickness in May does not account for subsequent accumulation.

Schuler et al. (2013) published meteorological records from a weather station located ~400 m a.s.l. on the Austfonna Ice Cap from May 2004 - May 2012. The summit area is located approximately 300 m higher than the weather station and is therefore exposed to lower air temperatures throughout the year. However, interdependencies between the meteorological conditions at lower elevation and the specific surface mass balance at the Summit can be observed.

In the summer of 2009 the highest number of PDD (positive degree day) were registered (Schuler et al. 2013). This corresponds well with the low specific surface net mass balance (32.8 cm w.eq., b_n fraction) for the same year. Compared to 2009, lower PDD in summer 2010 and a higher winter mass balance were measured, resulting in a higher net mass balance (60.2 cm w.eq., b_n fraction). 2011 appears to be an extraordinary year in the meteorological and mass balance record. While the specific winter mass balance (46.9 cm w.eq.) is lower than 2009 (49.1 cm w.eq.) and temperatures above 0°C are recorded from July until October. The net mass balance is more than twice as high as in 2009.

The standard and firn-ice fraction methods are applied to calculate the specific net mass balance. While the standard method assumes a constant density value for firn, firn-ice fraction method accounts for the amount of ice in the old snow pack. According to the derived firn core stratigraphy, ice layers and lenses occur in each section below the LSS. The results demonstrate an underestimation of the net mass balance by 5.8 %, if the ice content in the firn below is not considered in the assessment. The difference in specific net in 2010 is high enough to invert the negative summer balance estimated by the standard method. By implementing the ice-fraction method in this particular year the summer balance becomes positive and in theory no mass is lost during the ablation season.

Both methods are based on several assumptions, which are crucial for the calculation of the specific mass balance at the summit area of the Austfonna Ice Cap.

The firn core boreholes are located in the long-term firn area (Dunse et al. 2009), which is proven by the number of summer surfaces recognized in the 2013 firn core above the firn-ice transition. The mass balance stake is located 900 m away from the borehole location of the 2011 and 2012 firn core and even further from the 2010 and 2012 drilling location. Therefore topographical constraints and variations in the subsurface are neglected.

Parry et al. (2007) concluded that features in the snow pack created by meltwater percolation and refreezing are spatially inconsistent. Ice layers and widespread ice lenses observed in one snow pit within the percolation zone of the Greenland Ice Sheet, were seldom correlated to the snow stratigraphy recorded 1-10 m away. However, less permeable layers such as wind crust and sastrugi surfaces induce ice layers. Their results contradict studies by Pfeffer and Humphrey (1998), who concluded that ice layers in the snow pack are confined by specific stratigraphic boundaries related to grain size differences.

The comparison of the firn core stratigraphy for the period investigated in this study supports the results of Parry et al. (2007). The record indicates an overall incoherent stratigraphy pattern in between the years and location of the firn core boreholes.

By estimating the mass balance from height changes of the stake in the accumulation area, no additional meltwater is assumed to infiltrate the snow pack and firn from adjacent areas. The assessment of the run-off limit, the upper limit of elevation at which meltwater solely refreezes in the snow/firn pack without the reduction of net mass balance, is essential (Parry et al. 2007, Pfeffer et al. 1991). Saturated layers in the firn in the summit area of the Austfonna Ice Cap have been reported during the process of firn core drilling and the temperate firn is evident down to several meters below the surface (Schuler 2014, personal communication). Wet firn beneath a substantial amount of cold firn suggests subsurface accumulation or ponding of water. This is likely related to topographical depressions and retained water above an impermeable layer.

The firn-ice fraction method seems to provide more accurate specific surface net balance results, but inconsistent stratigraphy and spatially constrained ice layers and lenses have to be considered.

Since the field site, within the summit area of the Austfonna Ice Cap, is located in the percolation/wet snow zone, internal accumulation is a significant factor in the annual mass balance assessment. Möller et al. (2011) concluded that, on average, 25 % of the ablation is preserved in the firn on the Vestfonna Ice Cap in 2000-2009. Vestfonna is located west of Austfonna on Nordaustlandet.

In this thesis, firn cores (2010-2013) have been analyzed to reveal ice layer thickness changes below the LSS throughout the observation period. The only year with a substantial ablation rate is 2009. Unfortunately, no firn core stratigraphy record was available for 2009 to compare it to the ice content of the 2010 core. An increase in ice layers would provide evidence of internal accumulation caused by severe melting. Nevertheless, the 2011 firn core exposes the highest amount of ice (80.9 cm w.eq.) in the depth interval between the 2006-2009 summer surface interfaces.

A thick ice layer (~10 cm) is visible at 5.50 m in the 2011 core. At the same depth one year later, three thinner layers are present in the core stratigraphy. By assuming that ice agglomerations propagate rather than segregate, the question has to be raised, whether the change is caused by spatial variabilities in the firn or discrepancies in the classification procedure. The 2011 firn core was not categorized by the author. However if the increase in ice is related to topographical depressions, more meltwater could have been infiltrating the underlying firn. Remarkably the 2013 firn core, retrieved approximately three meters away from the borehole in 2011, does not reflect the thick ice agglomerations in the same depth interval.

In order to broaden the knowledge about the onset and progression of meltwater infiltration into the snow/firn pack on the Austfonna Ice Cap, supplementary surveys at the end of the ablation season should be arranged (Bell et al. 2008, Parry et al. 2007, Pfeffer and Humphrey 1996, Pfeffer and Humphrey 1998) and firn cores should be classified according to firn types as proposed by Brown et al. (2011) and Bezeau et al. (2013). Additional methods, such as the approach of Trabant and Mayo (1985) and Schneider and Jansson (2004), to quantify internal accumulation depending on the temperatures and water content of firn should be implemented.

6.2 Borehole camera video system

The glaciology team of the University of Oslo operated a borehole camera set-up in the years 2011-2013 on the Austfonna Ice Cap. The following discussion about the results, problems and potential improvements is based on the analyzing process, personal communications with colleagues and the author's participation in field work activities on the Austfonna Ice Cap in the year 2013.

6.2.1 Reliability and accuracy of the video intensity-derived stratigraphy

The comparison of the video intensity-derived firn stratigraphy with ground truth firn core data revealed a varying agreement depending on the ice content in the borehole wall and the operation of the camera.

Average agreement between the stratigraphy records ranges from high values in the 2012 (91 %) and 2013 snow pit borehole (B) (83 %) video to moderate in the 2011 and 2013 firn core borehole (A) with 63 % and 71 %, respectively. The same tendency is evident in the results of the cumulative ice content. 2011 and 2013 (A) replicate less than half of the ice, which is present in the borehole wall, whereas 2012 and 2013 (B) exhibit approximately the same amount. The best approximation was achieved in the ice auger drilled borehole (2013 B).

The results indicate a general underestimation of ice content by the borehole camera video intensity, if more than 0.20 m of ice is observed in a section (1m) of the firn core. Both 2013 (A, B) intensity records do not replicate any ice layers in wide sections in the upper part of the log. Although the 2011, 2013 B intensity record overestimates the ice content, if less than 0.20 m are measured in the firn core data, the finding is not supported by the 2012 and 2013 (A) profiles. Overall good agreement is achieved in sections without or with minimal ice content in the firn core. Thicker ice layers are more likely to be replicated in the corresponding depth range than smaller ice layers.

The field operation of the borehole camera directly influences the output of the processing tool. If the camera is hauled up fast during the logging, the vertical resolution decreases. Hubbard et al. (2008) suggested a hauling speed of ~1m per min (1.6 cm sec^{-1}). During the field work in 2011 and 2012 the borehole camera was pulled up with an average speed of 1.16 and 1.06 cm sec^{-1}. In contrast, the video camera was moved 14.01 and 8.47 cm sec^{-1} in the 2013 (A) and 2013 (B) boreholes, respectively. Nevertheless, a simple relation between the quality of the intensity-derived stratigraphy and the average speed was not identified. While the agreement between

the stratigraphy records is poor in 2011 and the hauling speed slow, the 2013 (B) data set reveals a good agreement with a speed seven times higher.

The movement profiles show an inconsistent motion of the camera along the length of the borehole due to the manual operation of the cable winch. Temporary acceleration of the camera during the logging process causes the spatial interval between the frames to increases. Hence, thin ice layers are likely not to be detected in the narrow search window. In the 2013 (A) video fewer thin ice layers are represented in the intensity stratigraphy record, which could be related to the high camera movement of 4.6 mm per frame on average compared to the other videos.

The processing algorithm calculates the specific depth value for each frame. Therefore, the movement profile is dependent on the accurate determination of the depth encoder values in the video. If the numbers are not recognized by the digit classification program, the depth values are interpolated until the next number is identified. The camera in the 2011 and 2013 (A) video was not centered throughout the log. As a result the background section behind the depth value is too illuminated to generate enough contrast. Depending on the degree of misinterpretation, the depth and intensity record is distorted. To improve the depth estimation, the movement has to be consistent and the camera centered in the borehole. Consequently, the horizontal position in the borehole and a steady vertical movement are more relevant than a low hauling speed.

The 2013 (B) video logged in an ice auger borehole three meters away from the firn core borehole, agrees better with the firn stratigraphy record than the 2013 (A) video itself. The smaller borehole diameter might prevent horizontal swinging of the camera during the recording and increases the accuracy, even though ice layers are highly variable over short distances (Parry et al. 2007). However, the higher agreement can also be related to the poor representation of solid ice below the firn-ice transition in the 2013 (A) video.

Hawley and Morris (2006), Kinnard et al. (2008) and Hubbard and Malone (2013) noticed an inversion of the intensity signal with depth. These authors correlated the density of the firn with the borehole wall intensity and concluded that a change in densification process causes the signal to reverse. While grain boundary sliding increases the intensity values, pressure sintering reduces the signal. As a result, they recorded dark sections at the bottom of the borehole and brighter sections the further the camera was hauled to the surface. The inversion point was reached at ~10-15 m below the surface. From this point onwards the intensity decreased once again.

The inversion in the intensity signal was not observed in the borehole video camera data analyzed in this study. The reason could be the location of the field site. While Hawley and Morris (2006) carried out their field work at the Summit camp and Hubbard et al. (2008) at NEEM (North Greenland Eemian Ice Drilling) on the Greenland Ice Sheet, both located in the dry snow zone, the summit of the Austfonna Ice Cap is comprised of the wet snow zone. Hence, the

densification of snow and firn proceeds more rapidly and is influenced by percolating meltwater. Higher firn densities and ice agglomerations could diminish the inversion of the intensity signal.

6.2.2 Threshold determination

The threshold (Equation 4) is the most important parameter of the firn stratigraphy classification. It categorizes firn and ice in the borehole wall according to the mean average intensity of the record. Several external factors, such as the position of the camera in the borehole, influence the quality of the log. As seen in the intensity log (e.g. Figure 12), results from the center and side record of the same borehole do not give the same values necessarily. Consequently, the statistical comparison becomes invalid. However, both records exhibit low intensity sections, which indicate ice layers. Hence, the threshold value has to adjust depending on the statistical properties of the individual intensity record.

As shown in the high agreement values derived from the firn stratigraphy and detailed ice content comparison, the threshold chosen in this study produces reliable results. Nevertheless, exceptions can be found in the intensity-derived firn stratigraphy records (e.g. at 8.90 m in 2011 and 9.40 m in 2012). The intensity peaks indicate a change in borehole wall composition, but are not significant enough to be classified as ice. The median $\tilde{x}_{rec}$ instead of the mean $\bar{x}_{rec}$ of the average intensity record or the STD σ_{rec} multiplied by the factor f ($f < 1.0$) could be applied. Both modifications would raise the threshold value and therefore, more sections of the intensity record would be classified as ice. The cumulative ice content of the 2011 and 2013 (B) intensity-derived stratigraphy records would approximates the total amount of ice in the firn cores. However, more section classified as ice in the 2012 and 2013 (B) record would decrease the quality of the stratigraphy log.

6.2.3 Persistent problems with the set-up and recommended improvements

Operating the borehole camera video system in glacial or cold climate environments causes problems. During the field work on the Austfonna Ice Cap several situations occurred in which the camera lens and mirror of the borehole camera fogged up. The fogging is caused by the rapid change from very low temperatures (approx. -15°C and below) on the surface to moderate temperatures of a few degrees Celsius below the freezing point in the borehole.

The drilling equipment roughens the borehole wall and produces firn and ice chips. The loose chips had to be cleared of the borehole wall, before the video camera was inserted. If not

removed, the chips can cover the mirror of the camera and downgrade the performance of the processing program. Furthermore, they fill up the borehole during the drilling process gradually. The cleaning tool of choice was a commercial toilet brush, which was attached to several avalanche probes. This method caused multiple problems. The videos reveal that the brush proved to be insufficient in cleaning of the borehole wall. In few situations, in which the cleaning equipment got caught in the borehole, the field work resulted in time consuming efforts to recover it.

However other cleaning methods have been discussed and reported in literature. Marchenko (2014, personal communication) suggests to lower down a brush combined with a heavy weight on a rope. Koerner et al. (1981) presented a method of pouring alcohol into the borehole to absorb the ice chips. Another option could be the operation of a hot water drill as suggested by Hubbard et al. (2008). If it is necessary to operate lightweight field equipment a mechanical, hand-stabilized drill is sufficient. To protect the surrounding surface and to confine the diameter of the upper part of the borehole, the usage of a plastic tube with a disk at the top is preferable (Hawley and Waddington 2011). While operating on the Austfonna Ice Cap, the aim of the borehole camera tool was to log an undisturbed record from the snow surface to the firn-ice transition. Loose snow at the surface tends to subside, which increases the borehole diameter and disturbs the underlying snow pack. Therefore, the borehole was drilled at the bottom of a snow pit occasionally, because the LLS provides a more stable and resistant surface.

In general, drilling equipment produces ridges, saw tooth pattern or gouges at the borehole wall, which will affect the intensity record (Hubbard et al. 2008, Hubbard and Malone 2013) . Alternations in the signal originate from variations in material composition. If lighted from above, porous firn layers cast shadows on the deeper parts of the borehole. The shadow effects are seen in the processed intensity records as small-scale fluctuations in the signal. To achieve accurate average intensity values, the camera has to be stabilized in the borehole by attached centralizers and preferably should not move laterally (Fudge and Smith 2010, Pohjola 1993).

The depth measurements have to be precise to correlate the intensity values with the stratigraphy in the firn core. This can be accomplished by an internal logger in the winch, which records the length of the camera cable or by lowering a measuring tape down into the borehole. Both methods have accuracy issues due to potential sliding of the cable or straightening issues (Hawley and Waddington 2011). The former set-up is preferable, because the measuring tape can cover up parts of the investigated borehole wall and distort the intensity record.

The movement profiles reveal the inconstant speed of the camera along the borehole caused by the manual operation of the winch. In cold climatic conditions the body has to be protected against wind and temperatures far below the freezing point. Readjusting the grip on the winch handle with thick gloves or a moment of abstraction can interrupt the hauling process. An

automatic winch set-up should be considered to reduce uncertainties and the complexity of the processing tool.

6.2.4 Failure analysis of the processing tool

All of the operational issues experienced during the field work influence the accuracy of the processing product. However, the borehole camera video analysis tool accounts for hauling speed inconsistencies and small-scale variations in the intensity signal.

The set-up utilizes a downward looking camera, which distorts the thickness of individual layers. While the mirror produces an orthogonal projection of the borehole wall, the camera lens images the wall in central projection. In the central projection, layers in the video frame are displayed thinner than they are in reality. Therefore, the search window in the processing tool does not recognize layers in their full length and the thickness is underrepresented. Nevertheless the effect of the distortion is considered to be marginal, because the distance between the camera lens and the observed section of the wall is less than 5 cm.

The mirror underneath the camera enables the processing tool to extract the layer thickness without image distortions. However the lateral view of the borehole wall is limited to the size of the mirror and the opposite site of the wall is neglected. Ice layers and lenses in the record are underrepresented, if they do not intersect the observed section. Furthermore, the fogging and coverage in ice ships as seen in the 2012 (Figure 12) and 2013 (A) (Figure 13) product causes interferences with the intensity signal. White horizontal lines or blurry changes in borehole wall material decrease the accuracy of the intensity record.

In three out of four videos, the side intensity record (off mirror) was used in the analysis of the firn stratigraphy. In the one case in which the center intensity was chosen, the mirror was not attached to the camera. In this study the intensity extracted from the mirror in the borehole camera set-up proved to be irrelevant for the analysis.

The search window in the borehole camera video analysis tool extracts grayscale values from a very confined area in the borehole. If the window size would be enlarged, the variability in the grayscale values and the impact of the shadow effects would increase. Hawley (2005) and Hubbard et al. (2008) suggest to use an annulus window around the borehole wall for down and side-looking camera systems. This method captures the intensity values of the entire wall independent of the orientation. The annulus extraction cannot be applied with the analyzed in this study, because the inserted measuring tape blocked parts of the borehole wall.

The borehole camera videos were manually reviewed before the processing. Several cases of short-time blackouts and edge artifacts were visible in the videos. Nevertheless, the search

windows are placed closer to the center of the frames and blackouts were seldom. Hence, the impact of interferences on the intensity record is considered to be minimal.

During field work, the depth encoder was reset to zero meters when the camera was close the bottom of the borehole. In the 2012 and 2013 (A, B) videos the intensity recording was started a couple of centimeters ($<$ 10 cm) above the bottom, because the mirror prohibited further lowering. The offset in depth is seen when the encoder value in the video is compared to the numbers on the measuring tape. Furthermore, the depth in the frames is displayed in meter and decimeter values. Consequently, minor inaccuracies in the start depth and the broad subdivision of the encoder values result in a depth offset of $\pm$10 cm in the intensity record.

6.3 Further applications of the borehole camera video system

The current set-up of the borehole video camera system can be operated on glaciers or large ice masses to trace spatially consistent layers over larger distances, e.g. a well-defined summer surface. Furthermore, firn conditions can be assessed, to determine internal reflection horizons mapped by GPR or air- and spaceborne radar altimeters. The intensity-derived firn stratigraphy can provide additional information about position, extent, thickness and composition of layers to support existing investigations such as Hawley et al. (2013), Langley et al. (2007) and Scott et al. (2006).

Since the borehole video camera system is used to log firn and snow stratigraphy, it could be applied as a time efficient tool to quantify the amount of refreezing and internal accumulation, if study sites are revisited on a regular basis. Firn stratigraphy profiles next to mass balance stakes increase the accuracy of mass balance measurements.

If the videos are interpreted visually, englacial channels and voids (Copland et al. 1997), bedrock sliding rates (Pohjola 1993) or ice structures can be observed and quantified (Hubbard et al. 2008, Hubbard et al. 2012).

7. Summary and Conclusion

The firn stratigraphy of glaciers, ice caps and ice sheets is a major concern for scientific studies employing mass balance measurements, GPR or airborne and spaceborne remote sensing methods. Since 2004, glaciological calibration and validation campaigns (CryoVEX) for the CryoSat-2 satellite have been carried out on the Austfonna Ice Cap, Svalbard. Part of the field work was the operation of a borehole camera system to observe the stratigraphy of firn. In the presented study, the specific surface mass balance at a location in the summit area of the ice cap was calculated, a processing tool for a borehole video camera system was developed and the products evaluated. The analyzed data set consists of shallow firn cores and a mass balance stake in addition to the borehole camera videos.

In the first part of the thesis, the specific winter, summer and net mass balance were computed for the observation period 2009-2012. The winter mass balance was derived from snow thickness measurements. For the calculation of the net mass balance two methods were applied. Based on the assumption of homogeneous layers in firn with a predefined density value, the standard method underestimates the net mass balance by 5.8 %. In contrast, the firn-ice fraction method considers the amount of ice layers in the firn. The results indicate variabilities in winter balance throughout the observation period, whereas the net mass balance increases in 2009-2011. In three out of four years the summer mass balance is positive. The comparison of the findings of this study to estimates from the last 50 years suggests that the specific net mass balance has not changed considerably in the summit area of the Austfonna Ice Cap.

The mass balance is closely related to meteorological condition on the ice cap. However, the closest weather station is located approximately 300 m below the summit. In absence of temperature inversions, temperatures above the freezing point and melting events are less severe at higher elevations. Nevertheless, thick ice agglomerations were noticed in the lower parts of the shallow firn cores, which indicate internal accumulation in years with extensive periods with air temperatures above 0°C. The highest ice content between the 2006-2009 summer surface interfaces was measured in the 2011 firn core (80.9 cm w.eq.). Thick ice agglomerations beneath the 2009 summer surface indicate internal accumulation after a long period of summer air temperatures above the melting point. In agreement with previous studies the alignment of the firn cores reveals an inconsistent pattern and composition of ice layer over short horizontal distances. These observations should be considered carefully, if individual layers are traced over greater distances with other mass balance measurement techniques.

The primary aim of this thesis was to evaluate the quality of the Junior Ultra Low Light camera for firn stratigraphy investigations. The borehole video camera set-up was operated on the Austfonna Ice Cap in 2011-2013. Four videos from firn core boreholes and an ice auger borehole

were processed and analyzed with the Borehole camera video analysis tool developed in MATLAB (2013) for this study. The processing program extracts grayscale values from the borehole videos and produces a continuous intensity log of the recorded borehole wall. Due to the manual operation of the cable winch, the accurate depth estimation is essential for interpreting the intensity record. Therefore, the program applies a self-testing depth calculation algorithm, which derives the position of the camera in the borehole from the encoder values displayed in the video frame. The tool produces a visual log of the selected borehole wall sections and an average intensity for each individual frame. To evaluate the intensity log with ground truth firn core stratigraphy, the record was classified into firn and ice section depending on a unique threshold value.

High to moderate agreement (91-63%) between the intensity-derived firn stratigraphy and the ground truth data is observed in the results. Two out of four intensity records reproduce the cumulative amount of ice layers effectively well (1-4% difference in total ice content). The firn stratigraphy log comparison reveals that thin ice layers are reproduced insufficiently. Thick ice layers are more often recognized in the corresponding depth range. If more than 0.20 m of ice per firn core section is observed, the classification of the borehole camera intensity underestimates the ice content in general. The highest agreement was shown in sections with without or with minimal ice content in the firn core. The inversion of the intensity signal with depth, reported by previous studies, was not evident in the borehole camera intensity records from the Austfonna Ice Cap.

The quality of the processing products is highly dependent on the set-up in the field and the operation of the borehole camera during the logging process. Ice chips at the wall and in the bottom of the borehole, the manual hauling of the camera without stabilizing centralizers and the downward-looking camera hinders the accurate determination of the wall intensity and distort the record. The set-up of the borehole camera system used by the glaciology section of the University of Oslo is in need of technical and operational improvements to achieve the same quality as ground truth firn core data. Recommended is a commercial system based the existing set-up and improvements that are suggested in this thesis. Nonetheless, a light-weight transportable borehole camera system with the additional processing algorithms is a reliable, logistically inexpensive and time-efficient tool. When the borehole camera system is operated on glaciers and ice masses, spatial investigations of the firn stratigraphy, ice structure and firn densification can be accomplished without the effort of drilling firn cores.

References

Allegheny Instruments, Inc. (2012). Manufacturer of GeoVISION™ Borehole Video Systems. http://www.alleghenyinstruments.com. (Access Date: 21.03.2014)

Bamber, J., Krabill, W., Raper, V. and Dowdeswell, J. (2004). Anomalous recent growth of part of a large Arctic ice cap: Austfonna, Svalbard. *Geophysical Research Letters*, **31**(12), L12402.

Bamber, J. L. and Kwok, R. (2004). Remote-sensing techniques. *In* Bamber, J. L. and Payne, A. J., *(eds.) Mass Balance of the cryosphere*, Cambridge University Press, Cambridge, 59-113.

Bell, C., Mair, D., Burgess, D., Sharp, M., Demuth, M., Cawkwell, F., Bingham, R. and Wadham, J. (2008). Spatial and temporal variability in the snowpack of a High Arctic ice cap: implications for mass-change measurements. *Annals of Glaciology*, **48**(1), 159-170.

Benn, D. I. and Evans, D. J. A. (2010). *Glaciers and glaciation.* 2nd ed., Hodder Education, London.

Benson, C. S. (1961). Stratigraphic studies in the snow and firn of the Greenland ice sheet. No. **RR70**. *COLD REGIONS RESEARCH AND ENGINEERING LAB HANNOVER NH*

Bertler, N. A. N. (2011). Ice core. *In* Shroder, J. F., Singh, V. P. and Haritashya, U. K., *(eds.) Encyclopedia of snow, ice and glaciers*, Springer, 584-589.

Bevan, S., Luckman, A., Murray, T., Sykes, H. and Kohler, J. (2007). Positive mass balance during the late 20th century on Austfonna, Svalbard, revealed using satellite radar interferometry. *Annals of Glaciology*, **46**(1), 117-122.

Bezeau, P., Sharp, M., Burgess, D. and Gascon, G. (2013). Firn profile changes in response to extreme 21st-century melting at Devon Ice Cap, Nunavut, Canada. *Journal of Glaciology*, **59**(217), 981-991.

Bohren, C. F. and Barkstrom, B. R. (1974). Theory of the optical properties of snow. *Journal of Geophysical Research*, **79**(30), 4527-4535.

Box, J. E., Bromwich, D. H., Veenhuis, B. A., Bai, L.-S., Stroeve, J. C., Rogers, J. C., Steffen, K., Haran, T. and Wang, S.-H. (2006). Greenland Ice Sheet Surface Mass Balance Variability (1988–2004) from Calibrated Polar MM5 Output. *Journal of Climate*, **19**(12), 2783–2800.

Brandt, O., Kohler, J. and Lüthje, M. (2008). Spatial mapping of multi-year superimposed ice on the glacier Kongsvegen, Svalbard. *Journal of Glaciology*, **54**(184), 73-80.

Brandt, Ola (2014). Borehole video camera. http://olabrandt.wikispaces.com/Borehole+video+camera. (Access date: 30.04.2014)

Brown, J., Harper, J., Pfeffer, W. T., Humphrey, N. and Bradford, J. (2011). High-resolution study of layering within the percolation and soaked facies of the Greenland ice sheet. *Annals of Glaciology*, **52**(59), 35-42.

Carsey, F., Behar, A., Lane, A. L., Realmuto, V. and Engelhardt, H. (2002). A borehole camera system for imaging the deep interior of ice sheets. *Journal of Glaciology*, **48**(163), 622-628.

Church, J. A., White, N. J., Aarup, T., Wilson, W. S., Woodworth, P. L., Domingues, C. M., Hunter, J. R. and Lambeck, K. (2008). Understanding global sea levels: past, present and future. *Sustainability Science*, **3**(1), 9-22.

Church, J. A., White, N. J., Konikow, L. F., Domingues, C. M., Cogley, J. G., Rignot, E., Gregory, J. M., van den Broeke, M. R., Monaghan, A. J. and Velicogna, I. (2011). Revisiting the Earth's sea-level and energy budgets from 1961 to 2008. *Geophysical Research Letters*, **38**(18).

Cogley, J. G., Hock, R., Rasmussen, L. A., Arendt, A. A., Bauder, A., Braithwaite, R. J., Jansson, P., Kaser, G., Möller, M. and Nicholson, L. (2011). *Glossary of Glacier Mass Balance and Related Terms.* IACS Contribution No. 2, UNESCO-IPH, Paris.

Copland, L., Harbor, J., Gordon, S. and Sharp, M. (1997). The use of borehole video in investigating the hydrology of a temperate glacier. *Hydrological Processes*, **11**(2), 211-224.

Cuffey, K. M. and Paterson, W. S. B. (2010). *The physics of glaciers.* 4th ed., Elsevier, Amsterdam.

DeWalle, D. R. and Rango, A. (2008). *Principles of snow hydrology.* Cambridge University Press New York.

Dowdeswell, J., Unwin, B., Nuttall, A.-M. and Wingham, D. (1999). Velocity structure, flow instability and mass flux on a large Arctic ice cap from satellite radar interferometry. *Earth and Planetary Science Letters*, **167**(3), 131-140.

Dowdeswell, J., Benham, T., Strozzi, T. and Hagen, J. (2008). Iceberg calving flux and mass balance of the Austfonna ice cap on Nordaustlandet, Svalbard. *Journal of Geophysical Research*, **113**(F03022).

Dowdeswell, J. A., Drewry, D. J., Cooper, A. P. R., Gorman, M. R., Liestøl, O. and Orheim, O. (1986). Digital mapping of the Nordaustlandet ice caps from airborne geophysical investigations. *Annals of Glaciology*, **8**, 51-58.

Dunse, T., Schuler, T. V., Hagen, J. O., Eiken, T., Brandt, O. and Hogda, K. A. (2009). Recent fluctuations in the extent of the firn area of Austfonna, Svalbard, inferred from GPR. *Annals of Glaciology*, **50**(50), 155-162.

Dunse, T., Greve, R., Schuler, T. V. and Hagen, J. O. (2011). Permanent fast flow versus cyclic surge behaviour: numerical simulations of the Austfonna ice cap, Svalbard. *Journal of Glaciology*, **57**(202), 247-259.

Dunse, T., Schuler, T. V., Hagen, J. O. and Reijmer, C. H. (2012). Seasonal speed-up of two outlet glaciers of Austfonna, Svalbard, inferred from continuous GPS measurements. *The Cryosphere*, **6**(2), 453-466.

Dunse, T., Schellenberger, T., Kääb, A., Hagen, J. O., Schuler, T. V. and Reijmer, C. H. (2014). Destabilisation of an Arctic ice cap triggered by a hydro-thermodynamic feedback to summer-melt. *The Cryosphere Discuss.*, **8**(3), 2685-2719.

Eiken, T., Hagen, J. O. and Melvold, K. (1997). Kinematic GPS survey of geometry changes on Svalbard glaciers. *Annals of Glaciology*, **24**, 157-163.

Engelhardt, H. F., Harrison, W. D. and Kamb, B. (1978). Basal sliding and conditions at the glacier bed as revealed by bore-hole photography. *Journal of Glaciology*, **20**(84), 469-508.

Fudge, T. J. and Smith, B. E. (2010). Instruments and Methods, Light propagation in firn: application to borehole video. *Journal of Glaciology*, **56**(198), 614-624.

Graham, A. G. C. (2011). Ice Sheet. *In* Shroder, J. F., Singh, V. P. and Haritashya, U. K., *(eds.) Encyclopedia of snow, ice and glaciers*, Springer, 592-607.

Hagen, J. O., Melvold, K., Eiken, T., Isaksson, E. and Lefauconnier, B. (1999). Mass balance methods on Kongsvegen, Svalbard. *Geografiska Annaler: Series A, Physical Geography*, **81**(4), 593-601.

Hagen, J. O., Melvold, K., Pinglot, F. and Dowdeswell, J. A. (2003). On the Net Mass Balance of the Glaciers and Ice Caps in Svalbard, Norwegian Arctic. *Arctic, Antarctic, and Alpine Research*, **35**(2), 264-270.

Hagen, J. O. and Reeh, N. (2004). In situ measurements technigues: land ice. *In* Bamber, J. L. and Payne, A. J., *(eds.) Mass Balance of the cryosphere*, Cambridge University Press, Cambridge, 11-43.

Hagen, J. O., Eiken, T., Kohler, J. and Melvold, K. (2005). Geometry changes on Svalbard glaciers: mass-balance or dynamic response? *Annals of Glaciology*, **42**(1), 255-261.

Harper, J. T. and Humphrey, N. F. (1995). Borehole video analysis of a temperate glacier' englacial and subglacial structure: Implications for glacier flow models. *Geology*, **23**(10), 901-904.

Harrison, W. D. and Kamb, B. (1973). Glacier bore-hole photography. *Journal of Glaciology*, **12**(64), 129-137.

Hawley, R. L., Waddington, E. D., Alley, R. B. and Taylor, K. C. (2003). Annual layers in polar firn detected by Borehole Optical Stratigraphy. *Geophysical Research Letters*, **30**(15), 1788.

Hawley, R. L. (2005). Borehole investigations of firn processes. (PhD disseration, University of Washington.)

Hawley, R. L. and Morris, E. M. (2006). Borehole optical stratigraphy and neutron-scattering density measurements at Summit, Greenland. *Journal of Glaciology*, **52**(179), 491-496.

Hawley, R. L., Brandt, O., Morris, E. M., Kohler, J., Shepherd, A. P. and Wingham, D. J. (2008a). Instruments and Methods - Techniques for measuring high-resolution firn density profiles: case study from Kongsvegen, Svalbard. *Journal of Glaciology*, **54**(186), 463-468.

Hawley, R. L., Morris, E. M. and McConnell, J. R. (2008b). Rapid techniques for determining annual accumulation applied at Summit, Greenland. *Journal of Glaciology*, **54**(188), 839-845.

Hawley, R. L. and Waddington, E. D. (2011). Instruments and Methods In situ measurements of firn compaction profiles using borehole optical stratigraphy. *Journal of Glaciology*, **57**(202), 289-294.

Hawley, R. L., Brandt, O., Dunse, T., Hagen, J. O., Helm, V., Kohler, J., Langley, K., Malnes, E. and Gda, K.-A. H. (2013). Using airborne Ku-band altimeter waveforms to investigate winter accumulation and glacier facies on Austfonna, Svalbard. *Journal of Glaciology*, **59**(217), 893-899.

Hubbard, B., Roberson, S., Samyn, D. and Merton-Lyn, D. (2008). Digital optical televiewing of ice boreholes. *Journal of Glaciology*, **54**(188), 823-830.

Hubbard, B., Tison, J.-L., Pattyn, F., Dierckx, M., Boereboom, T. and Samyn, D. (2012). Optical-televiewer-based identification and characterization of material facies associated with an Antarctic ice-shelf rift. *Annals of Glaciology*, **53**(60), 137-146.

Hubbard, B. and Malone, T. (2013). Optical-televiewer-based logging of the uppermost 630 m of the NEEM deep ice borehole, Greenland. *Annals of Glaciology*, **54**(64), 83-89.

Jóhannesson, T., Sigurdsson, O., Laumann, T. and Kennett, M. (1995). Degree-day glacier massbalance modelling with application to glaciers in Iceland, Norway, and Greenland. *Journal of Glaciology*, **41**(138), 345–358.

Kinnard, C., Koerner, R. M., Zdanowicz, C. M., Fisher, D. A., Zheng, J., Sharp, M. J., Nicholson, L. and Lauriol, B. (2008). Stratigraphic analysis of an ice core from the Prince of Wales Icefield, Ellesmere Island, Arctic Canada, using digital image analysis: High-resolution density, past summer warmth reconstruction, and melt effect on ice core solid conductivity. *Journal of Geophysical Research*, **113**(D24120).

Koerner, R. M., Fisher, D. A. and Parnandi, M. (1981). Bore-hole Video and Photographic Cameras. *Annals of Glaciology*, **2**(1), 34-38.

Kovacs Enterprise, LLC (2014). Ice drilling and coring equipment. http://kovacsicedrillingequipment.com. (Access Date: 29.04.2014)

Langley, K., Hamran, S.-E., Hogda, K. A., Storvold, R., Brandt, O., Hagen, J. O. and Kohler, J. (2007). Use of C-band ground penetrating radar to determine backscatter sources within glaciers. *IEEE Transactions on Geosciences and Remote Sensing*, **45**(5), 1236-1246.

Langley, K., Patel, A., Hawley, R., Dunse, T., Hagen, J., Kohler, J., Skourup, H., Gogineni, S., Forsström, S., Eiken, T., C., L. and Helm, V. (2012). CryoSat cal/val activities on Austfonna – Part II: Ground-based measurements using a Ku-band radar, for validation of the CryoSat-2 SIRAL data. *Earth Observation and Cryosphere Science Conference,* 13.11.-16.11.2012

Lefauconnier, B. and Hagen, J. O. (1991). Surging and calving glaciers in eastern Svalbard. *Norwegian Polar Institute*, Oslo.

Lovell, M. A., Williamson, G. and Harvey, P. K. (eds.) (1999). Borehole imaging: Applications and Case Histories*,* London. *Geological Society Special Publications*

Malone, T., Hubbard, B., Merton-Lyn, D., Worthington, P. and Zwiggelaar, R. (2013). Borehole and Ice Feature Annotation Tool (BIFAT): A program for the automatic and manual annotation of glacier borehole images. *Computers & Geosciences*, **51**, 381-389.

Marchenko, S. (2012). Internal accumulation on glaciers: qualitative description and quantitative estimates. Uppsala University Uppsala.

Marchenko, S. (2013). Review of internal accumulation rates on glaciers of Svalbard. Uppsala University.Uppsala.

Marchenko, S. (2014). Department of Earth Sciences, Uppsala University. In discussion with the author

Marks Products, Inc. (2014). Overview Borehole and Water Well Inspection Camera Systems. http://www.marksproducts.com. (Access Date: 21.03.2014)

Massom, R. and Lubin, D. (2006). *Polar remote sensing Volume II: Ice Sheets.* Springer, Chichester, United Kingdom.

MATLAB (2013). Version 8.1.0.604 (R2013a), The MathWorks Inc., Natick, Massachusetts, USA.

Moholdt, G., Hagen, J. O., Eiken, T. and Schuler, T. V. (2010). Geometric changes and mass balance of the Austfonna ice cap, Svalbard. *The Cryosphere*, **4**(1), 21-34.

Moholdt, G. and Kääb, A. (2012). A new DEM of the Austfonna ice cap by combining differential SAR interferometry with ICESat laser altimetry. *Polar Research*, **31**(1).

Möller, M., Finkelnburg, R., Braun, M., Hock, R., Jonsell, U., Pohjola, V. A., Scherer, D. and Schneider, C. (2011). Climatic mass balance of the ice cap Vestfonna, Svalbard: A spatially distributed assessment using ERA-Interim and MODIS data. *Journal of Geophysical Research: Earth Surface*, **116**(F3), F03009.

Müller, F. (1962). Zonation in the accumulation area of the glaciers of Axel Heiberg Island, NWT, Canada. *Journal of Glaciology*, **4**(33), 302-311.

Nuth, C., Kohler, J., König, M., von Deschwanden, A., Hagen, J. O., Kääb, A., Moholdt, G. and Pettersson, R. (2013). Decadal changes from a multi-temporal glacier inventory of Svalbard. *The Cryosphere*, **7**(5), 1603-1621.

United Nations Atlas of the Oceans (2014). Human Settlements on the Coast. http://www.oceansatlas.org/servlet/CDSServlet?status=ND0xODc3JjY9ZW4mMzM9KiYzNz1rb3M~. (Access Date: 29.05.2014)

Parry, V., Nienow, P., Mair, D., Scott, J., Hubbard, B., Steffen, K. and Wingham, D. (2007). Investigations of meltwater refreezing and density variations in the snowpack and firn within the percolation zone of the Greenland ice sheet. *Annals of Glaciology*, **46**(1), 61-68.

Pfeffer, W. and Humphrey, N. (1996). Determination of timing and location of water movement and ice-layer formation by temperature measurements in sub-freezing snow. *Journal of Glaciology*, **42**(141), 292-304.

Pfeffer, W. and Humphrey, N. (1998). Formation of ice layers by infiltration and refreezing of meltwater. *Annals of Glaciology*, **26**, 83-91.

Pfeffer, W. T., Meier, M. F. and Illangasekare, T. H. (1991). Retention of Greenland runoff by refreezing: implications for projected future sea level change. *Journal of Geophysical Research: Oceans (1978–2012)*, **96**(C12), 22117-22124.

Pinglot, J. F., Hagen, J. O., Melvold, K., Eiken, T. and Vincent, C. (2001). A mean net accumulation pattern derived from radioactive layers and radar soundings on Austfonna, Nordaustlandet, Svalbard. *Journal of Glaciology*, **47**(159), 555-566.

Pohjola, V. A. (1993). TV-video observations of bed and basal sliding on Storglaciären, Sweden. *Journal of Glaciology*, **39**(131), 111-118.

Pohjola, V. A. (1994). TV-video observations of englacial voids in Storglaciären, Sweden. *Journal of Glaciology*, **40**(135), 231-240.

Reeh, N. and Gundestrup, N. S. (1985). Mass balance of the Greenland ice sheet at Dye 3. *Journal of Glaciology*, **31**(108), 198-200.

Reeh, N. (1999). Mass balance of the Greenland ice sheet: can modern observation methods reduce the uncertainty. *Geografiska Annaler*, **81 A**(4), 735-742.

Roberson, S. and Hubbard, B. (2010). Application of borehole optical televiewing to investigating the 3-D structure of glaciers: implications for the formation of longitudinal debris ridges, midre Lovénbreen, Svalbard. *Journal of Glaciology*, **56**(195), 143-156.

Schneider, T. and Jansson, P. (2004). Internal accumulation in firn and its significance for the mass balance of Storglaciären, Sweden. *Journal of Glaciology*, **50**(168), 25-34.

Schuler, T. V., Loe, E., Taurisano, A., Eiken, T., Hagen, J. O. and Kohler, J. (2007). Calibrating a surface mass-balance model for Austfonna ice cap, Svalbard. *Annals of Glaciology*, **46**(1), 241-248.

Schuler, T. V., Dunse, T., Østby, T. I. and Hagen, J. O. (2013). Meteorological conditions on an Arctic ice cap—8 years of automatic weather station data from Austfonna, Svalbard. *International Journal of Climatology*.

Schuler, T. V. (2014). Department of Geosciences, University of Oslo. In discussion with the author

Scott, J. B. T., Nienow, P., Mair, D., Parry, V., Morris, E. and Wingham, D. J. (2006). Importance of seasonal and annual layers in controlling backscatter to radar altimeters across the percolation zone of an ice sheet. *Geophysical Research Letters*, **33**(24), L24502.

Sjögren, B., Brandt, O., Nuth, C., Isaksson, E., Pohjola, V., Kohler, J. and Van De Wal, R. (2007). Determination of firn density in ice cores using image analysis. *Journal of Glaciology*, **53**(182), 413-419.

Svensson, A., Nielsen, S. W., Kipfstuhl, S., Johnsen, S. J., Steffensen, J. P., Bigler, M., Ruth, U. and Röthlisberger, R. (2005). Visual stratigraphy of the North Greenland Ice Core Project (NorthGRIP) ice core during the last glacial period. *Journal of Geophysical Research*, **110**(D02108).

Taurisano, A., Schuler, T. V., Hagen, J. O., Eiken, T., Loe, E., Melvold, K. and Kohler, J. (2007). The distribution of snow accumulation across the Austfonna ice cap, Svalbard: direct measurements and modelling. *Polar Research*, **26**(1).

Trabant, D. and Mayo, L. (1985). Estimation and effects of internal accumulation on five glaciers in Alaska. *Ann. Glaciol*, **6**, 113-117.

Warren, S. G. (1982). Optical properties of snow. *Reviews of Geophysics*, **20**(1), 67-89.

WGMS, Zemp, M., Frey, H., Gärtner-Roer, I., Nussbaumer, S. U., Hoelzle, M., Paul, F. and Haeberli, W. (eds.) (2012). *Fluctuations of Glaciers 2005–2010,* Zurich, Switzerland: ICSU(WDS)/IUGG(IACS)/UNEP/UNESCO/WMO, World Glacier Monitoring Service.

Appendix

A. MATLAB Scripts

The description and the MATLAB scripts for the processing and the analysis are available at:

1. UiO Department of Geosciences – Server

   K:\gggruppe-prosj\glasio-data\svalbard\austfonna\Borehole_camera\Borehole camera video analysis tool

2. Dropbox

   https://www.dropbox.com/sh/2dfea7tuqxwwuem/AAD2v5Jb717LgyvQxPojyg7ra

The following m-files are included:

- train_detect_HOG.m
- bhc_matlabtool.m
- get_inputs.m
- compute_depth_HOG.m
- guess_digit.m
- guess_depth_from_digit.m
- video_intensity.m
- output_intensity.m
- csvwrite_with_headers.m
- smooth_intensity.m
- class_intenisty.m
- smooth_strat.m
- class_strat.m
- comparison_int_strat.m

B. Tables

Table 3: Borehole camera video properties and input data

	Coordinates (Latitude/ Longitude)	Depth range (m)	Overall length (m)	Reference Surface	Borehole diameter (m)	Search window coordinates for intensity (x, y)	Total number of video frames	Start frame for analysis	End frame for analysis	Sum of frames for analysis	Interpreted intensity (center/ side)	Duration of analyzed video section (sec)	Average speed (cm/sec)	Movement per frame (mm)
2011	79.829661 23.9602310	1.73 – 10.33	8.5	LSS	0.08	Center: (439, 397) Side: (161,212)	26310	3570	25790	22220	Center	741	1.16	0.39
2012	79.829295 23.9514944	0.00 – 9.8	9.8	Snow surface	0.08	Center: (368, 338) Side: (620, 276)	28350	610	28223	27613	Side	922	1.06	0.36
2013 firn core borehole (A)	79.829663 23.9602239	1.50 – 15.80	14.3	LSS	0.08	Center: (380, 320) Side: (99, 202)	3330	161	3207	3046	Side	102	14.01	4.69
2013 snow pit borehole (B)	79.829662 23.9601226	0.00 – 9.80	9.8	Snow surface	0.05	Center: (375, 324) Side: (633, 258)	3840	307	3800	3493	Side	116	8.47	2.81

Table 4: Firn core locations and properties

	Coordinates (Latitude/ Longitude)	Altitude (m a.s.l.)	Depth range (m)	Overall length (m)	Reference surface	Firn- ice transition depth (m)	Comments
2010	79.83267 24.00354	749	0.00 - 9.98	9.98	Snow surface	Not reached	
2011	79.829661 23.9602310	757	1.73 – 9.735	8.01	LSS	Not reached	Core length measured in the field: 8.86 m Core length measured in the cold lab: 8.005 m
2012	79.829295 23.9514944	-	0.00 – 10.26	10.26	Snow surface	9.91	Firn-Ice transition reached presumably
2013	79.829663 23.9602239	-	1.50 – 16.275	14.78	LSS	12.29	

Table 5: Mean value and mean of the STD of the smoothed and normalized average intensity center and side record

	$\bar{x}_{rec}$		$\bar{x}$ of σ_{int}	
	Center	**Side**	**Center**	**Side**
2011	0.636	0.641	0.151	0.200
2012	0.678	0.671	0.275	0.078
2013 firn core borehole (A)	0.597	0.498	0.306	0.101
2013 snow pit borehole (B)	0.752	0.680	0.230	0.209

Table 6: Ice fraction (cm w.eq.) for 2010-2013 firn cores in core section intervals between the summer surfaces of particular years

Previous summer surface - LSS	2013 core ice content (cm w.eq.)	2012 core ice content (cm w.eq.)	2011 core ice content (cm w.eq.)	2010 core ice content (cm w.eq.)
2011-2012	10.4	-	-	-
2010-2011	6.1	2.6	-	-
2009-2010	8.7	7.8	13.9	-
2008-2009	4.4	5.2	37.4	5.2
2007-2008	35.7	12.2	31.3	15.7
2006-2007	12.2	4.4	12.2	17.4

Table 7: 2011 firn core and borehole intensity (BHC) ice content

Depth below the surface (m)	Firn core ice content (cm)	BHC intensity ice content (cm)	Agreement (%)
1.74-2.73	16	0	0
2.74-3.73	61	25	41
3.74-4.73	12	13	108
4.74-5.73	20	23	115
5.74-6.73	2	4	200
6.74-7.73	51	2	4
7.74-8.73	17	21	124
8.74-9.73	66	5	8

Table 8: 2012 firn core and borehole intensity (BHC) ice content

Depth below the surface (m)	Firn core (cm)	BHC intensity (cm)	Agreement (%)
0.01-1.00	0	0	100
1.01-2.00	0	0	100
2.01-3.00	3	2	67
3.01-4.00	8	6	75
4.01-5.00	12	0	0
5.01-6.00	5	9	180
6.01-7.00	6	0	0
7.01-8.00	8	1	13
8.01-9.00	42	40	95
9.01-9.80	34	22	65

Table 9: 2013 firn core and firn core borehole intensity (A) (BHC) ice content

Depth below the surface (m)	Firn core (cm)	BHC intensity (cm)	Agreement (%)
1.51-2.50	7	0	0
2.51-3.50	9	0	0
3.51-4.50	3	0	0
4.51-5.59	10	3	30
5.51-6.50	11	0	0
6.51-7.50	34	4	12
7.51-8.50	8	0	0
8.51-9.50	11	0	0
9.51-10.50	43	0	0
10.51-11.50	47	12	26
11.51-12.50	61	55	90
12.51-13.50	100	67	67
13.51-14.50	100	56	56
14.51-15.50	100	40	40
15.51-15.79	29	14	48

Table 10: 2013 firn core and snow pit borehole intensity (B) (BHC) ice content

Depth below the surface (m)	Firn core (cm)	BHC intensity (cm)	Agreement (%)
0.01-1.00	0	9	NaN
1.01-2.00	6	0	0
2.01-3.00	8	0	0
3.01-4.00	4	0	0
4.01-5.00	6	0	0
5.01-6.00	10	19	190
6.01-7.00	13	9	69
7.01-8.00	30	23	77
9.01-9.00	16	29	181
9.01-9.89	10	16	160